

The Pennsylvania State University  
The Graduate School  
Department Mechanical and Nuclear Engineering

**MOLECULAR DYNAMICS ANALYSIS OF OXIDATION, SEGREGATION AND STRESS  
CORROSION FAILURES OF REFRACTORY ALLOYS**

A Dissertation in  
Mechanical Engineering

by  
Osvalds Verners

Submitted in Partial Fulfillment  
of the Requirements  
for the Degree of

Doctor of Philosophy

August 2014

The dissertation of Osvalds Verners was reviewed and approved\* by the following:

Adri C.T. van Duin  
Associate Professor of Mechanical Engineering  
Dissertation Advisor  
Chair of Committee

Sulin Zhang  
Associate Professor of Engineering Science and Mechanics and Bioengineering

Amanul Haque  
Professor of Mechanical Engineering

Zoubeida Ounaies  
Dorothy Quiggle Career Developmental Professorship

Karen Thole  
Department Head of Mechanical and Nuclear Engineering

\*Signatures are on file in the Graduate School

## ABSTRACT

The focuses of the thesis are heating induced segregation/mixing of refractory alloys, along with oxidation and stress corrosion properties of selected fcc metals and thin oxide layers formed on the surfaces thereof.

The particular studies include segregation and oxidation simulation of  $\text{Mo}_3\text{Ni}$  alloy clusters. These reveal favorable stabilizing oxidation resistance properties due to the Ni component, which diffuses during annealing to the surface of the clusters.

A comparative study has been done for different sized Al grains in Fe or Ni bulk matrices. Its results indicate that Ni matrix is favorable due to the grain dissolution and energetic stability properties upon heating and cooling of the structures. Oxidation simulation of the same structures in slab structures indicate that unmixed metals oxidize first and the alloy layer, which forms only for the Ni matrix, eventually segregates to single-metal layers, which oxidize subsequently.

The stress corrosion properties of Al oxide slab/thin film structures in water, noble gas and vacuum environments have been studied with the aim of subsequent stress corrosion simulation of alloys or metals with protective surface oxide layers. The obtained results indicate brittle type failures, which involve shear deformation and localized amorphization. The plasticity enhancing fluid environment effects are found to be similar for both reactive and nonreactive species, which indicates significant pressure effects and passivated reactivity of surfaces. Parallel to the corrosion study, strain rate effects and cyclic loading behavior for slab structures in vacuum have been characterized and compared at different temperatures. These indicate time dependent deformation mechanisms including temperature enhanced local amorphization prior to crack formation. Complementary analyses include extended timescale crack behavior of a slab structure in vacuum using parallel replica dynamics and steady state analysis of a slab structure in water using a Grand Canonical Monte Carlo method. The latter allow for validation of the high strain rate and limited timescale results obtained with classical molecular dynamics.

Hydrogen embrittlement studies have been conducted for Al metal slabs with oxidized surfaces. These have provided evidence for possible grain boundary decohesion and void formation related embrittlement mechanisms at different loading conditions with different initial defects.

Studies of stress corrosion properties of Ni metal slab structures in water at different temperatures have been performed. The results indicate reduction of dislocation nucleation barriers due to the water reactions on material surfaces and increased temperature, resulting in reduction of material ductility. Significant effects of stress triaxiality are also observed.

## TABLE OF CONTENTS

LIST OF FIGURES.....	ix
LIST OF TABLES .....	xvi
ACKNOWLEDGEMENTS .....	xvii
1 Introduction.....	1
1.1 Materials for coal combustion applications .....	1
1.2 Methods .....	2
2 Simulation and analysis methods.....	3
2.1 Reactive force field ReaxFF.....	3
2.2 Simulation methods.....	4
2.2.1 ReaxFF ADF settings .....	5
2.2.2 ReaxFF LAMMPS settings .....	5
2.3 Stress analysis .....	6
2.4 Strain distribution calculation .....	8
2.5 Slip vector analysis .....	8
2.6 Centrosymmetry parameter and coordination number calculation.....	9
2.7 Fracture toughness calculation .....	9
2.8 Postprocessing per-atom data.....	10
2.9 Used terminology .....	10
2.10 Crystallographic notation .....	11
3 Annealing and oxidation of binary Mo <sub>3</sub> Ni clusters.....	12
3.1 Introduction.....	12
3.2 Method .....	13
3.2.1 Initial minimization .....	13

3.2.2	Annealing .....	13
3.2.3	Oxidation.....	13
3.2.4	Radial distribution definitions .....	14
3.3	Results and discussion .....	14
3.3.1	Annealing .....	14
3.3.2	Oxidation.....	17
3.4	Summary .....	19
4	Al grain mixing in Fe/Ni matrices and its influence on oxidation .....	21
4.1	Introduction.....	21
4.2	Method .....	22
4.3	Results and discussion .....	24
4.3.1	Potential energy, volume and atom distribution during melting .....	24
4.3.2	Strain energy distribution during melting.....	26
4.3.3	Stress distribution during melting .....	27
4.3.4	Solidification analysis .....	28
4.3.5	Oxidation simulation results.....	29
4.4	Conclusion .....	38
5	Stress corrosion failure and related studies .....	40
5.1	Introduction.....	40
5.1.1	Stress corrosion cracking in alloys .....	41
5.1.2	Hydrogen embrittlement in metals .....	41
5.1.3	Stress corrosion cracking and fatigue in Al <sub>2</sub> O <sub>3</sub> based ceramics .....	42
5.2	Evaluation of elasticity, plasticity and fracture material properties .....	45
5.2.1	$\alpha$ -Al <sub>2</sub> O <sub>3</sub> .....	45
5.2.2	fcc-Al and fcc-Ni.....	50
5.3	$\alpha$ -Al <sub>2</sub> O <sub>3</sub> anisotropy and strain study.....	51

5.3.1	Structures.....	51
5.3.2	Method .....	52
5.3.3	Results and Analysis .....	52
5.4	Loading rate and relaxation study .....	56
5.4.1	Structures and Method .....	56
5.4.2	Results and Analysis .....	57
5.4.3	Summary .....	64
5.5	$\alpha$ -Al <sub>2</sub> O <sub>3</sub> fatigue study .....	64
5.5.1	Structures and Method .....	64
5.5.2	Results and Discussion .....	65
5.5.3	Summary .....	71
5.6	$\alpha$ -Al <sub>2</sub> O <sub>3</sub> stress corrosion study .....	71
5.6.1	Structures.....	71
5.6.2	Method .....	72
5.6.3	Results and Analysis .....	73
5.6.4	Summary .....	78
5.7	Extended time scale/steady state $\alpha$ -Al <sub>2</sub> O <sub>3</sub> study .....	78
5.7.1	Extended time scale crack propagation .....	79
5.7.2	Steady state stress corrosion study .....	82
5.8	fcc-Ni stress corrosion study.....	85
5.8.1	Structures and Method .....	85
5.8.2	Results and Discussion.....	86
5.8.3	Summary .....	94
5.9	fcc-Al hydrogen embrittlement study .....	95
5.9.1	Structures.....	95
5.9.2	Method .....	95
5.9.3	Results and Discussion.....	96

5.9.4 Summary .....	105
5.10 Conclusion and Outlook.....	106
References .....	107
Appendix A Annealing and oxidation of binary Mo <sub>3</sub> Ni-cluster.....	117
Appendix B Molecular dynamics simulation of Al grain mixing in Fe/Ni matrices and its influence on oxidation.....	119
Appendix C Dissertation related papers and conference presentations .....	124

## LIST OF FIGURES

Figure 2-1. Average stresses vs. time for Al <sub>2</sub> O <sub>3</sub> slab (33.8x4.9x101.7 Å) structure with a crack at T=300K: $\sigma_x$ (a), $\sigma_{xz}$ (b).....	7
Figure 3-1. Initial cluster configurations (a – 256-atom cluster, 50x50x50 Å, b – 1372-atom cluster, 85x85x85 Å, orange=Ni, green=Mo).....	16
Figure 3-2. Annealed cluster configurations, cut in the middle (a – 50x50x50 Å cluster, b – 85x85x85 Å cluster, grey=Mo, black=Ni).....	16
Figure 3-3. Bezier interpolated temperature and potential energy during the annealing cycle (a – 256-atom cluster, b – 1372-atom cluster).....	16
Figure 3-4. IGCRDF for Mo and Ni in the initial and annealed states (a – 256-atom cluster, b – 1372-atom cluster). .....	17
Figure 3-5. Bezier interpolated numbers of main Mo and Ni species vs. temperature during the cluster oxidation (a – 256-atom cluster, b – 1372-atom cluster).....	18
Figure 3-6. Cluster oxidation snapshots of the 256-atom cluster, cut in the middle, with oxygen molecules removed, corresponding to the temperature range of 2000-5500K. ....	19
Figure 3-7. Cluster oxidation snapshots of the 1372-atom cluster, cut in the middle, with oxygen molecules removed, corresponding to the temperature range of 2500-6000K. ....	19
Figure 3-8. Temperature, potential and total energy during the cluster oxidation (a – 256-atom cluster, b – 1372-atom cluster).....	19
Figure 4-1. Strain energy [kcal/mol] distribution for Fe (1 grain (a), 8 grains (c), 28.4x28.4x28.4 Å) and Ni (1 grain (b), 8 grains (d), 28.2x28.2x28.2 Å) matrix structures in the initial configuration at 300K. ....	31
Figure 4-2. Potential energy (a) and volume (b) vs. temperature for Fe matrix structures during heating.....	31
Figure 4-3. Potential energy (a) and volume (b) vs. temperature for Ni matrix structures during heating.....	31
Figure 4-4. Strain energy [kcal/mol] distribution for 1 Al grain in Fe matrix structure (28.4x28.4x28.4 Å) at different temperatures during heating.....	32
Figure 4-5. Strain energy [kcal/mol] distribution for 8 Al grains in Fe matrix structure (28.4x28.4x28.4 Å) at different temperatures during heating.....	32

Figure 4-6. Strain energy [kcal/mol] distribution for 1 Al grain in Ni matrix structure (28.2x28.2x28.2 Å) at different temperatures during heating. ....	33
Figure 4-7. Strain energy [kcal/mol] distribution for 8 Al grains in Ni matrix structure (28.2x28.2x28.2 Å) at different temperatures during heating. ....	33
Figure 4-8. Atomic hydrostatic stress [ $\text{Å}^3 \cdot \text{atm}$ ] distribution for 1 Al grain in Fe matrix structure (28.4x28.4x28.4 Å) at different temperatures during heating. ....	34
Figure 4-9. Atomic hydrostatic stress [ $\text{Å}^3 \cdot \text{atm}$ ] distribution for 8 Al grains in Fe matrix structure (28.4x28.4x28.4 Å) at different temperatures during heating. ....	34
Figure 4-10. Atomic hydrostatic stress [ $\text{Å}^3 \cdot \text{atm}$ ] distribution for 1 Al grain in Ni matrix structure (28.2x28.2x28.2 Å) at different temperatures during heating. ....	35
Figure 4-11. Atomic hydrostatic stress [ $\text{Å}^3 \cdot \text{atm}$ ] distribution for 8 Al grains in Ni matrix structure (28.2x28.2x28.2 Å) at different temperatures during heating. ....	35
Figure 4-12. Mean atomic hydrostatic stress vs. time for 1/8 Al grain Fe matrix structures during heating. ....	35
Figure 4-13. Mean atomic hydrostatic stress vs. time for 1/8 Al grain Ni matrix structures during heating. ....	36
Figure 4-14. Potential energy (a) and volume (b) vs. temperature for 1 Al grain Fe matrix structure during heating and cooling. ....	36
Figure 4-15. Potential energy (a) and volume (b) vs. temperature for 1 Al grain Ni matrix structure during heating and cooling. ....	36
Figure 4-16. Molten Fe matrix (28.4x28.4x28.4 Å) structure configuration snapshots before (1701K (a)) and after (1325K (b)) solidification (Fe – orange, Al – grey). ....	37
Figure 4-17. Molten Ni matrix (28.16x28.16x28.16 Å) structure configuration snapshots before (1515K (a)) and after (1084K (b)) solidification (Ni – green, Al – grey). ....	37
Figure 4-18. Fe matrix/1 Al grain structure (28.4x28.4x28.4 Å) oxidation simulation snapshots (Fe – black, Al – grey, O – red). ....	37
Figure 4-19. Ni matrix/1 Al grain structure (28.2x28.2x28.2 Å) oxidation simulation snapshots (Ni – black, Al – grey, O – red). ....	37
Figure 5-1. $\alpha\text{-Al}_2\text{O}_3$ (152.5x4.9x152.3 Å supercell) initial $\langle 00.1 \rangle \{ 10.0 \}$ crack configuration. ....	46
Figure 5-2. $\alpha\text{-Al}_2\text{O}_3$ (152.5x4.9x152.3 Å supercell) $\langle 00.1 \rangle \{ 10.0 \}$ crack propagation snapshots. ....	48
Figure 5-3. Al-Al (a), Al-O (b), O-O (c) radial distribution functions for bulk stretched structure samples (X1, X2 from red designated phase areas in Figure 5-16) and volume minimized $\text{Al}_2\text{O}_3$ unit cell (Xmin). ....	48

Figure 5-4. Uniform expansion equations of state of $\text{Al}_2\text{O}_3$ phases (a) and [10.0] expansion equation of state of $\alpha\text{-Al}_2\text{O}_3$ (b). .....	49
Figure 5-5. $\alpha\text{-Al}_2\text{O}_3$ (152.5x4.9x152.3 Å) [00.1] stretching with relaxation in [10.0]; configuration snapshots.....	49
Figure 5-6. $\alpha\text{-Al}_2\text{O}_3$ slab (33.8x4.9x101.7 Å) [10.0] stretching snapshots; octahedral stress distribution. ....	53
Figure 5-7. $\alpha\text{-Al}_2\text{O}_3$ slab (34.2x8.5x101.7 Å) [-12.0] stretching snapshots; octahedral stress distribution. ....	53
Figure 5-8. Potential energy (a) and tensile stress (b) vs. time: comparison for [10.0] and [-12.0] strained $\alpha\text{-Al}_2\text{O}_3$ slabs. ....	54
Figure 5-9. Maximum principal and octahedral strain distributions according to Green (a,c) and Almansi (b,d) strain tensors for [10.0] strained $\alpha\text{-Al}_2\text{O}_3$ slab (33.8x4.9x101.7 Å, $\epsilon=0.8$ ): distribution comparison.....	55
Figure 5-10. Mean maximum principal and octahedral strains according to Green and Almansi strain tensors for [10.0] strained $\alpha\text{-Al}_2\text{O}_3$ slab. ....	55
Figure 5-11. $\alpha\text{-Al}_2\text{O}_3$ slab (33.8x4.9x101.7 Å) [10.0] stretching snapshots; max. normal stress distribution. ....	58
Figure 5-12. $\alpha\text{-Al}_2\text{O}_3$ slab (33.8x4.9x101.7 Å) [10.0] stretching snapshots; charge distribution. ....	58
Figure 5-13. Potential energy (a) and tensile stress (b) vs. strain: comparison for [10.0] strained $\alpha\text{-Al}_2\text{O}_3$ slabs ( $1x=5e-6 \text{ fs}^{-1}$ ). ....	59
Figure 5-14. [10.0] strained $\alpha\text{-Al}_2\text{O}_3$ slab (33.8x4.9x101.7 Å) amorphization and re-crystallization snapshots; octahedral stress distribution. ....	59
Figure 5-15. $\alpha\text{-Al}_2\text{O}_3$ radial distribution upon amorphization and subsequent re-crystallization. ....	60
Figure 5-16. $\alpha\text{-Al}_2\text{O}_3$ slab (152.3x4.9x152.5 Å) [10.0] deformation with variable relaxation time; configuration snapshots.....	61
Figure 5-17. $\alpha\text{-Al}_2\text{O}_3$ slab (152.3x4.9x152.5 Å) [10.0] deformation with constant relaxation time; configuration snapshots.....	61
Figure 5-18. Potential energy (a) and tensile stress (b) vs. strain: loading regime comparison for [10.0] strained $\alpha\text{-Al}_2\text{O}_3$ slabs.....	61
Figure 5-19. [1-10] $5e-6 \text{ fs}^{-1}$ strained $\alpha\text{-Al}_2\text{O}_3$ -terminated fcc-Al slab (152.3x9.77x148.8 Å); configuration snapshots.....	62
Figure 5-20. [1-10] $5e-4 \text{ fs}^{-1}$ strained $\alpha\text{-Al}_2\text{O}_3$ -terminated fcc-Al slab (152.3x9.77x148.8 Å); configuration snapshots (Al – grey, O – red).....	63

Figure 5-21. Potential energy (a) and tensile stress (b) vs. strain for [1-10] strained $\alpha$ - $\text{Al}_2\text{O}_3$ -terminated fcc-Al slab: loading rate comparison ( $1 \times 5 \times 10^{-6} \text{ fs}^{-1}$ ).....	63
Figure 5-22. On-top (c,d) and fcc (a,b) $\alpha$ - $\text{Al}_2\text{O}_3$ /fcc-Al interface stacking (with respect to O) configurations prior to and after minimization (Al – grey, O – red).....	63
Figure 5-23. [10.0] strained $\alpha$ - $\text{Al}_2\text{O}_3$ slab (152.3x4.9x152.5 Å) snapshots; max. normal stress distribution. ....	66
Figure 5-24. Potential energy and tensile stress vs. strain for [10.0] strained $\alpha$ - $\text{Al}_2\text{O}_3$ slabs at 300K (a,b), $\epsilon_0=0.0$ , and at 0K with $\epsilon_0=0.07$ (c,d) and $\epsilon_0=0.0$ (e,f).....	67
Figure 5-25. Potential energy (a) and tensile stress (b) vs. time for [10.0] strained $\alpha$ - $\text{Al}_2\text{O}_3$ slab at 300K.....	68
Figure 5-26. [10.0] strained $\alpha$ - $\text{Al}_2\text{O}_3$ slab (152.3x4.9x152.5 Å) at 300K; configuration snapshots.....	69
Figure 5-27. [10.0] strained $\alpha$ - $\text{Al}_2\text{O}_3$ slab (152.3x4.9x152.5 Å) at 0K, $\epsilon_0=0.07$ ; configuration snapshots. ....	69
Figure 5-28. [10.0] strained $\alpha$ - $\text{Al}_2\text{O}_3$ slab (152.3x4.9x152.5 Å) at 0K, $\epsilon_0=0.0$ ; configuration snapshots. ....	70
Figure 5-29. Suggested [10.0] strained $\alpha$ - $\text{Al}_2\text{O}_3$ slab {10.-2} slip facilitated amorphization mechanism. ....	70
Figure 5-30. Vacuum placed $\alpha$ - $\text{Al}_2\text{O}_3$ slab (152.3x4.9x152.5 Å) [10.0] stretching snapshots: max. normal stress distribution. ....	73
Figure 5-31. $\text{H}_2\text{O}$ (a,b), Ne (c) and NVE/vacuum environment placed (d) $\alpha$ - $\text{Al}_2\text{O}_3$ slab (152.3x4.9x152.5 Å) [10.0] stretching snapshots: max. normal stress distribution. ....	74
Figure 5-32. Potential energy (a) and tensile stress (b) vs. strain for [10.0] strained $\alpha$ - $\text{Al}_2\text{O}_3$ slab: environment species/ensemble comparison. ....	75
Figure 5-33. Mean atomic octahedral (a) and max. normal (b) stress vs. strain for [10.0] strained $\alpha$ - $\text{Al}_2\text{O}_3$ slab: environment species/ensemble comparison. ....	76
Figure 5-34. Number of atom groups vs. time for $\text{H}_2\text{O}$ environment placed [10.0] strained $\alpha$ - $\text{Al}_2\text{O}_3$ slab.....	77
Figure 5-35. Bond breaking event distribution for [10.0] strained $\alpha$ - $\text{Al}_2\text{O}_3$ slab. ....	80
Figure 5-36. Coordination number (max=19, min=2) distribution for [10.0] strained $\alpha$ - $\text{Al}_2\text{O}_3$ slab (33.8x4.88x101.7 Å). ....	81
Figure 5-37. Relative energy (a) and number of $\text{H}_2\text{O}$ molecules (b) vs. iterations for GCMC/MD [10.0] strained $\alpha$ - $\text{Al}_2\text{O}_3$ slab. ....	84

Figure 5-38. Relative energy (a) and number of H <sub>2</sub> O molecules (b) vs. iterations for GCMC/MD [10.0] strained $\alpha$ -Al <sub>2</sub> O <sub>3</sub> slab: comparison of incremental runs with different numbers of iterations.....	84
Figure 5-39. Numbers of H <sub>2</sub> O molecule displacement moves and total number of H <sub>2</sub> O molecules vs. iterations for GCMC/MD [10.0] strained $\alpha$ -Al <sub>2</sub> O <sub>3</sub> slab.....	84
Figure 5-40. GCMC/MD [10.0] strained $\alpha$ -Al <sub>2</sub> O <sub>3</sub> slab (33.8x4.88x50.9 Å) configuration snapshots (Al – grey, O – red, H – white).....	85
Figure 5-41. Equilibration of fcc-Ni slab (29.8x8.6x30.4 Å) in vacuum (300K, 0 atm); configuration snapshots.....	86
Figure 5-42. [1-10] strained fcc-Ni slab (29.8x8.6x30.4 Å) in water (300K, P <sub>[11-2]</sub> =const); configuration snapshots (Ni – black, O – red, H – white).....	87
Figure 5-43. [1-10] strained fcc-Ni slab (29.8x8.6x30.4 Å) in water (300K, P <sub>[11-2]</sub> =const); octahedral Almansi strain distribution. ....	87
Figure 5-44. [1-10] strained fcc-Ni slab (29.8x8.6x30.4 Å) in water (300K, P <sub>[11-2]</sub> =const); octahedral stress distribution.....	88
Figure 5-45. Potential energy (a) and tensile stress (b) vs. strain for [1-10] strained fcc-Ni slab in water: boundary condition comparison.....	89
Figure 5-46. Potential energy (a) and tensile stress (b) vs. strain for [1-10] strained fcc-Ni slab: temperature and environment comparison. ....	90
Figure 5-47. [1-10] strained fcc-Ni slab (29.8x8.6x30.4 Å) in water (600K, dx <sub>[11-2]</sub> =const); dislocation planes. ....	91
Figure 5-48. [1-10] strained pre-oxidized fcc-Ni slab (29.8x8.6x30.4 Å) in vacuum (300K, dx <sub>[11-2]</sub> =const); step formation mechanism at $\epsilon=0.272$ . ....	91
Figure 5-49. Potential energy and strain vs. time for [1-10] strained pre oxidized fcc-Ni slab (300K, dx <sub>[11-2]</sub> =const): step formation transition.....	92
Figure 5-50. [1-10] strained pre-oxidized fcc-Ni slab (29.8x8.6x30.4 Å) in vacuum (300K, dx <sub>[11-2]</sub> =const); neck formation; octahedral stress distribution. ....	92
Figure 5-51. [1-10] strained fcc-Ni slab (29.8x8.6x30.4 Å) failure comparison (dx <sub>[11-2]</sub> =const): structures in water at 300K (a) and 600K (c) and structures in vacuum without pre-oxidation (b) and with pre-oxidized notch (d) (Ni – black, O – red, H – white).....	93
Figure 5-52. Reaction species and water pressure vs. time for [1-10] strained fcc-Ni slab in water: 300K systems with P <sub>[11-2]</sub> =const (a) and dx <sub>[11-2]</sub> =const (b) and a dx <sub>[11-2]</sub> =const system at 600K (c). ....	94

Figure 5-53. Potential energy (a) and tensile stress (b) vs. strain: comparison for [1-10] strained $\alpha$ -Al <sub>2</sub> O <sub>3</sub> -terminated fcc-Al slab (H1 - structure with initial H-filled vacancies, H2 - structure with bulk distributed H, without initial vacancies). .....	97
Figure 5-54. [1-10] strained $\alpha$ -Al <sub>2</sub> O <sub>3</sub> -terminated fcc-Al slab (152.3x9.77x148.8 Å); configuration snapshots (Al – grey, O – red). .....	97
Figure 5-55. [1-10] strained $\alpha$ -Al <sub>2</sub> O <sub>3</sub> -terminated fcc-Al slab (152.3x9.77x148.8 Å) with bulk distributed H, without initial vacancies; configuration snapshots (Al – grey, O – red, H – black).....	98
Figure 5-56. [1-10] strained $\alpha$ -Al <sub>2</sub> O <sub>3</sub> -terminated fcc-Al slab (152.3x9.77x148.8 Å) with initial H-filled vacancies; configuration snapshots (Al – grey, O – red, H – black).....	98
Figure 5-57. [1-10] strained $\alpha$ -Al <sub>2</sub> O <sub>3</sub> -terminated fcc-Al slab (152.3x9.77x148.8 Å) snapshots; max. normal stress distribution. ....	100
Figure 5-58. [1-10] strained $\alpha$ -Al <sub>2</sub> O <sub>3</sub> -terminated fcc-Al slab (152.3x9.77x148.8 Å) snapshots; octahedral Almansi strain distribution. ....	101
Figure 5-59. Comparison of bulk (a) and surface (b) 10-atom sample H diffusivities and mean square displacement in [1-10] strained $\alpha$ -Al <sub>2</sub> O <sub>3</sub> -terminated fcc-Al slab with bulk distributed H, without initial vacancies, at $\epsilon=0.37$ . ....	103
Figure 5-60. H diffusivity vs. tensile stress (a) and strain (b) in [1-10] strained $\alpha$ -Al <sub>2</sub> O <sub>3</sub> -terminated fcc-Al slab with bulk distributed H, without initial vacancies. ....	103
Figure 5-61. Potential energy (a) and tensile stress (b) vs. time: loading rate comparison for [1-10] strained $\alpha$ -Al <sub>2</sub> O <sub>3</sub> -terminated fcc-Al slab with bulk distributed H, without initial vacancies. ....	104
Figure 5-62. Relaxation of [1-10] strained $\alpha$ -Al <sub>2</sub> O <sub>3</sub> -terminated fcc-Al slab (152.3x9.77x148.8 Å) with bulk distributed H, without initial vacancies, at $\epsilon=0.17$ ; configuration snapshots at 280 ps (a) and 550ps (b) (Al – grey, O – red, H – black).....	105
Figure A-1. IRDF for Mo and Ni atoms in the initial (lattice) and annealed states (a – 256-atom cluster, b – 1372-atom cluster).....	117
Figure A-2. IRDF for Mo atoms with respect to Mo and Ni atoms separately in the initial (lattice) and annealed states (a – 256-atom cluster, b – 1372-atom cluster).....	117
Figure A-3. IRDF for Ni atoms with respect to Mo and Ni atoms separately in the initial (lattice) and annealed states (a – 256-atom cluster, b – 1372-atom cluster).....	118
Figure A-4. Bezier interpolated numbers of MoO <sub>x</sub> and NiO <sub>x</sub> species vs. temperature during the cluster oxidation (a – 256-atom cluster, b – 1372-atom cluster).....	118
Figure B-1. RDF of Al-Al (a), Fe-Fe (b), Fe-Al (c) and IRDF of Fe-Al (d) for 1 Al grain in Fe matrix structure during heating. ....	119

Figure B-2. RDF of Al-Al (a), Fe-Fe (b), Fe-Al (c) and IRDF of Fe-Al (d) for 8 Al grains in Fe matrix structure during heating. ....	120
Figure B-3. RDF of Al-Al (a), Ni-Ni (b), Ni-Al (c) and IRDF of Ni-Al (d) for 1 Al grain in Ni matrix structure during heating. ....	120
Figure B-4. RDF of Al-Al (a), Ni-Ni (b), Ni-Al (c) and IRDF of Ni-Al (d) for 8 Al grains in Ni matrix structure during heating. ....	121
Figure B-5. Standard deviation of atomic hydrostatic stress vs. time for 1/8 Al grain Fe matrix structures during heating. ....	122
Figure B-6. Standard deviation of atomic hydrostatic stress vs. time for 1/8 Al grain Ni matrix structures during heating. ....	122
Figure B-7. RDF of Al-Al (a), Fe-Fe (b), Fe-Al (c) and IRDF of Fe-Al (d) for molten 1 Al grain in Fe matrix structure during cooling. ....	123
Figure B-8. RDF of Al-Al (a), Ni-Ni (b), Ni-Al (c) and IRDF of Ni-Al (d) for molten 1 Al grain in Ni matrix structure during cooling. ....	123

## LIST OF TABLES

Table 4-1. Atomic percentage of Al in Fe/Ni-Al matrix/grain structures.....	30
Table 4-2. Characteristic temperatures and bond distances of Ni, Fe, Al.....	30
Table 4-3. Estimates of melting points (K).....	32
Table 5-1. $\alpha$ -Al <sub>2</sub> O <sub>3</sub> elastic constants and fracture toughness values.....	48
Table 5-2. fcc-Al elastic constants, fracture toughness values, intrinsic and unstable stacking fault energies. ....	51
Table 5-3. fcc-Ni elastic constants, fracture toughness values, intrinsic and unstable stacking fault energies. ....	51
Table 5-4. Ensemble settings for $\alpha$ -Al <sub>2</sub> O <sub>3</sub> slab loading rate study.....	57
Table 5-5. 1 <sup>st</sup> and 2 <sup>nd</sup> loading cycle failure strains, stresses and potential energies for [10.0] strained $\alpha$ -Al <sub>2</sub> O <sub>3</sub> slab.....	66
Table 5-6. Parallel replica dynamics event statistics for [10.0] strained $\alpha$ -Al <sub>2</sub> O <sub>3</sub> slab. ....	81
Table 5-7. H diffusivity comparison for fcc-Al. ....	103

## **ACKNOWLEDGEMENTS**

This material is based upon work supported by the Department of Energy.

Gratitude is expressed to friends and relatives for support.

Special thanks to all committee members and dissertation advisor in particular.

# 1 Introduction

## 1.1 Materials for coal combustion applications

Current coal combustion technologies are known to have insufficient energy production efficiency and high CO<sub>2</sub> emissions. To tackle this problem, several new technologies have been proposed. These include oxy-fuel ‘zero-emission’ gas turbine power plants, featuring high-pressure combustion of fuel mixture with oxygen in the presence of recycled coolant to produce drive gases composed predominantly of steam and CO<sub>2</sub>, advanced gasification systems, advanced ultra-supercritical steam systems, advanced turbine systems and advanced carbon capture systems [1, 2].

These new technologies require structural materials that would be capable of operating at temperatures as high as 1760°C and pressures as high as 4.14 MPa [3]. The performance of the materials in such environments will strongly depend on the interactions that occur at surfaces. For example, the performance of structural components (such as a boiler tube or a turbine blade, etc.) will be affected by surface oxidation and corrosion processes. Excessive oxidation and corrosion may not only limit the life expectancy, but underlying changes to the material’s microstructure may also compromise the mechanical integrity of the component. Therefore, understanding surface phenomena and engineering cost-effective materials that can withstand or control these processes is of paramount importance for the development of advanced engineering systems.

Common protective surface oxides, like Cr<sub>2</sub>O<sub>3</sub>, Al<sub>2</sub>O<sub>3</sub>, SiO<sub>2</sub>, provide oxidation resistance up to temperatures of about 1400°C for Al<sub>2</sub>O<sub>3</sub> protective surfaces at 1 MPa [4]. Therefore, to meet the new requirements for structural materials, new durable thermal barrier coatings (TBCs) and high temperature oxidation and creep resistant metal substrates/structural alloys are to be developed. Complex materials structures, e.g., multi-component or multi-phase materials, offer distinct advantages over single

component or single phase materials, as the properties of complex structures can be tailored or tuned by the appropriate combination and distribution of elements, constituents, or phases.

According to [5], the main difficulties in developing refractory alloys are lack of basic experimental data on thermodynamic, mechanical and physical properties of most of the alloy systems, and difficulties associated with processing of these alloys. In order to avoid traditional trial-and-error experiments, which are also time consuming and expensive, it has become essential to develop theoretical modeling to guide experimental alloy development. Such theoretical modeling can be multiscale in nature, which includes first principles, density functional theory (DFT) ab initio based calculations, and atomistic, mesoscale and continuum simulations.

## 1.2 Methods

Due to their interpretative and predictive capacities, ab initio calculations are widely employed to study alloy properties, such as lattice stability, interfacial energies and defect structures. Current computational capabilities allow DFT MD calculations for systems of a few hundreds atoms, being too slow for simulations of liquids [6]. In contrast, the reactive empirical force field (FF) ReaxFF can simulate reactive systems of more than million atoms for periods of nanoseconds or longer [7, 8]. Therefore for the reactive atomistic level simulations, which are the main focus of the thesis, ReaxFF was used [9].

## 2 Simulation and analysis methods

### 2.1 Reactive force field ReaxFF

The reactive force field ReaxFF [9] divides the potential energy of the system into various partial energy contributions, including bonding, over- and under-coordination, valence angle, penalty (for systems with two double bonds sharing an atom in a valence angle), torsion angle, conjugation (for systems with regions of overlapping p-orbitals), van der Waals and Coulomb energies. The implementation of the energy terms is described below.

The bond order between a pair of atoms is obtained directly from the interatomic distance. The bond orders are corrected for over-coordination and for residual 1-3 bond orders in valence angles, if applicable. The bonding energy is calculated as a function of bond orders.

After correction of the original bond orders a degree of over-coordination may remain in the molecule. Therefore the over-coordination energy imposes an energy penalty on the system as a function of the degree of deviation of the sum of the corrected bond orders around an atomic center from its valence. The form of the function ensures that over-coordination energy quickly vanishes to zero for under-coordinated systems.

For an under-coordinated atom the energy contribution for the resonance of the  $\pi$ -electron between attached under-coordinated atomic centers is taken into account. This is done if the bonds between an under-coordinated atom and its under-coordinated neighbors partly have  $\pi$ -bond character.

Similarly to other energy terms, the energy contribution from valence angle terms goes to zero as the bond orders in the valence angle go to zero. The effects of over/under-coordination in the central atom on the valence angle energy are taken into account. The equilibrium angle depends on the sum of  $\pi$ -bond orders around the central atom.

The torsion angle energy definition also accounts for the involved atom bond orders. A valence-angle-dependent term ensures that the torsion energy contribution disappears when either of the two valence angles approaches  $\pi$ .

To account for repulsive interactions at short interatomic distances due to Pauli exclusion principle and attraction energies at long distances due to dispersion, non-bonded interaction energies are defined. These interactions, corresponding to van der Waals and Coulomb forces, are included for all atom pairs, thus avoiding abrupt alterations in the energy description during bond dissociation. For the van der Waals interactions a distance-corrected Morse-potential is used. By including a shielded interaction excessively high repulsions between bonded atoms (1-2 interactions) and atoms sharing a valence angle (1-3 interactions) are avoided. To adjust for orbital overlap between atoms at close distances a shielded Coulomb potential is used to account for the Coulomb (electrostatic) interactions. Atomic charges are calculated using the Electron Equilibration Method (EEM) approach [10]. According to it, the effective electronegativity of an atom in a molecule, which is equal to the molecular electronegativity, is expressed as a function of electronegativity and hardness of the neutral atom, as well as charges and interatomic distances between the atoms in the molecule. The electronegativity and hardness of an atom are defined as the first and second derivatives, respectively, of the total molecular energy with respect to the number of electrons associated with the atom.

The energy component definitions above allow estimating the total potential energy contribution for each atom in a structure, which enables detailed analysis of energy distribution in a structure.

## 2.2 Simulation methods

For the studies presented in sections 3 and 4 the ReaxFF ADF [11] implementation was used, whereas for the rest of studies the ReaxFF LAMMPS [12] implementation was used.

### 2.2.1 ReaxFF ADF settings

For static calculations the conjugate gradient minimization was used. For the dynamic calculations the Verlet velocity algorithm [13] was used to solve the Newtonian equations of motion. The MD calculations were performed either with NVE (constant system size-volume-energy) or microcanonical, NVT (constant system size-volume-temperature), a.k.a. canonical, and NPT (constant system size-pressure-temperature) ensemble conditions. Velocity and system volume scaling (for NVT and NPT ensembles, respectively) were performed using the Berendsen method [14]. The main user choice for this method is the setting of the damping constants, which determine the strength of coupling between the system and an external velocity (heat) or volume (pressure) bath. High coupling ( $<100 \cdot t_{\text{step}}$  for NVT,  $<1000 \cdot t_{\text{step}}$  for NPT [12]) may cause unphysical velocity distribution of the system.

### 2.2.2 ReaxFF LAMMPS settings

The number of atoms was kept constant in all simulations. All structures were initially potential energy minimized, using a conjugate gradient based method with a root mean square force per atom tolerance  $0.25 \text{ kcal/mol}/\text{\AA}$  or a relative energy change between successive iterations less than  $1e-7$ . When applicable, volume minimization to 0 atm pressure was performed. For the equilibration of structures the constant pressure-temperature (NPT) ensemble with anisotropic pressure equilibration was applied. The simulation step size was 0.2 fs due to the assumed order of magnitude for vibrational frequencies of H atoms (vibration period of 7.4 fs for  $\text{H}_2$  [15]) and energy conservation requirements [16]. The tension was applied by scaling the respective axis dimension and atom positions in every iteration to simulate the selected engineering strain rate. Due to the expected rise in temperature as a result of deformation energy input and requirement for maintaining constant pressure conditions when applicable, the constant volume

and energy (NVE) ensemble was not applicable for the presented studies and NVT/NPT pre-equilibrated systems were used.

The Nose-Hoover thermo- and barostats, coupled with equations of motion in velocity Verlet formulation [13], were used for the simulations. 3 chain thermostats were used for pressure equilibration, unless noted otherwise. For shock loading rates a reversible multiple time scale molecular dynamics algorithm implementation for the integration of equations of motion [17] was used in some deformation simulations. In this implementation, position-dependent deformation velocity is subtracted from each atom's actual velocity to yield a thermal velocity which is used for temperature computation and thermostatting. Thus in the latter method the atom velocities instead of coordinates are being modified.

The rest of the settings were selected specifically for each simulation.

### 2.3 Stress analysis

For qualitative stress analysis the octahedral (equation 1) and maximum principal stress criteria, commonly related to ductile/shear and brittle failure of materials [18], resp., were used. Both the atomic distributions of the criteria and mean values of the atomic criteria values were considered.

$$\sigma_{oct} = \frac{1}{3} \sqrt{(\sigma_1 - \sigma_2)^2 + (\sigma_1 - \sigma_3)^2 + (\sigma_3 - \sigma_2)^2}, \quad (1)$$

where  $\sigma_{1,2,3}$  – principal stresses.

Due to the definition of virial stress (equation 2) in units of stress times atomic volume [19], only relative comparison of the obtained atomic stress values was done. Yet, according to derivation in [19], the virial stress generally should be interpreted in volume and time averaged sense, which tentatively justifies the approach taken.

$$\boldsymbol{\sigma}_{virial} = \frac{1}{\Omega} \left( -m_i \dot{\mathbf{u}}_i \otimes \dot{\mathbf{u}}_i + \frac{1}{2} \sum_{j(\neq i)} \mathbf{r}_{ij} \otimes \mathbf{f}_{ij} \right), \quad (2)$$

where  $\Omega$  – volume around particle  $i$ ,  $\mathbf{u}_i$  – displacement of  $i$  with respect to reference position,  $\mathbf{r}_{ij} = \mathbf{r}_i - \mathbf{r}_j$ ,  $\mathbf{r}_i$  – position of  $i$ ,  $\mathbf{f}_{ij}$  – force on particle  $i$  by particle  $j$ .

Due to the observed differences between sums of atomistic stresses, as defined in [12], and overall system stress components [19] it was established that for numerical analysis the overall stress values could be considered more reliable for fluids in particular. However, for estimation of stresses in specific parts of a system, e.g., overall stress on a slab, the atomic stresses had to be used, which poses the requirement for estimation of atomic volume. Considering the slab as close to incompressible due to its macroscopically brittle nature at room temperature [20, 21], the total slab volume estimate was based on the initial volume size. Yet caution should be exercised upon evaluation of individual atom stress tensor values due to balance requirements in multi-element structures (Figure 2-1).

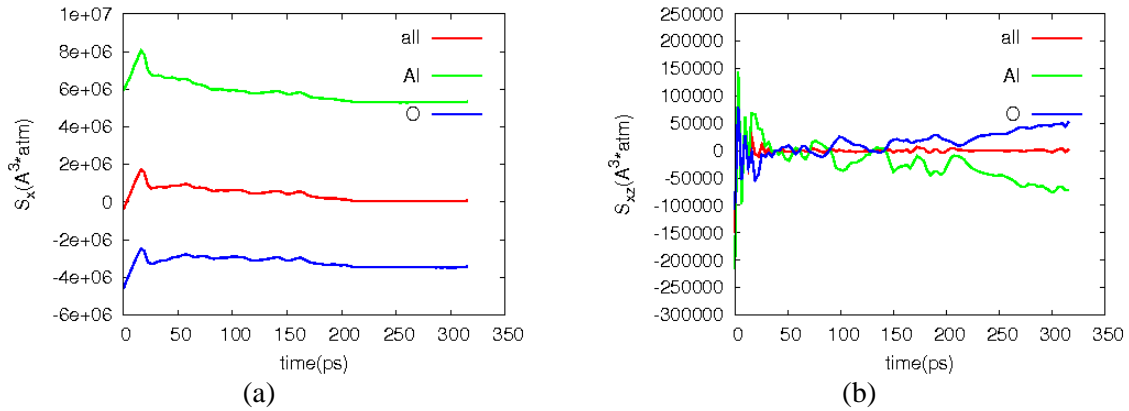


Figure 2-1. Average stresses vs. time for Al<sub>2</sub>O<sub>3</sub> slab (33.8x4.9x101.7 Å) structure with a crack at T=300K:  $\sigma_x$  (a),  $\sigma_{xz}$  (b).

Since only the part of the virial stress for atomic systems (equation 2) which depends on the interatomic forces and atom positions is relevant for the estimation of the equivalent of the Cauchy stress [22], its kinetic component, corresponding to momentum transfer in the spatial description of the balance of momentum [22], was not included in the atomic stress calculation.

## 2.4 Strain distribution calculation

A kinematic algorithm, presented in [23], was implemented for the calculation of Almansi and Green continuum strain tensors from atomistic simulation data. The choice was based largely on its lower computational cost and consistence with continuum predictions [23], including compatibility of configurations, characterized by zero curl of deformation gradient in most instances [24]. According to the algorithm, the discrete, incremental form of the deformation gradient emerges from a weighted least squares minimization that includes a length scale relating the distance from the atom in question with a particular cutoff radius. A modification to the equation (26) in [23] was made by replacing the first nearest neighbor distance by zero due to the need for capturing separation of newly formed gas phase species from the bulk. A step weight function was used due to finding that weight functions with non-zero spatial gradient may cause incorrect results because of thermal fluctuations [23]. The weight values were updated for each incremental deformation gradient calculation. Thus a piecewise linearized quasi-continuum strain history dependent characterization of the deformation was obtained.

In analogy with stress criteria analysis, the maximum principal and octahedral strains [18] were used for strain analysis. The approach also allows avoiding the effects of different principal strain directions for Green and Almansi strains [23, 25]. For strain analysis in metallic structures under plastic deformation the Almansi octahedral strain was applied due to its suitability for large strain shear deformation analysis.

## 2.5 Slip vector analysis

For identification of particular dislocation directions the slip vector calculation method [26] was implemented. Although it provides additional data compared to the strain tensor analysis and is computationally inexpensive due to its linear averaging definition, its dependence on particular reference

configurations renders it inapplicable for obtaining cumulative strain history evaluation, which is possible with the nonlinear incremental definition of strain tensor (section 2.2).

## 2.6 Centrosymmetry parameter and coordination number calculation

For crystalline structures symmetry dependent parameters can be applied for identification of structural defects. In particular, for structures with inversion symmetry the centrosymmetry parameter can be calculated in order to identify and distinguish between different types of defects [27, 28].

Alternatively, structural defects can be identified by comparison of coordination numbers against the analogues for ideal crystalline structures [28, 29].

## 2.7 Fracture toughness calculation

Although the applicability of linear elastic fracture mechanics (LEFM) and strain energy release rate (SERR) concepts is limited by the amount of acceptable level of plastic deformation [18] and flaw tolerance limit due to reduced dimensions of the structures at nanoscale [30], several studies have revealed results that indicate agreement between continuum and atomistic calculations for grapheme sheets. E.g., in [31] the SERL has been evaluated by calculation of  $J$ -integral and is found to agree with surface energy calculation up to 10%. Instead, in [32] the SERR has been calculated directly by global energy or crack closure methods, the result being in agreement with LEFM and finite element method (FEM) calculations.

For the current study the fracture toughness was expressed as a function of strain energy release rate during crack propagation (equation 3), according to LEFM [18], from static simulations, performed by incremental minimization.

$$G = \frac{\Delta E_{loss}}{t\Delta a}; \Delta E_{loss} = \Delta E_{pot} - V_0 \int_{\Delta \varepsilon} \sigma d\varepsilon, \text{ where} \quad (3)$$

$t$  – slab thickness,  $\Delta a$  – crack length change,  $V_0$  – initial material volume,  $\sigma$  – tensile stress.

## 2.8 Postprocessing per-atom data

For displaying any per-atom properties with real or integer values custom coloring schemes can be readily applied [33]. Since most of the atomic output quantities described above typically involve large data value scatter, for visualization purpose the data may require defining custom color map ranges. For the atomic value plots in this study the coloring reference value ranges, unless noted otherwise, were defined as

$$\max[E(x) - \sigma(x) \quad \inf x] \leq x_{plot} \leq \min[E(x) + \sigma(x) \quad \sup x], \text{ where} \quad (4)$$

$x$  – scalar value to be plotted,  $E(x)$  – mean of  $x$ ,  $\sigma(x)$  – standard deviation of  $x$ .

## 2.9 Used terminology

For identifying the failure mechanisms in the observed material transformation processes upon deformation, the following general definitions were referred to:

- material strength as ultimate or fracture stress value [18]
- kinematic strain hardening as loading direction dependent increase in stress after yielding with the assumption that yielding in the reverse direction occurs when the stress change from unloading point is twice the monotonic yield stress [18]
- shakedown as a transition from elasto-plastic to purely elastic deformation under time-variable loading [34]

- crack formation as an atomistically sharp, possibly branched, tip and surface forming process due to bond cleavage
- crack healing as small void/crack closing process due to formation of bonds between initially separated surfaces
- stress corrosion as enhancement of material oxidation/dissolution processes in chemically reactive environments in mechanically strained state
- amorphization as a transition from crystalline to a non-periodic/disordered material structure
- fatigue as material strength degradation upon cyclic loading
- static fatigue/creep as finite timescale [35] / subcritical stress level [36] material strength degradation upon monotonic/static loading
- embrittlement as a reduction in ductility of a material, quantified by reduction in either [18] of
  - fracture strain – requires a standardized aspect ratio for comparison
  - percent reduction in specimen cross-section area at fracture point
- material's energy capacity or tensile toughness, defined as the volume normalized work done in deforming the material up to fracture, attributed to a combination of material's strength and ductility properties [18]. In the presented studies the strained material's energy capacity is comparatively estimated by the potential energy values at fracture or ductile failure points (see also section 2.7).

## 2.10 Crystallographic notation

For the designation of crystallographic directions and planes the Miller indices for orthogonal (bcc/fcc metals) and 4-axes hexagonal ( $\alpha$ -Al<sub>2</sub>O<sub>3</sub>) lattices [37] have been used, with a simplification for the minus sign notation that is occasionally found in literature [38].

### 3 Annealing and oxidation of binary Mo<sub>3</sub>Ni clusters

#### 3.1 Introduction

Currently used high operating temperature structural materials include Ni base superalloys, which are characterized by combination of corrosion resistance [39] and mechanical strength up to temperatures of about 800 deg C [40]. Potential constituents for new alloys are elements with higher melting point (m.p.) and higher stiffness than Ni (m.p. 1453 deg C [41],  $E = 200$  GPa). A particular choice could be Mo (m.p. 2610 deg C [41],  $E = 329$  GPa), which is a well-known Ni based alloy constituent beside Cr (m.p. 1890 deg C [41],  $E = 279$  GPa) [42, 43]. Accordingly, Mo<sub>3</sub>Ni represents a potential structural alloy for high temperature applications.

We have performed a comparative study of 256- and 1372-atom face-centered cubic (FCC) Mo<sub>3</sub>Ni cluster oxidation using Molecular Dynamics (MD) [13] with NVT (constant number of atoms, volume and temperature) and NVE (constant number of atoms, volume and energy) ensemble conditions. The main goal of the current study was finding evidence of segregation mechanisms in Mo<sub>3</sub>Ni cluster annealing process and qualitative analysis of the annealed cluster oxidation dynamics/kinetics and products.

A comparative study of surface segregation in bimetallic Pt-Ni, Pt-Re and Pt-Mo alloy nanoparticles has been done by [44], revealing different segregation mechanisms, including a surface-sandwich structure, core-shell structure and a more specific structure for Pt<sub>80</sub>Mo<sub>20</sub> nanoparticles. The competition between surface segregation and compositional ordering in alloys from theoretic and experimental point of view has been considered by [45], which states that order-segregation competition in ordered alloys and solid solutions, attributed to subtle balance of segregation driving-forces and interaction strength, can be manifested in peaked segregation versus temperature curves.

## 3.2 Method

The [46] version of the ReaxFF force field for Mo/Ni/C/O/N/S/H systems was used in the study.

### 3.2.1 Initial minimization

256- and 1372-atom FCC Mo<sub>3</sub>Ni clusters were initially energy minimized by the conjugate gradient based method. The end point criterion for convergence - root mean square gradient (RMSG) - was set equal to 4.0 kcal/mol/Å since we only needed a local minimum for the subsequent annealing simulation. Figure 3-1 shows the initial cluster configurations.

### 3.2.2 Annealing

The clusters were first equilibrated at the temperature of 300K, which was the starting temperature for the annealing cycle. The MD simulation step size was .25 fs and the 1st temperature damping constant for the Berendsen thermostat (BTDC) [14] was set equal to 100 fs. The annealing cycle used a MD step size of 1.0 fs included stages of linear ramp of .037 K/fs up to the temperature of 4000K, a constant period of 150000 fs and a reversed ramp back to 300K (Figure 3-3). For the 1372-atom cluster a second identical annealing cycle was simulated.

### 3.2.3 Oxidation

Prior to the oxidation simulation the clusters were equilibrated at a temperature of 1500K using a MD step size of .1 fs and BTDC of 100 fs. During the main oxidation simulation a weak damping was maintained by setting BTDC to 25000 fs, making these simulations essentially NVE-simulations.

Additional simulation settings include periodic box sizes of 50x50x50 Å for the 256-atom cluster and 85x85x85 Å for the 1372-atom cluster, 500 oxygen molecules for the 256-atom cluster and 2500 oxygen molecules for the 1372-atom cluster, giving number density of .2 kg/l for both clusters. The number of oxygen molecules exceeded the stoichiometric amounts, estimated with respect to NiO and MoO<sub>3</sub>/MoO<sub>2</sub> as 320/224 for the 256-atom cluster and 1715/1201 for the 1372-atom cluster, respectively.

### 3.2.4 Radial distribution definitions

For analysis of the annealing simulation results two functions were used: the integral of the overall radial distribution function (IRDF) and the integral of radial distribution function defined with respect to the geometric centers of the Mo<sub>3</sub>Ni clusters (IGCRDF).

## 3.3 Results and discussion

### 3.3.1 Annealing

Figure 3-2 shows the cluster configurations after the anneal cycle. The IGCRDF changes after initial minimization, equilibration and annealing (Figure 3-4) show that Mo atoms have shifted towards the cluster center, whereas the Ni atoms have shifted towards the outer surface of the cluster, similarly to the result for Pt<sub>75</sub>Re<sub>25</sub> nanoparticles [44], reported to have a nearly pure Pt shell surrounding a more uniform Pt–Re core. These changes could be attributed to the differences of cohesive energy (defined as  $E_{\text{crystal}} - E_{\text{atoms}}$ ) between Mo and Ni, which are -598 kJ/mol for bulk Mo [47] and about -428 kJ/mol for Ni (-428.39 kJ/mol by experiment, -436.11 kJ/mol by PW (Perdew et al.) functional, -417.78 kJ/mol by BP (Becke-Perdew) functional and -576.98 kJ/mol by LDA (local-density approximation) [48]). Figure 3-3

indicates that the segregation process that takes place yields an energetically more favorable configuration.

Comparison of IGCRDF for two consecutive 1372-atom cluster annealing cycles indicated that the second annealing cycle had yielded no significant change in the cluster configuration. For this reason, we concluded that the first cycle had produced close to a globally minimized configuration.

The IRDF calculations for Mo and Ni atoms with respect to all cluster atoms (Figure A-1) show that annealing yields fairly homogeneous diffusion of the respective atoms. Also, the average IRDF values of the first coordination shell (below distance of 4 Å) for Ni decrease, whereas for Mo the respective values increase, which is in accord with the segregation mechanism discussed above. Similar observations can be made from the IRDF plots for Mo atoms with respect to Mo and Ni atoms separately (Figure A-2), which seems reasonable since Mo atoms constitute the majority of the cluster atoms. However, for Ni atoms (Figure A-3) it is the average IRDF values of the first coordination shell with respect to Mo atoms that decrease, whereas for Ni-Ni atoms the respective values increase. This can be attributed again to the segregation mechanism discussed above. Another observation is that the average interatomic distance with respect to Mo atoms after annealing is greater than that with respect to Ni atoms. This could be attributed both to the segregation and the different bulk interatomic distances for pure Mo and Ni crystals, which are 2.72 Å [49] and 2.492 Å [50] (2.73 Å and 2.55 Å in ReaxFF), respectively.

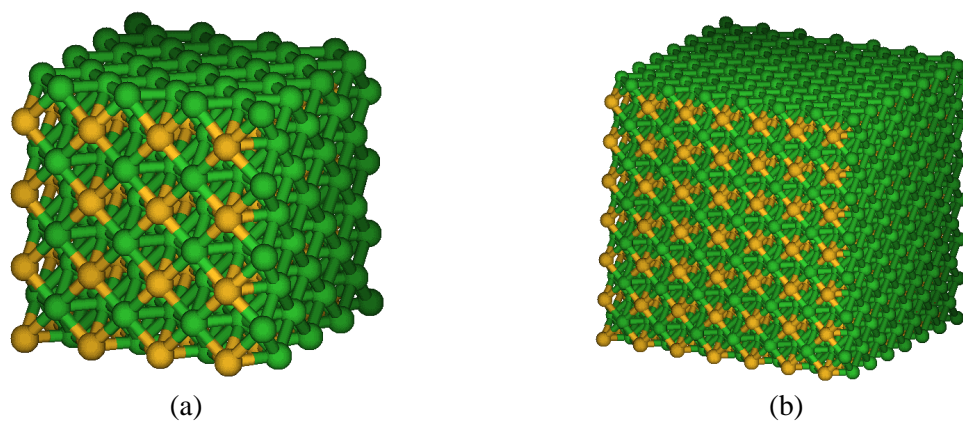


Figure 3-1. Initial cluster configurations (a – 256-atom cluster, 50x50x50 Å, b – 1372-atom cluster, 85x85x85 Å, orange=Ni, green=Mo).

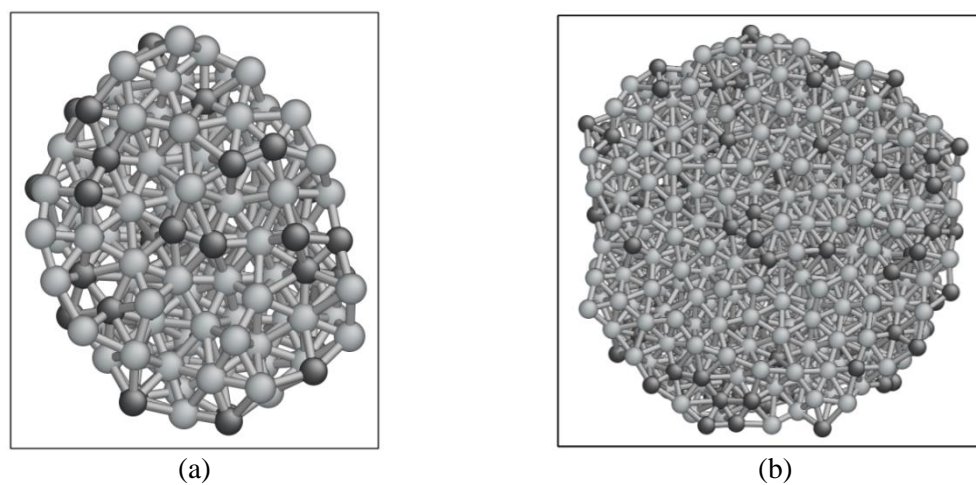


Figure 3-2. Annealed cluster configurations, cut in the middle (a – 50x50x50 Å cluster, b – 85x85x85 Å cluster, grey=Mo, black=Ni).

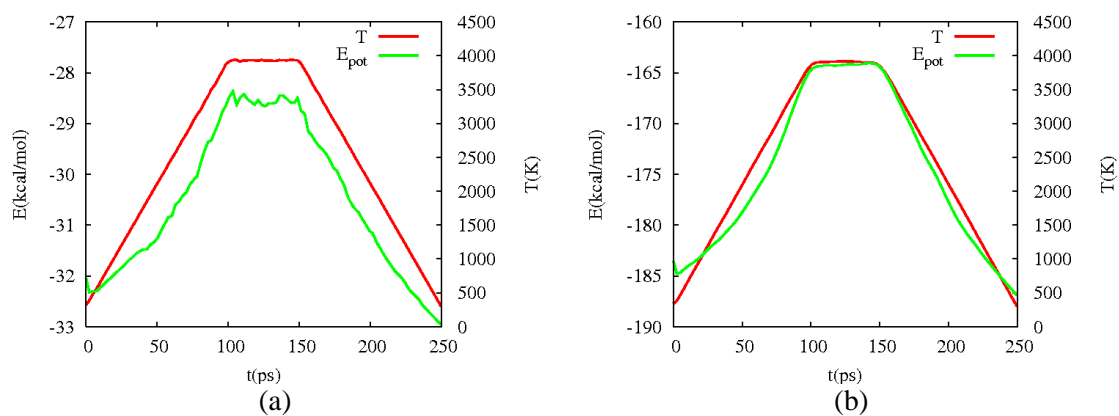


Figure 3-3. Bezier interpolated temperature and potential energy during the annealing cycle (a – 256-atom cluster, b – 1372-atom cluster).

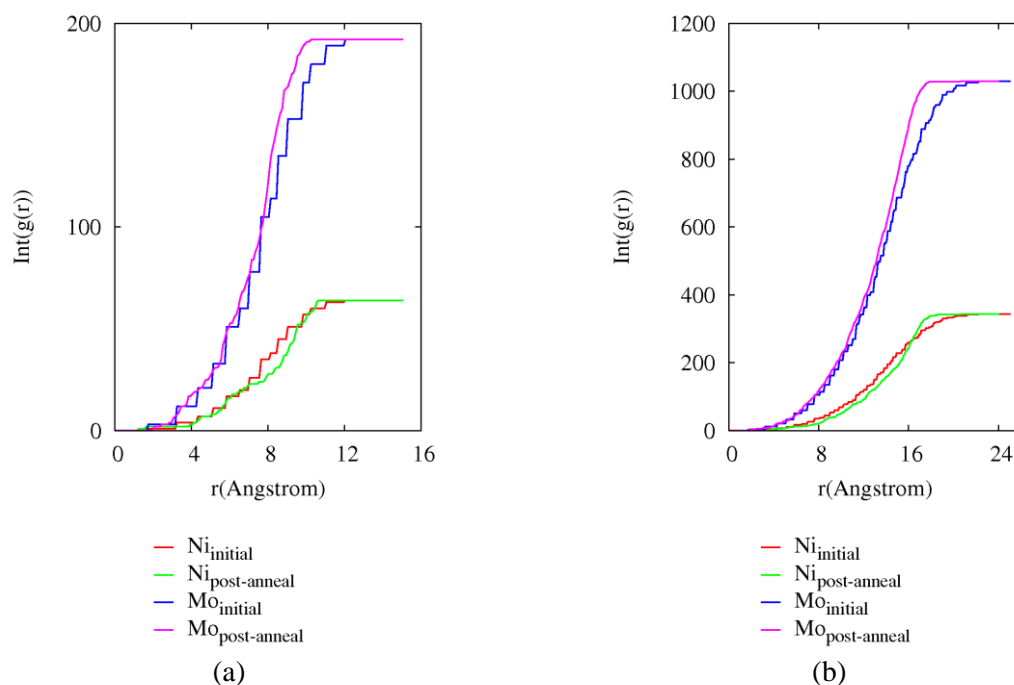


Figure 3-4. IGCRDF for Mo and Ni in the initial and annealed states (a – 256-atom cluster, b – 1372-atom cluster).

### 3.3.2 Oxidation

Figure A-4 shows the generation of  $\text{MoO}_x$ ,  $\text{MoNiO}_x$  and  $\text{NiO}_x$  species as a function of simulation temperature. As a general trend for all main product species (Figure 3-5) two stages in the process can be observed. The first one corresponds to the first major occurrence of main product species - Mo and Ni oxides, including mixed Mo-Ni species. It occurs approximately between temperatures of 2000-3000K, which is in the range of Ni and Mo melting points (1726K and 2895K [41], respectively), as well as melting and boiling points of NiO (2263K/2623K [51]) and  $\text{MoO}_2$  (~1823K/1973K [51]). The second corresponds to a steep increase of the main product species, which starts between temperatures of 3000-3500K and is close to the Ni boiling point (3157K [41]). The correlation with Ni boiling point temperature could be related to the numeric dominance of Ni atoms on the cluster outer surfaces. The plots also show dominance of Mo oxides product species, which is significantly greater than the Mo atom

numeric dominance (3:1). The low concentrations of Ni/O species in particular could be due to higher stability of Mo oxides ( $\text{MoO}_2$ ,  $\text{MoO}_3$ ) (which form several strong double bonds) compared to Mo/Ni/O clusters (Figure 11) and NiO especially (since it can only form a single weak double bond).

Graphical simulation snapshots for the 256-atom cluster (Figure 3-6) confirm the observed species concentration changes by showing a discernible migration of oxygen atoms towards the center of the cluster at around 3300K and larger amounts of small-sized product species at around 4600K. At about 5300K there is no distinct cluster bulk structure to be seen. From the simulation snapshots for the 1372-atom cluster (Figure 3-7) it can be clearly observed that the oxygen atoms tend to build bonds mostly with Mo-surface atoms and consequently the majority of product species are indeed Mo oxides.

Results show that the total energy increases approximately simultaneously with the concentration of oxidation products (Figure 3-5, Figure 3-8). This does not seem to be affected by reducing the iteration step size from .1 fs to .05 fs and .025 fs. Thus the lack of total energy conservation could be attributed to weak damping setting.

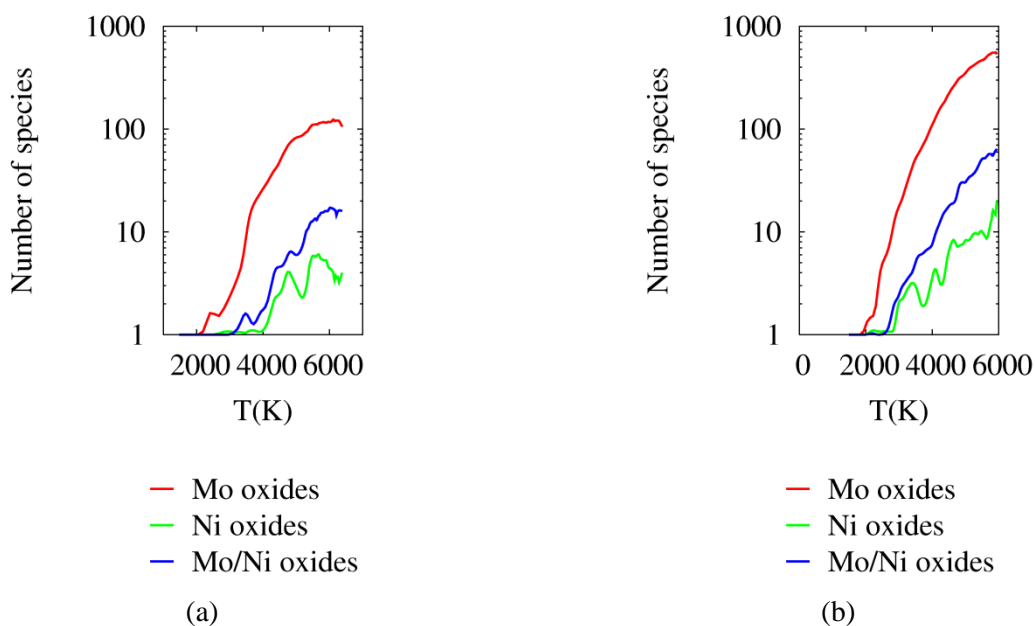


Figure 3-5. Bezier interpolated numbers of main Mo and Ni species vs. temperature during the cluster oxidation (a – 256-atom cluster, b – 1372-atom cluster).

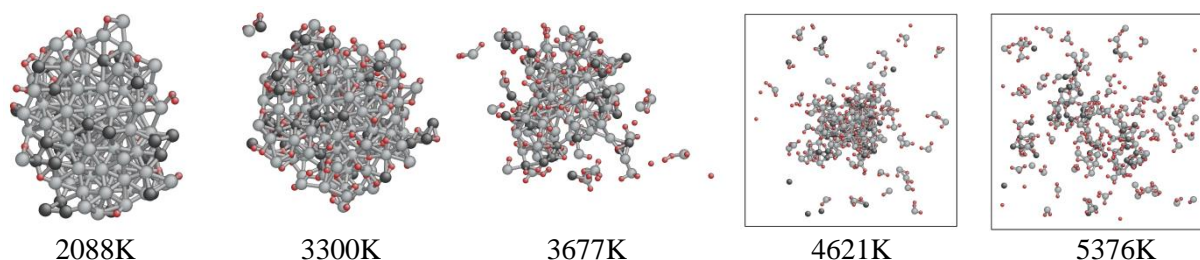


Figure 3-6. Cluster oxidation snapshots of the 256-atom cluster, cut in the middle, with oxygen molecules removed, corresponding to the temperature range of 2000-5500K.

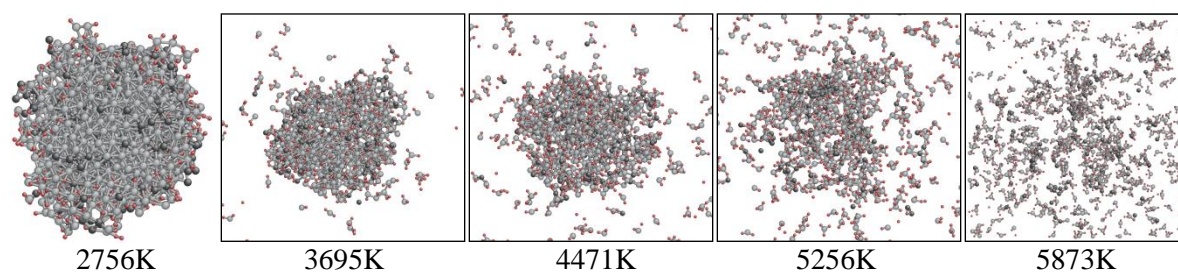


Figure 3-7. Cluster oxidation snapshots of the 1372-atom cluster, cut in the middle, with oxygen molecules removed, corresponding to the temperature range of 2500-6000K.

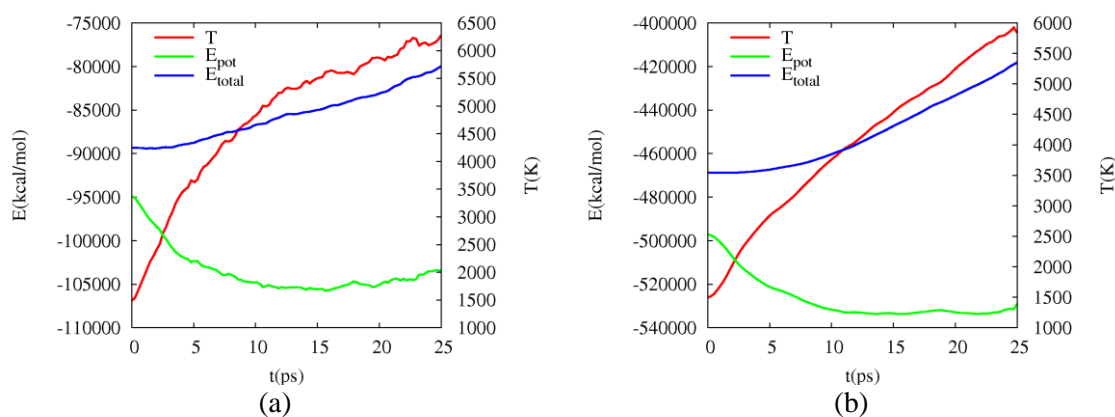


Figure 3-8. Temperature, potential and total energy during the cluster oxidation (a – 256-atom cluster, b – 1372-atom cluster).

### 3.4 Summary

The main goal of the study was exploring of segregation mechanisms in  $\text{Mo}_3\text{Ni}$  cluster annealing process and analysis of the annealed cluster oxidation dynamics/kinetics and products. The comparative study has yielded similar patterns for 256- and 1372-atom face-centered cubic  $\text{Mo}_3\text{Ni}$  clusters. The

annealing cycle has produced a layered structure with a Mo-enriched core and a Ni-enriched outer layer. Our oxidation simulations showed high production of Mo oxides gas phase-species and a low concentration of Ni-oxides in the gas phase. This could be attributed to higher chemical stability of Mo-oxide gas phase species. The observed oxidation stages vs. temperature correlate well with the characteristic temperatures of Mo and Ni and the main gas phase product species ( $\text{MoO}_2$ ,  $\text{MoO}_3$  and  $\text{NiO}$ ).

*The simulations allow for the conclusion that even a relatively small amount of Ni in a Mo base alloy significantly reduces the formation of gas-phase oxidation products due to thermodynamically favorable segregation, thus stabilizing the surface by subsequent oxide formation.*

## 4 Al grain mixing in Fe/Ni matrices and its influence on oxidation

### 4.1 Introduction

A general focus of research related to the issues highlighted in section 1.1 is on the bulk and surface characteristics of  $\text{Al}_x\text{Ni}_y\text{Fe}_{(1-x-y)}$  alloys, relevant to their use as structural materials in the presence of ambient gases ( $\text{O}_2$ ,  $\text{H}_2$ ,  $\text{H}_2\text{O}$  and  $\text{CO}_2$ ) [52, 53]. A specific aim is to computationally predict the critical Al content necessary for  $\text{Al}_2\text{O}_3$  scale formation and to predict oxidation growth kinetics. With this aim it is important to study the stability of different sized Al grains in a Ni or Fe bulk matrix at temperatures above and below the structure melting point, which is the focus of this study.

Numerous numerical studies involving Ni-Al and Fe-Al compounds have been published. These include calculation of Ni-Al alloy properties, like phase stability [54], point defect properties [54], antiphase boundary energies [54], surface energies [54], relaxations [54], elastic constants for  $\text{Ni}_3\text{Al}$  [54], as well as equilibrium lattice constants [10], cohesive energy [10], activation and migration energies for self-diffusion and the vacancy jump processes for NiAl and  $\text{Ni}_3\text{Al}$  [10], using the embedded atom method (EAM) [55] in static (0K) [54], Monte Carlo (MC) [13, 54] or molecular dynamics (MD) [10, 13] calculations. Modified EAM versions have also been used, like the second nearest-neighbor modified EAM (2NN MEAM) [56] for Fe-Al binary alloys, capable of reproducing ordering ( $\text{DO}_3$  or B2) [56], point defect formation [56], stacking fault energy [56], grain boundary segregation [56] and interactions between dislocations and a solute atom [56], as well as structural, elastic and thermodynamic properties [56]. Other approaches have been employed as well, e.g., analysis of atomic ordering mechanism and order-disorder transformation phenomena (673-1273K temperature range) in  $\text{Fe}_3\text{Al}$  type intermetallics by combining the electronic theory of alloys in pseudopotential approximation with MC simulation [57], or semi-empirical n-body non-central potential MD simulations of cluster formation and order

transformations in the process of quick solidification of liquid  $\text{Fe}_{50}\text{Al}_{50}$  [58]. Regarding Al-Ni and Al-Fe diffusion processes specifically, there are multiple related studies published [59-73]. Most of the studies deal with Al-Ni alloy diffusion at temperatures below the melting point. A study on Ni/Al planar interface diffusion at temperature close to melting point using MD and EAM has also been published [74]. However, to the best of our knowledge, no results have been published on Al grain – Fe/Ni matrix mixing processes.

The reported study is based on MD type simulations in combination with the ReaxFF empirical reactive force field [75] with a parameter set developed particularly for elements Fe, Ni, and Al. The motivation for using ReaxFF instead of EAM or other methods available is primarily related to the intended further simulations of Fe/Ni/Al alloy oxidation in the presence of ambient gases and the high quality of its previous performance in simulations on surface segregation in Fe/Ni/Al alloys [76]. We have recently demonstrated that ReaxFF can provide an accurate description for single-metal phases [77] and compared the ReaxFF description for gold to EAM-descriptions for this metal [78], demonstrating that ReaxFF is of similar or superior quality (for diffusion barriers) to existing EAM descriptions. ReaxFF has a considerable higher computational expense than EAM or MEAM description (typically 5-20 times more expensive). The lower computational expense of the embedded atom descriptions may make these methods more appealing for single-metallic or simple bimetallic descriptions, but for connection to gas-phase chemistry and carbide/hydride/oxide/sulfide chemistry [79-82] the high ReaxFF transferability and accuracy provides sufficient compensation for the increased computational expense.

## 4.2 Method

The [83] version of the ReaxFF force field for Al/Ni/Fe/O systems was used in the study.

Prior to the main simulation there were prepared conjugate gradient energy minimized (force tolerance/root mean square of potential energy less than  $.25 \text{ kcal/mol}/\text{\AA}$ ) periodic bulk structures of pure

Fe or Ni with sizes of 2000 (28.4x28.4x28.4 Å) and 2048 (28.16x28.16x28.16 Å) atoms, respectively. Subsequently, 1 and 8 spherical Al grains, yielding approximate grain/matrix atom ratio of 1:3, were defined by redefining the respective bulk subvolume atoms as Al (Table 4-1, Figure 4-1). Since the interatomic distances in pure Al crystals are larger than those of Fe and Ni (Table 4-2), the newly defined grain/matrix structures were energy minimized again (no volume change allowed during the minimization).

The constant system size – pressure – temperature ensemble (NPT), in implementation with the Verlet velocity algorithm for integrating the equations of motion [13] and the Berendsen thermo/barostat [14], has been used in the study. Settings of .25 fs time step, 100 fs temperature and 5000 fs pressure damping constants were used. The atmospheric pressure was set to 0 Pa during the whole simulation. To simulate heating process of the structures in the temperature range of 300 to 3000K, the temperature was changed stepwise by 100K increments after 50 ps equilibration time intervals. Cooling simulations were also done with the structures obtained from 1 Al grain melting simulations over the temperature range of 3000-300K using the same settings.

Oxidation simulations were done for slab structures with single Al grain in constant system size, volume and temperature (NVT) ensemble at 1500K with 3000 oxygen molecules added at density of .09 kg/l. Settings of .1 fs time step and 300 fs temperature damping constant with individually damped atoms were used. For the Ni matrix structure the temperature damping was applied to the slab atoms only.

*Strain energy definition.* The chemical strain energy per atom is defined as the sum of the total potential energy component fractions per atom subtracted by the heat of formation increment, which corresponds to the energy of the respective atom type in its natural state. The potential energy component fractions are defined specifically for each energy component.

### 4.3 Results and discussion

For analysis of results the potential energies and system volumes vs. temperature were plotted (Figure 4-2, Figure 4-3, Figure 4-14, Figure 4-15). These enabled us to detect time instants when critical changes in the structures occur. Also, locally calculated chemical strain energies per atom (Figure 4-4 – Figure 4-7) as well as the radial distribution function (RDF) and its integral form (IRDF) were evaluated (Figure B-1, Figure B-4, Figure 4-7, Figure 4-8). For visualization of strain energy and atom distribution graphical snapshots of the structure cross sections at different time instants were used.

#### 4.3.1 Potential energy, volume and atom distribution during melting

For the 1 grain Fe matrix structure, the volume rise at about 1600K (Figure 4-2b, Figure 4-4a,b) could correspond to melting of Al (Figure B-1a), due to substantial Al-Al RDF peak flattening, and interface mixing (Figure B-1c,d), due to increase in Fe-Al RDF and IRDF values. The potential energy rise and volume drop at about 2500K (Figure 4-2, Figure 4-4c,d) could correspond to complete grain/matrix atom mixing (Figure B-1c,d), due to substantial increase in Fe-Al RDF and IRDF values, and structure melting (Figure B-1a,b), due to notable Al-Al and Fe-Fe RDF peak flattening. Similar reasoning applies to the conclusions that follow for the other Fe and Ni matrix structures.

For the 8 grain Fe matrix structure, we assign the slight potential energy and volume drop after reaching 2300K (Figure 4-2, Figure 4-5a,b) to substantial interface mixing (Figure B-2c,d) and melting of Al (Figure B-2a). A sharp rise of potential energy and volume at about 2700K (Figure 4-2, Figure 4-5b,c) is due to complete grain/matrix atom mixing (Figure B-2c,d) and structure melting (Figure B-2a,b).

For the 1 grain Ni matrix structure, the potential energy and volume drop at about 1800K (Figure 4-3, Figure 4-6a,b) could result from partial ordered mixing of grain/matrix atoms in the grain region (Figure B-3c,d), not observed for Fe matrix structures, and structure melting (Figure B-3a,b), particularly

Al. The partial ordered mixing is attributed to a large increase in the first peak and small change between the first and second peaks of the Ni-Al RDF, and the corresponding increase and flatness of the first coordination shell segment of the Ni-Al IRDF. The potential energy and volume rise at about 2400K (Figure 4-3, Figure 4-6b,c) could result from complete mixing of grain/matrix atoms (Figure B-3c,d) and dynamic continuation of structure melting (Figure B-3a,b).

For the 8 grain Ni matrix structure, the discontinuation of the increase of volume and potential energy at about 1000K (Figure 4-3, Figure 4-7a,b) could be related to the initiation of grain/matrix atom mixing (Figure B-4c,d) and structure melting (Figure B-4a,b). Further drop in volume and potential energy at about 2000K (Figure 4-3, Figure 4-7c,d) could be related to more dynamic mixing (Figure B-4c,d) and melting (Figure B-4a,b) processes. Subsequent sharp rise in volume and potential energy at about 2300K (Figure 4-3, Figure 4-7d,e) could be related to complete mixing of grain/matrix atoms (Figure B-4c,d) and structure melting continuation (Figure B-4a,b).

Summarizing the above observations it could be concluded that

- The Al grains start melting earlier than matrix atoms in accordance with the lower melting point of Al (Table 4-2).
- Sudden changes of volume and potential energy accompany initiation of abrupt changes in structure melting and mixing processes, which most often coincide.
- In the Fe matrix grain/matrix melting and mixing occurs earlier for larger grains, supposedly due to the latter having a sharp expansion prior to the matrix melting start, which is not observed in any of our other simulations and could be related to Fe-Fe crystal bond lengths being smaller than Ni-Ni bond lengths, both being smaller than those of Al-Al (Table 4-2), thus creating a larger volume mismatch in the Fe/Al case, compared to the Ni/Al case. Likewise, the sharp expansion could be related to Al atoms, which are most stable in face-centered cubic (FCC) configuration, in Fe matrix initially being in a body-centered cubic (BCC) configuration instead of FCC configuration in the Ni matrix case. Both effects are related to the applied grain definition (section 'Method').

- In the Ni matrix melting and mixing occurs earlier for smaller grains, supposedly due to the latter having a larger interface area.
- Melting is generally complete for the Ni matrix at lower temperatures than for the Fe matrix in accordance with the lower melting point of Ni (Table 4-2).
- Differences in melting/mixing temperature (Table 4-3), energy/volume change patterns and partially mixing favorable grain sizes for Fe and Ni matrices could be attributed to differences in mixing/formation energies, which are about -19kJ/mol [84] for Fe<sub>3</sub>Al and about -41kJ/mol [85] for Ni<sub>3</sub>Al at 0K. The observations are in accord with the strain energy distribution, described below.
- Structure melting processes occur primarily at temperatures that are higher than the known melting points of the separate components (Table 4-2), which could be partially attributed to the heating rate.

From the system snapshots (Figure 4-4 – Figure 4-7) it can be concluded that initial volume diffusion primarily occurs when the matrix atoms migrate into the molten Al grain with comparatively less Al atoms migrating into the matrix, which conforms with the results published in [74].

#### 4.3.2 Strain energy distribution during melting

The relative stability of atoms can be estimated based on their chemical strain energy values, as defined above. The atoms with lower strain energy are considered to be more stable. However, the strain energy definition does not allow for absolute value comparison between different atom types.

From the chemical strain energy distribution for matrix atoms (Figure 4-4 – Figure 4-7), ranging approximately between 0 and 40-60 kcal/mol for both matrices, it can be observed that the matrix atoms are less stable, compared to bulk, at grain/matrix interface. The chemical strain energy of Al atoms ranges approximately between -70 and 0 kcal/mol for Ni matrix and between -30 and 10 kcal/mol for Fe matrix. This allows for the conclusion that Al atoms are comparatively more stable in Ni matrix, which likewise could be attributed to the differences in mixing/formation energies. In distinction to matrix atoms (Figure

4-4 – Figure 4-7), the Al atoms appear to be more stable, compared to bulk, at grain/matrix interface. For all atom types the stability differences increase as the temperature increases.

### 4.3.3 Stress distribution during melting

Supplemental hydrostatic stress distribution calculations were performed during the melting simulations. For that purpose the individual atom stress components were calculated using the LAMMPS/ReaxFF implementation, which calculates the per-atom stress, defined as the negative of the per-atom pressure tensor, in units of stress·volume. The compatibility of the LAMMPS and ADF ReaxFF implementations was verified by comparing the respective potential energy and volume vs. time plots. The stress distribution plots (Figure 4-8 – Figure 4-11) indicate that distinct compressive or tensile stress regions are present only prior to the initiation of mixing and melting processes. Furthermore, the Al atoms appear to be in compression, whereas the matrix atoms are in tension, which is attributed to the differences in bond lengths, as discussed in section ‘Potential energy, volume and atom distribution during melting’, and partially related to the strain energy differences. Due to the increasingly randomized stress distribution after melting initiation, the mean and standard deviation values for each atom type were calculated from the atomic stresses at each iteration. By comparing the potential energy and mean stress changes vs. temperature and time, respectively, temperature and time being considered equivalent due to the linear heating rate (Figure 4-2, Figure 4-3, Figure 4-12, Figure 4-13), it was concluded that the mean stress changes abruptly upon discontinuous volume change, but not upon discontinuous potential energy changes in melting/mixing processes which do not involve sharp volume change. During the rest of mixing and melting processes the mean stresses for matrix atoms increase gradually, implying higher tension due to heating, whereas for the Al atoms the mean stress values approach zero, which could be considered as approaching tensile deformation state, compared to the initial state of compression.

Likewise, it can be observed that initially the Al/matrix atom stress ratio is greater than 1, but after melting and mixing it becomes much smaller than 1. That can be related to the NPT ensemble setting of zero total pressure (hydrostatic stress), which does include the kinetic energy contribution; the Al/matrix stoichiometric ratio of 1:3, which requires that the mean Al/matrix hydrostatic stress ratio should be 3:1; differences in strain energy stability, which intensify at higher temperatures, and comparatively small kinetic energy contribution at low temperatures. In distinction to the mean stress values, the stress dispersion/scattering, characterized by the standard deviation of stress for all atoms, increases at constant rate (Figure B-5, Figure B-6), except for discontinuous changes at moments of abrupt volume or potential energy change (section ‘Potential energy, volume and atom distribution during melting’), until an asymptotic value is approached. This could be attributed to the increase in kinetic energy in combination with the phase change. The large final standard deviation values suggest that, upon solidification, residual stresses larger than the initial stresses might occur, with matrix atoms being primarily in tension.

#### **4.3.4 Solidification analysis**

The molten Al/Ni and Al/Fe alloy simulations (Figure 4-14, Figure 4-15) indicated that transitions from liquid to solid state, characterized by discontinuous drop in potential energy and volume, occurred for the Fe alloy at about 1200K and 1400K for Ni, which is between the melting points of Al and Fe/Ni, respectively. The difference of order of 1000K between the melting and solidification temperatures of both alloys could be explained by both superheating and undercooling effects due to the applied high heating and cooling rates, respectively (stepwise temperature increments/decrements of 100K with 50 ps equilibration time intervals, corresponding to uniform heating/cooling rate of  $2 \times 10^{12}$  K/s). Furthermore, the Fe alloy indicates a single-crystalline structure (Figure B-7, Figure 4-16), due to close to zero values between the first and second peaks of all (Fe-Fe, Al-Al, Fe-Al) RDFs and the corresponding

flat segment for the first coordination sphere in the Fe-Al IRDF, whereas the Ni alloy has a polycrystalline/fine-grained structure (Figure B-8, Figure 4-17), due to less distinct crystalline structure patterns in all (Ni-Ni, Al-Al, Ni-Al) RDFs, particularly Al-Al, and the Ni-Al IRDF. It is known that for Ni-Al alloys the degree of order, composition of the solidified structure and transition to amorphous vs. crystalline state are dependent on cooling rate as well as the liquid alloy composition. For the Ni alloy in particular, the cooling rate ( $2 \times 10^{12}$  K/s), that was used in the simulation, corresponds to the critical range of rates for crystalline structures [86], whereas the specific solidification temperature corresponds to the dominance of chemically disordered face-centered cubic (FCC) phase [87]. However, the existence of the chemically disordered Al/Fe alloy at temperature below 1173K and 813K is in conflict with the experimentally observed transition to the chemically ordered phases of B2 and  $DO_3$  [88], respectively, which could be attributed to the effect of high cooling rate. Yet both structures yield energetically more stable, i.e., having a lower potential energy, final configurations compared to the initial ideal-crystalline structures (Figure 4-14a, Figure 4-15a), which conforms with the negative formation energy for both Ni-Al and Fe-Al alloys [84, 85], the approximate ratio of total heating/cooling potential energy change  $dE_{\text{pot}}(\text{Ni-Al})/dE_{\text{pot}}(\text{Fe-Al}) \approx 2.4$  – being close to the ratio of formation energies of the respective alloys – 2.2.

#### 4.3.5 Oxidation simulation results

We performed a series of MD-simulations on the Fe/Ni matrix/1 Al grain systems, defined in section ‘Method’, in order to study the influence of grain/matrix mixing on oxidation kinetics.

The Fe matrix simulations (Figure 4-18) indicate that oxygen preferably reacts with Al, which melts before active mixing occurs. This accounts for the observed oxygen diffusion inwards the slab. At the same time the Fe matrix atoms remain primarily in a crystalline state and oxidize comparatively

slowly. The final oxidation states for Fe and Al are 1.7 and 3.0, resp., which suggests that oxidation is complete for Al, whereas Fe is underoxidized, according to assumed stoichiometry of  $\text{Al}_2\text{O}_3$  and  $\text{FeO}$ .

The Ni matrix simulations (Figure 4-19) reveal that initially oxygen reacts with unmixed Ni and Al atoms in the outer surface layers, whereas inside the slab rapid matrix/grain mixing occurs without notable oxygen diffusion taking place. This suggests that Ni-Al alloy might be less reactive with oxygen than pure Ni or Al structures. It can also be observed that mixing is not complete, resulting in formation of rapidly oxidizing Al subsurface layers. In the final snapshot it can be observed that Al from the alloy layer eventually has dissolved into the adjacent Al layers and subsequently a layer of Ni oxide in the middle of the slab has formed. Again, the oxidation is complete for Al (oxidation state 3.1), whereas Ni is underoxidized (oxidation state 1.7), according to assumed stoichiometry of  $\text{Al}_2\text{O}_3$  and  $\text{NiO}$ . This allows for the conclusion that in the considered structures the oxidation rates of Fe and Ni are lower, compared to Al, the rate of Fe being the lowest.

The results of these small scale, preliminary oxidation simulations indicate that the dynamics of matrix/grain mixing processes has a pronounced influence on the kinetics of oxidation reactions; we aim to report larger-scale MD-studies on this topic in the future.

Table 4-1. Atomic percentage of Al in Fe/Ni-Al matrix/grain structures.

at. % Al		
matrix	1 grain	8 grains
Fe	25.1	28.0
Ni	23.6	26.6

Table 4-2. Characteristic temperatures and bond distances of Ni, Fe, Al.

	m.p. (K) [89, 90]	b.p. (K) [89, 90]	bond dist. (Å)
Ni	1726	3157	2.489 [91]
Fe	1811	3134	2.459 [92]
Al	933	2792	2.863 [93]

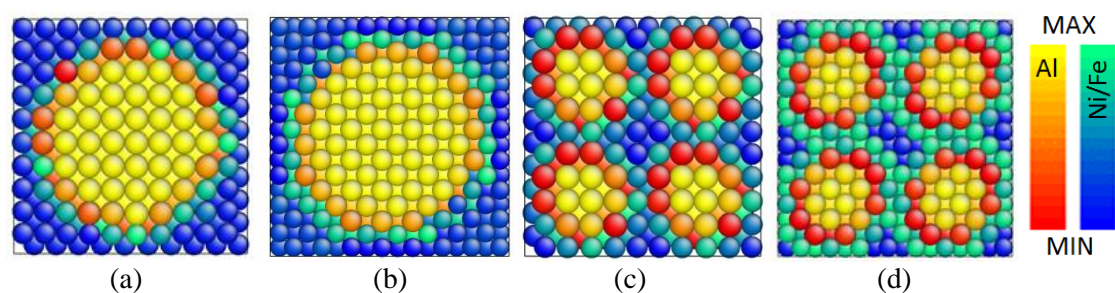


Figure	Fe		Al	
	min	max	min	max
a	-0.2812	3.9289	-23.0818	-4.4694
c	-0.3282	3.0271	-18.6820	-4.7794
	Ni		Al	
	min	max	min	max
b	0.1385	4.3081	-45.0379	-2.4486
d	0.7103	4.2367	-22.1244	-5.3649

Figure 4-1. Strain energy [kcal/mol] distribution for Fe (1 grain (a), 8 grains (c), 28.4x28.4x28.4 Å) and Ni (1 grain (b), 8 grains (d), 28.2x28.2x28.2 Å) matrix structures in the initial configuration at 300K.

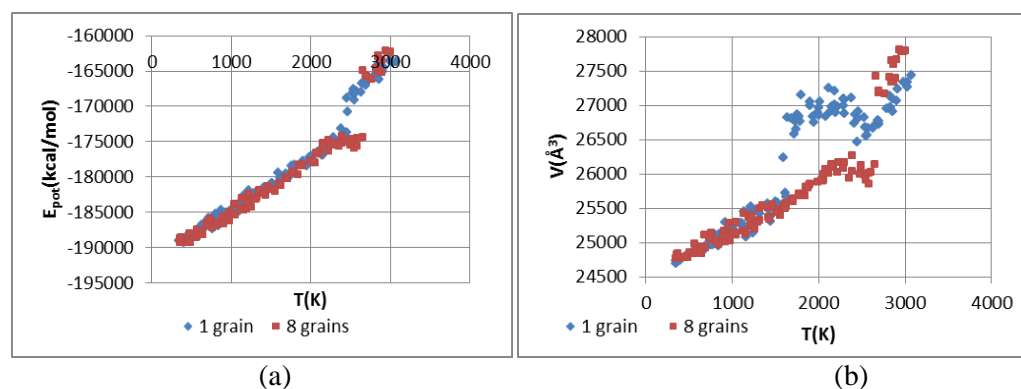


Figure 4-2. Potential energy (a) and volume (b) vs. temperature for Fe matrix structures during heating.

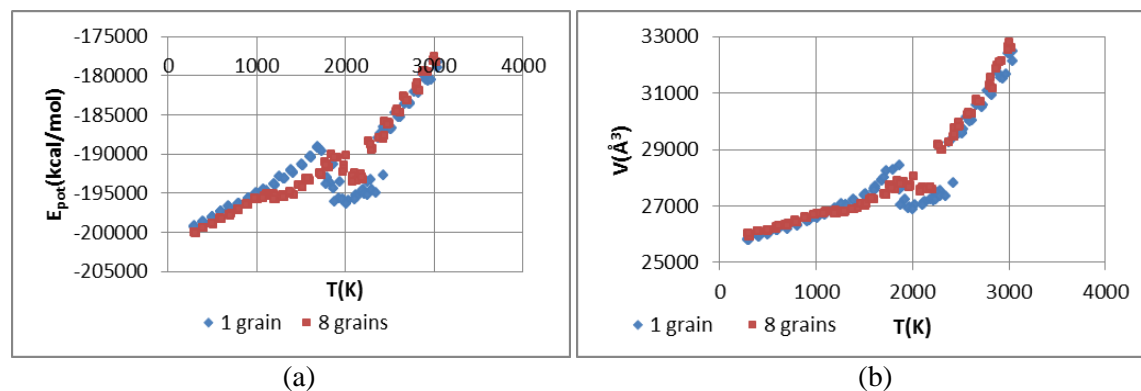


Figure 4-3. Potential energy (a) and volume (b) vs. temperature for Ni matrix structures during heating.

Table 4-3. Estimates of melting points (K).

matrix	1 grain	8 grains
Fe	2500	2700
Ni	2400	2300

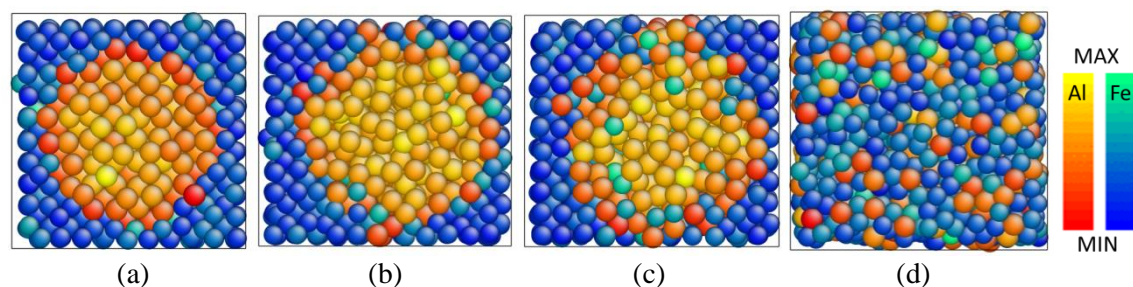


Figure	T(K)	Fe		Al	
		min	max	min	max
a	1437	-2.8121	22.3458	-23.0585	9.886
b	1781	-3.1055	33.7568	-27.6153	11.9302
c	2190	-2.0714	39.3965	-28.2012	12.2961
d	2560	-0.3379	42.5658	-35.411	6.8713

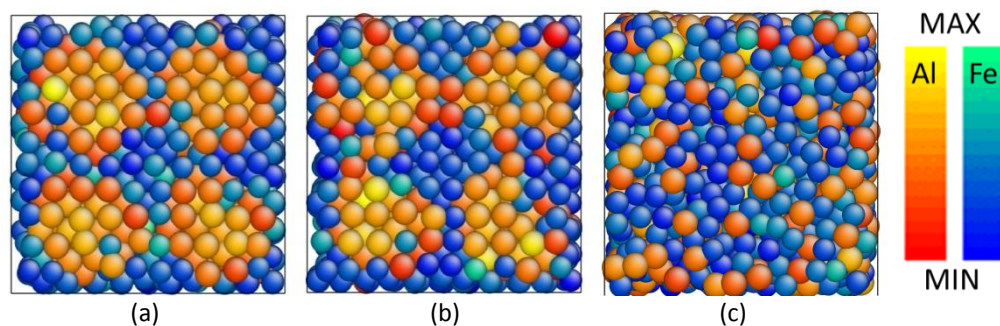
Figure 4-4. Strain energy [kcal/mol] distribution for 1 Al grain in Fe matrix structure ( $28.4 \times 28.4 \times 28.4 \text{ \AA}$ ) at different temperatures during heating.

Figure	T(K)	Fe		Al	
		min	max	min	max
a	2218	-3.1305	35.0254	-30.6674	11.6543
b	2359	-1.3442	38.7948	-28.9295	5.9496
c	2827	2.6176	49.2919	-35.2037	12.9927

Figure 4-5. Strain energy [kcal/mol] distribution for 8 Al grains in Fe matrix structure ( $28.4 \times 28.4 \times 28.4 \text{ \AA}$ ) at different temperatures during heating.

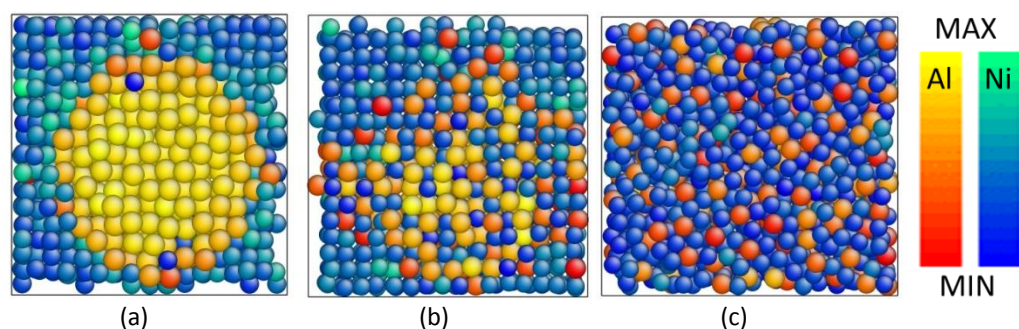


Figure	T(K)	Ni		Al	
		min	max	min	max
a	1599	-4.0874	18.458	-65.1115	4.2927
b	2006	-6.3304	24.9469	-68.2345	-5.4786
c	2371	2.3634	49.3437	-70.757	-9.2574

Figure 4-6. Strain energy [kcal/mol] distribution for 1 Al grain in Ni matrix structure ( $28.2 \times 28.2 \times 28.2 \text{ \AA}$ ) at different temperatures during heating.

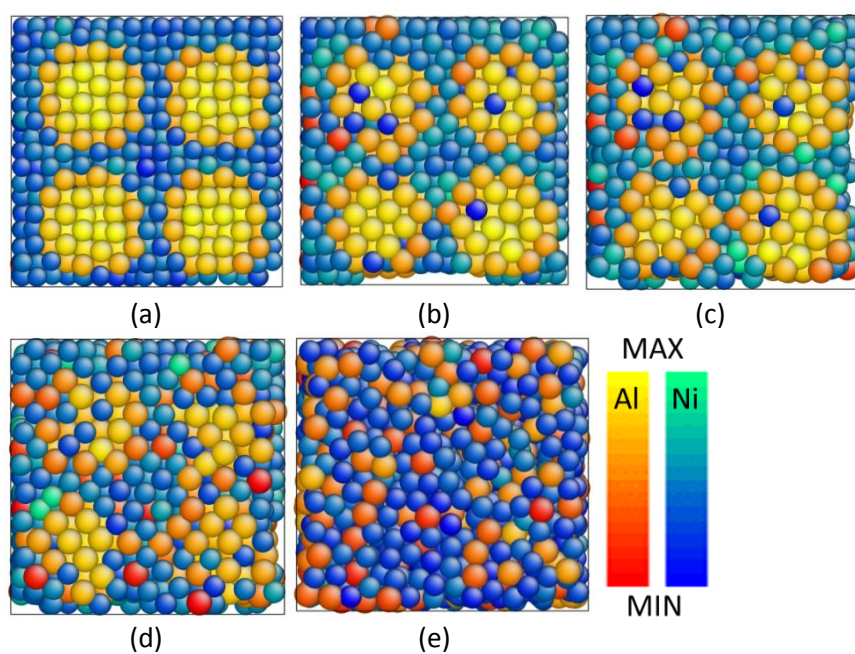


Figure	T(K)	Ni		Al	
		min	max	min	max
a	977	-5.2219	21.0283	-72.3846	-2.5232
b	1378	-9.715	21.4779	-73.1757	1.9223
c	1783	-9.2235	23.0217	-69.7747	5.4961
d	2076	-8.9252	26.46	-72.0443	4.6963
e	2436	3.4853	41.9935	-71.6098	-6.648

Figure 4-7. Strain energy [kcal/mol] distribution for 8 Al grains in Ni matrix structure ( $28.2 \times 28.2 \times 28.2 \text{ \AA}$ ) at different temperatures during heating.

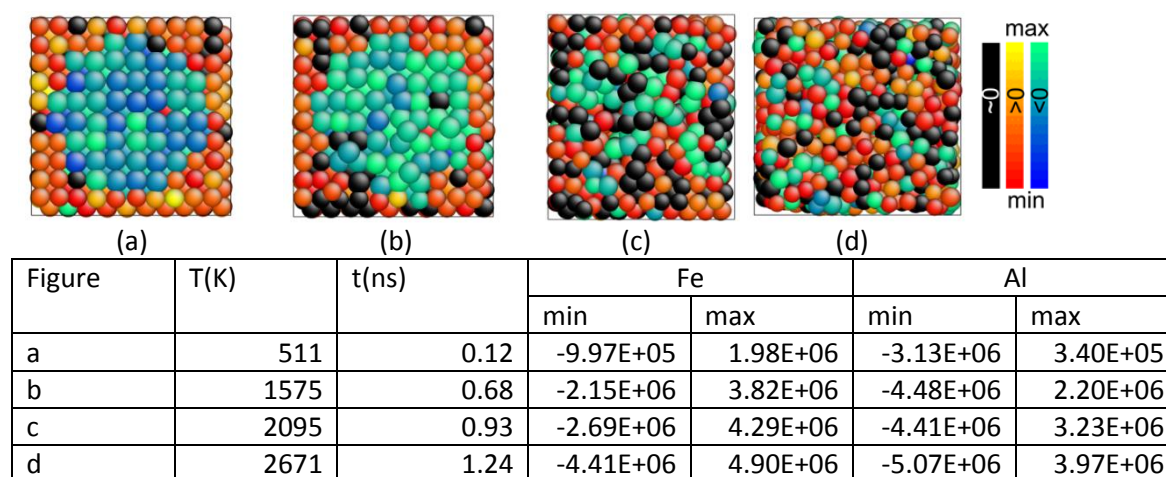


Figure 4-8. Atomic hydrostatic stress [ $\text{\AA}^3 \cdot \text{atm}$ ] distribution for 1 Al grain in Fe matrix structure ( $28.4 \times 28.4 \times 28.4 \text{ \AA}$ ) at different temperatures during heating.

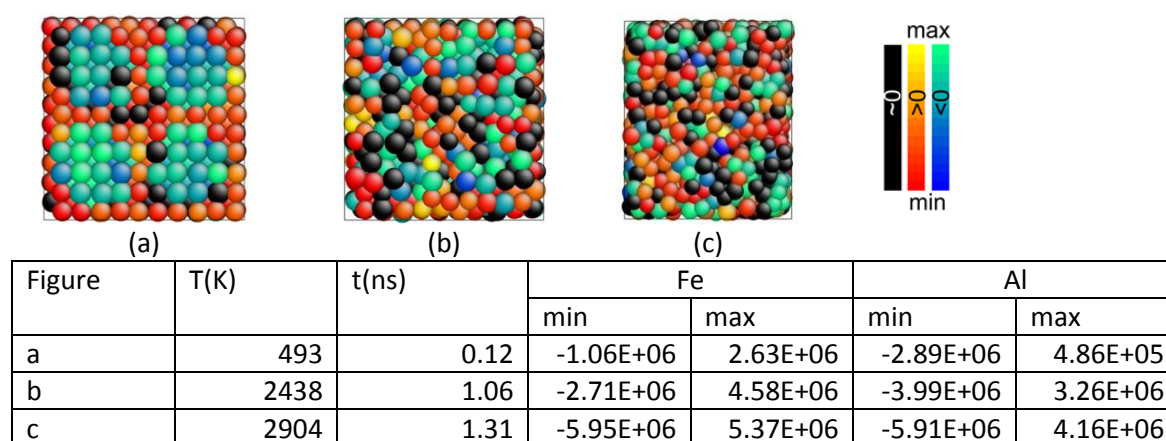


Figure 4-9. Atomic hydrostatic stress [ $\text{\AA}^3 \cdot \text{atm}$ ] distribution for 8 Al grains in Fe matrix structure ( $28.4 \times 28.4 \times 28.4 \text{ \AA}$ ) at different temperatures during heating.

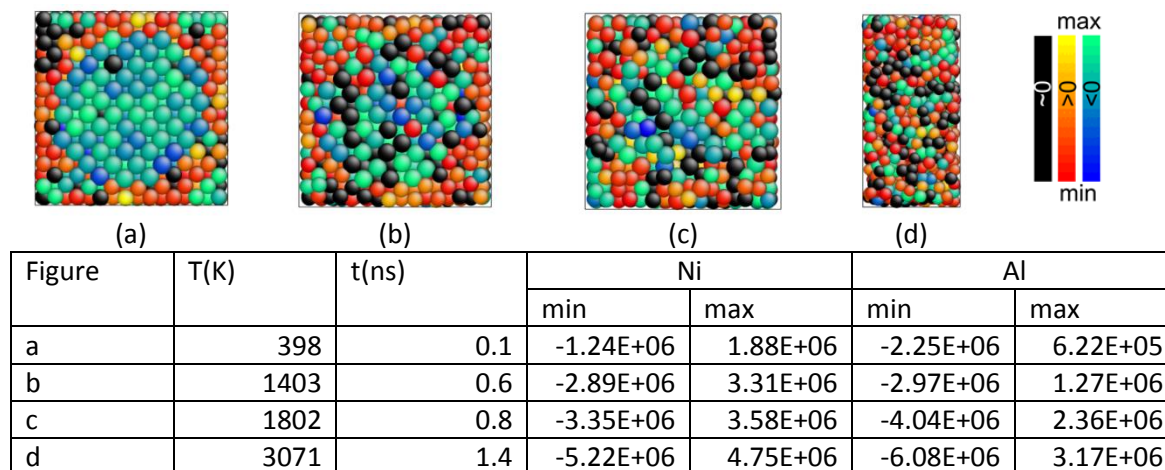


Figure 4-10. Atomic hydrostatic stress [ $\text{\AA}^3\text{-atm}$ ] distribution for 1 Al grain in Ni matrix structure ( $28.2 \times 28.2 \times 28.2 \text{ \AA}$ ) at different temperatures during heating.

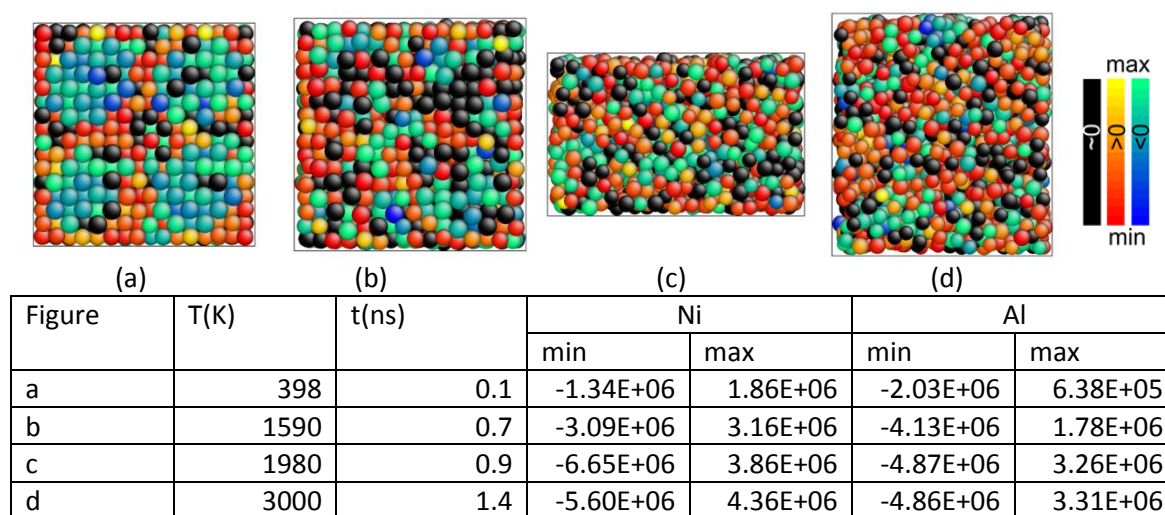


Figure 4-11. Atomic hydrostatic stress [ $\text{\AA}^3\text{-atm}$ ] distribution for 8 Al grains in Ni matrix structure ( $28.2 \times 28.2 \times 28.2 \text{ \AA}$ ) at different temperatures during heating.

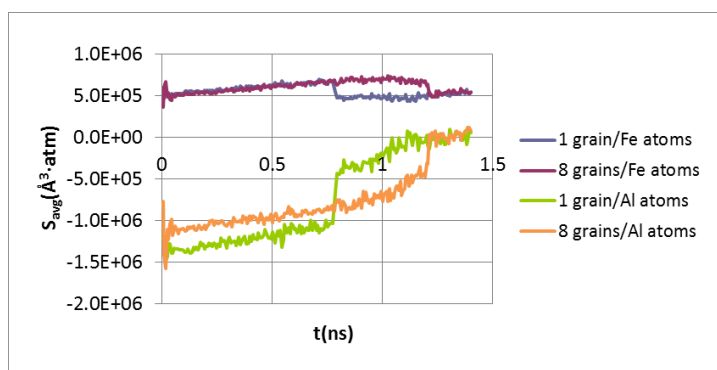


Figure 4-12. Mean atomic hydrostatic stress vs. time for 1/8 Al grain Fe matrix structures during heating.

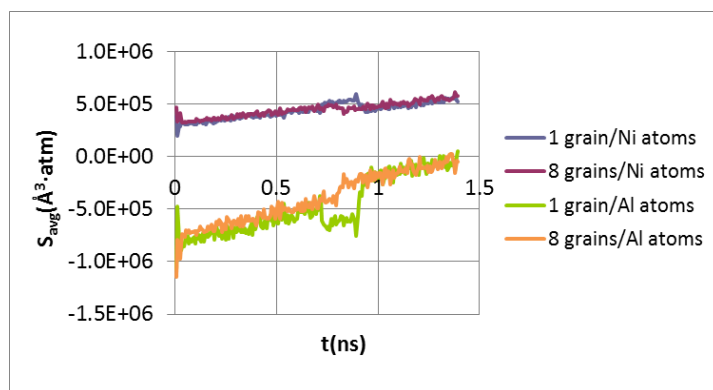


Figure 4-13. Mean atomic hydrostatic stress vs. time for 1/8 Al grain Ni matrix structures during heating.

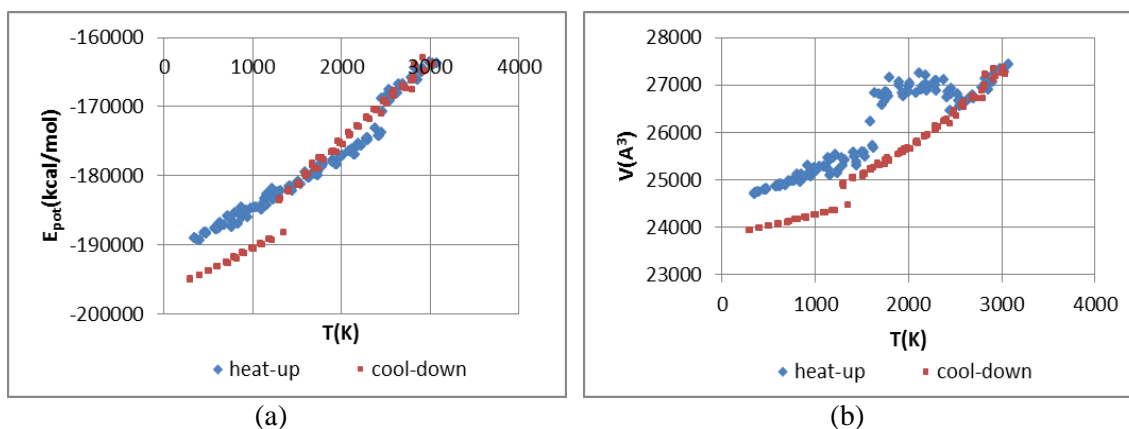


Figure 4-14. Potential energy (a) and volume (b) vs. temperature for 1 Al grain Fe matrix structure during heating and cooling.

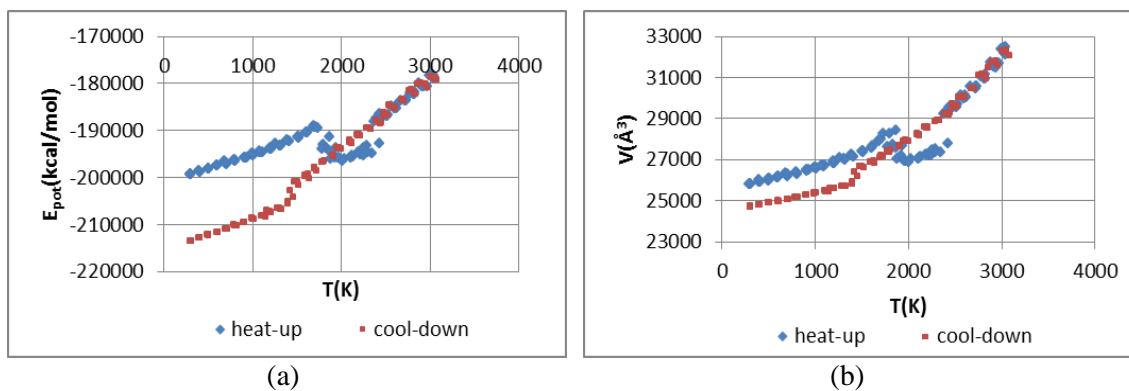


Figure 4-15. Potential energy (a) and volume (b) vs. temperature for 1 Al grain Ni matrix structure during heating and cooling.



Figure 4-16. Molten Fe matrix ( $28.4 \times 28.4 \times 28.4 \text{ \AA}$ ) structure configuration snapshots before (1701K (a)) and after (1325K (b)) solidification (Fe – orange, Al – grey).

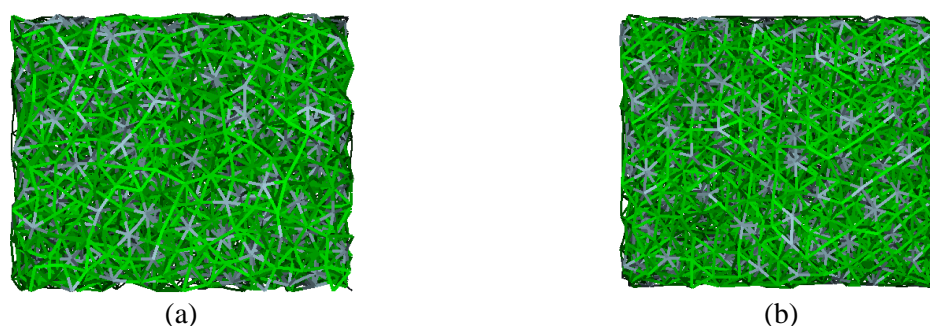


Figure 4-17. Molten Ni matrix ( $28.16 \times 28.16 \times 28.16 \text{ \AA}$ ) structure configuration snapshots before (1515K (a)) and after (1084K (b)) solidification (Ni – green, Al - grey).

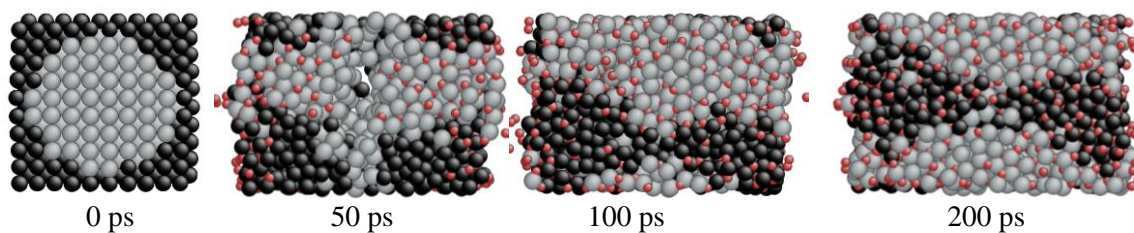


Figure 4-18. Fe matrix/Al grain structure ( $28.4 \times 28.4 \times 28.4 \text{ \AA}$ ) oxidation simulation snapshots (Fe – black, Al – grey, O – red).

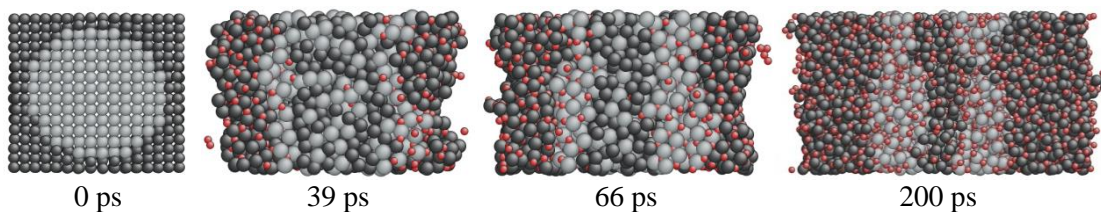


Figure 4-19. Ni matrix/Al grain structure ( $28.2 \times 28.2 \times 28.2 \text{ \AA}$ ) oxidation simulation snapshots (Ni – black, Al – grey, O – red).

#### 4.4 Conclusion

To study the stability of different sized Al grains in Ni/Fe bulk matrices at temperatures above and below the structure melting point, MD simulations of respective structures (grain/matrix atom ratio ~1:3) have been carried out in NPT ensemble conditions for temperatures being stepwise ramped over the range of 300-3000K. The results show that, in accord with published data, Al-Ni alloy is energetically more stable than Al-Fe alloy. This is confirmed by lower chemical strain energies for Al and Ni in mixed state and completion of mixing at lower temperature than for Fe matrix. Supposedly due to Fe-Fe crystal bond lengths being smaller than Al-Al bond lengths, larger Al grains appear to be favorable for mixing with Fe matrix. However, for Ni matrix smaller Al grains appear to be favorable for mixing, which can be explained by larger interface/mixing area, differences in the heats of formation and Ni-Ni crystal bond lengths being larger than Fe-Fe bond lengths.

Supplemental hydrostatic stress distribution calculations during the melting simulations were done to check for any correlation between stresses and the chemical strain energy distribution, as well as changes of stress distribution at moments of dynamic melting and mixing. The calculations indicate that a relation between strain energy stability and stresses for matrix and grain atoms exists both before and after structure melting. The stress value scattering, characterized by the standard deviation of stresses, was found to be increasing with temperature. The obtained stress distribution could serve as an estimate of the residual stress levels, which would be obtained upon amorphous/polycrystalline solidification.

Cooling simulations over the temperature range of 3000-300K were also done. These revealed that for the considered cooling rate Fe alloy solidifies at a lower temperature than Ni alloy. Moreover, the Fe alloy solidifies to a crystalline structure, whereas the Ni alloy solidifies to a polycrystalline/fine-grained structure. The ratio of total heating/cooling potential energy change is found to be close to the ratio of formation energies of the respective Fe and Ni alloys.

The results of preliminary oxidation simulations of slab structures with single grain allow concluding that the dynamics of matrix/grain mixing processes have a pronounced influence on the oxidation reactions, Al and Ni atoms in unmixed state being the most active reactants.

To summarize:

- Al-Ni alloy is energetically more stable than Al-Fe alloy.
- Obtained stress distribution could serve as an estimate of the residual stress levels, which would be obtained upon amorphous/polycrystalline solidification.
- For the given quenching rate the Fe alloy solidifies to a crystalline structure, whereas the Ni alloy solidifies to a polycrystalline/fine-grained structure.
- Dynamics of matrix/grain mixing processes have a pronounced influence on the oxidation reactions, Al and Ni atoms in unmixed state being the most active reactants.

## 5 Stress corrosion failure and related studies

### 5.1 Introduction

Among the environmentally assisted cracking (EAC) structural material failures a few main types can be distinguished [18]. These include stress corrosion cracking (SCC), which occurs through a material's interaction in stressed state with chemically active fluid environment species and hydrogen caused embrittlement (HE) due to bulk dissolved atomic hydrogen, which tends to migrate to high stress regions. Both phenomena have been explored extensively both experimentally and computationally for a wide range of materials. A comprehensive review of known and suggested SCC and HE mechanisms, as well as outstanding issues, can be found in [94]. In particular, a review of H diffusion and dislocation channeling related intergranular SCC and irradiation assisted SCC studies is published in [95]. Yet, to the best of our knowledge, no all-atomistic scale MD simulation studies of these phenomena at lower mesoscale spatial dimensions have been published so far.

Due to the use of periodic boundary conditions and the requirement for constant pressure fluid-solid interface, thin film structures were considered. Since it was considered that fundamental understanding of the mechanical failure mechanisms is essential for interpreting results from the interface systems simulations, complementary studies were focused on fatigue behavior and strain rate effects.

The ReaxFF force field versions used in the simulations of Al/O/H systems have been based on earlier published versions of Al/O [96, 97], Al/H [98], O/H [99] and Al/O/H [82] force fields. For Ni/O/H systems the [100] force field version was used.

### 5.1.1 Stress corrosion cracking in alloys

Both the dislocation nucleation inhibition by a single O impurity atom at a crack tip of a single metal in static calculations [101] and stress enhanced metal segregation and H/O inward diffusion in alloy type structures at elevated temperature [102] have been suggested as possible early stage EAC mechanisms. A more general discussion of solid materials brittleness and crack healing probability, based on a comparison of the electronic bonding structure from DFT calculations on Al and Al<sub>2</sub>O<sub>3</sub>, can be found in [103]. Moreover, analytical models, based on the combination of crack tip mechanics and oxidation kinetics in alloys, have been developed [104-106]. The models refer to consecutive stage mechanisms of open surface dissolution, oxidized film formation and thickening, solid state oxidation during steady state passivation and strain facilitated rupture, which produces new open surfaces. The significance of alloy composition has been studied experimentally, e.g., for a Ni-Cr alloy [107], which indicates simultaneous processes of alloy component diffusion and oxygen penetration ahead of crack tips and along grain boundaries, or for a Ni base superalloy [108], which indicates that dense grain boundary precipitates may reduce intergranular stress corrosion cracking (IGSCC) due to crack blunting effects. Furthermore, the room temperature reactivity properties as functions of electric field [100] or electrochemical potential [109] have been studied.

### 5.1.2 Hydrogen embrittlement in metals

Detailed atomistic failure mechanisms involving increased dislocation emission barriers by H atoms on crack surface [101, 110], reduced dislocation emission barriers by H atoms on the slip plane [110], H migration to crack tip [110, 111], as well as combined atomistic/kinetic models [111, 112] have been presented. In the latter, atomistic/kinetic model, studies a kinetic analysis is used to calculate the size of a H-rich region formed at the crack tip. By combining the kinetic analysis with the

deformation/fracture analysis a ductile-to-brittle transition mechanism map is proposed, which is validated by experimental results. Related HE mechanisms include hydrogen-enhanced decohesion [113], as well as adsorption-induced dislocation emission [114] and hydrogen-enhanced localized plasticity [115]. Likewise, related thermodynamic Al hydride properties [116-120], including Al-vacancy binding and other H trapping states, have been studied. Accordingly, for H facilitated fracture, void coalescence mechanisms, as discussed, e.g., for an Al alloy [121], may be applicable [114, 120, 122].

For the current HE study (section 5.9) fcc-Al was used as a model material due to its low H solubility [119] and, hence, a high expectation for chemical activity in proximity of crack surfaces [110].

### **5.1.3 Stress corrosion cracking and fatigue in $\text{Al}_2\text{O}_3$ based ceramics**

The cyclic and static fatigue behavior of polycrystalline  $\text{Al}_2\text{O}_3$  or  $\text{Al}_2\text{O}_3$  based ceramics, used as protective oxide surface layer materials in structural applications [4, 34, 123-125], has been studied experimentally and analytically, considering strength and crack propagation rate dependence on grain boundary content and air vs. water [126-128] or inert vs. moist air [129] environment, as well as grain bridging shielding degradation dependence on grain size and loading level [130-132]. A stress corrosion assisted grain size dependent [36] static fatigue mechanism, involving a microcrack growth, coalescence and fracture, and an associated analytical model have been proposed for multigrain vitreous bonded alumina [35]. The interface strengthening effects of  $\text{Al}_2\text{O}_3$  coating application, along with splat cracking and void coalescence development mechanisms, have also been studied, e.g., for steel substrates [133]. However, to the best of our knowledge, no atomistic fatigue studies beyond unit cell  $\alpha\text{-Al}_2\text{O}_3$  calculations [134] have been done. Yet, according to an experimental study [135], transgranular fracture, which may be dominant for unstable fracture [128, 135], constitutes ~30% of fatigue fracture surfaces. Moreover, since experimental fatigue studies may not identify incipient atomistic failure mechanisms of cyclic loading in single crystals, the current simulation studies (sections 5.3-5.7) are intended as a contribution

to the purpose. Water was chosen as a generalized EAC environment. In order to form a link with general characteristics of single- and polycrystalline  $\text{Al}_2\text{O}_3$  cracking, a brief overview of known phenomena will be presented in the remainder of this section.

The experimental data on polycrystalline, in particular nanocrystalline,  $\text{Al}_2\text{O}_3$  crack propagation indicate that cracks primarily propagate along grain boundaries [132, 136]. In contrast, the brittleness of bulk crystalline  $\text{Al}_2\text{O}_3$  has been explored in context of density distribution and extent of surface relaxation during crack opening in a DFT study [103]. Furthermore, the brittle vs. ductile deformation behavior of the material beside temperature can be influenced by deformation rate, grain size and the structure of the grain boundaries. In particular, the increase of deformation rate corresponds to increase in brittle to ductile transition temperature (BDTT) [21], whereas the presence of other elements, like Mg, may result in formation of amorphous grain boundary phases that have lower melting temperatures than pure Al oxide. As a result, a transition from ductile to brittle at high temperatures may occur [137]. The grain size is found to be proportional to the slope of stress intensity vs. crack length (related to *R*-curve behavior, a.k.a. *J* vs.  $\Delta a$  curve, for elastic materials  $J = -1/t \, dU/da$ , where *U* is the energy necessary for crack propagation, *t* – sample thickness, *a* – the crack depth), which implies that the fracture toughness of the material decreases with decreasing grain size [21, 138]. This particular material behavior is explained by the corresponding reduction in crack path length surrounding the bridging grains (grains in compression due to mismatch between elastic and thermal properties of grains) and the mean value of residual stresses [138]. Lower residual stresses imply reduction of friction forces upon grain pullout from the embedding matrix. The residual stress reduction, in turn, is attributed to stress relaxation due to grain boundary diffusion, which is higher for smaller grains [139]. Likewise, the *R*-curve behavior may be significantly reduced by addition of second phase particles, like  $\text{ZrO}_2$  or SiC, due to a resultant reduction in grain size [138].

For brittle transgranular fractures at room temperature, fracture morphologies of even fracture surfaces, surfaces with step-terraces and surfaces mainly composed by curved fracture have been

identified [20]. Likewise, a single sapphire crystal plates fatigue mechanism has been studied phenomenologically, indicating loading orientation dependent spatial perturbations along low energy cleavage planes [140]. Beside transgranular fractures that occur along the primary crack line along with intergranular fractures, the crack-interface grain bridging [141], which may appear between overlapping cracks, separated by several grain diameters, has been identified as a mechanism for explaining the *R*-curve behavior of the material under the assumption that no phase transformation takes place. This behavior is found to correlate with the findings of an acoustic emission study which attributes the propagation of the primary crack at room temperature to two crack resistance mechanisms which consist in coalescence of microcracks behind the crack tip and energy dissipation in the flanks of the crack [142].

According to [143], intermetallic compounds can be forced to undergo a crystalline to amorphous (CA) transformation when the stresses at a crack tip elevate the free energy of the compound above that of the amorphous state. Analogous behavior due to overall pressure has been reported also for TiO<sub>2</sub> [144] and Y<sub>2</sub>O<sub>3</sub> [145], as well is for hypervelocity impact deformations [29, 146]. Specifically, amorphization in  $\alpha$ -alumina under hypervelocity impact has been observed in large-scale MD simulations [29], where the amorphous regions are found to act as a source of dislocations. Instead, at the interface between amorphous domains and crystalline phases domains cracks are reported to initiate [29]. Likewise, amorphization has been observed in mullite (3Al<sub>2</sub>O<sub>3</sub>-2SiO<sub>2</sub>) samples shocked above the phase-transition pressure [146].

Alternatively, CA transition in elastic loading can be a sudden collapse of the lattice when the crystal is brought to become mechanically unstable, e.g., due to the loss of shear rigidity [143, 147]. The latter, according to [147], is valid for homogeneous processes of mechanical melting, which can be observed at extremely high deformation rates, or upper limit of superheating. Another deformation mechanism by amorphization induced plasticity has been introduced in [148]. According to this mechanism, nanoscale amorphization (NA) serves as a special plastic shear deformation mode in initially crystalline Ni and Si nanowires. This phenomenon can be partially attributed to the observed reduction of

alumina yield strength and stiffness in amorphous phase [149], compared to crystalline phases, which is related to lower density of the amorphous phases [149]. Similarly, in [150] non-viscous, plastic deformation behavior at low stress values ( $\sim 360$  MPa) in amorphous  $\text{ZrO}_2\text{-Al}_2\text{O}_3$  under compression has been attributed to the low density of the amorphous phase [150]. In the latter case plasticity onset is associated with a sharp yield drop and the formation of localized shear bands throughout the sample [150]. In contrast, Al nanowire amorphization has been explained by increased defect concentration, presumably due to a large surface/volume ratio, which results in reduction of plasticity due to necking type fracture [151]. Subsequently, it is suggested that amorphization may serve as a locally plastic, macroscopically brittle failure mechanism in materials with large dislocation barriers, like ceramics [152].

Instead, high temperature plastic deformation in fine-grained, polycrystalline alumina may take place by diffusional creep or grain boundary sliding [153]. In particular, this behavior is strongly affected by small amount of doping cations, which tend to segregate at the grain boundaries [153]. E.g., Lu doping has been observed to increase the creep resistance, supposedly due to increase in ionic bond strength [153]. In contrast, substitution  $\text{Fe}^{2+}$  cation doping has been found to increase the grain boundary diffusional creep at high temperature [154].

## **5.2 Evaluation of elasticity, plasticity and fracture material properties**

### **5.2.1 $\alpha\text{-Al}_2\text{O}_3$**

#### ***5.2.1.1 Structures and method***

For the calculation of elastic constants energy minimized unit cell structures at  $\pm 5\%$  strain levels were considered.

For the fracture toughness evaluation a bulk supercell with dimensions  $152.5 \times 4.9 \times 152.3$  Å in directions  $[10.0]/[-12.0]/[00.1]$ , resp., and a center located narrow elliptical hole approximating a crack was defined. The crack orientations  $\langle 10.0 \rangle \{00.1\}$  (C-plane) and  $\langle 00.1 \rangle \{10.0\}$  (M-plane) were considered (crack directions given). The hole was filled with He atoms to prevent its closing due to attractive forces during minimization (Figure 5-1).

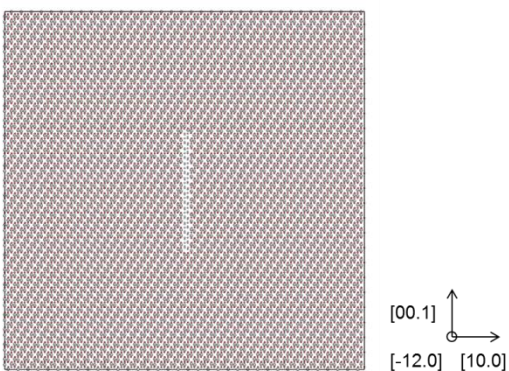


Figure 5-1.  $\alpha$ - $\text{Al}_2\text{O}_3$  ( $152.5 \times 4.9 \times 152.3$  Å supercell) initial  $\langle 00.1 \rangle \{10.0\}$  crack configuration.

The structures were statically deformed in 0.25% tension strain increments, followed by minimization without lateral volume relaxation. The latter condition corresponds to plane strain boundary condition.

### 5.2.1.2 Results

The latest ffield results (Table 5-1) indicate overestimation of  $C_{11}+C_{12}$  and  $C_{13}$ . However, the fracture toughness values and the observed fracture planes (Figure 5-2) [20] indicate good agreement with reference data, in particular the  $\{10.2\}$  plane (R-plane), which is known to have the lowest fracture toughness at room temperature [155]. The occurrence of partially amorphized lower density phases could be explained by comparing the energy vs. volume curves for different phases of Al oxide. These indicate that kappa phase becomes more stable at uniform expansion of  $\sim 7\%$ . Since the radial distribution plots

from the low density regions indicate close similarity to both kappa and alpha phases, an additional unit cell [10.0] expansion with fixed lateral dimensions was performed. The expansion indicated two phase transitions. Subsequently, the phase after the first transition ( $\epsilon=0.24$ ) was identified with the radial distribution of the low density regions (Figure 5-3). A comparison of the unidentified phase against the known phase energy vs. volume curves indicates that the phase becomes more stable than the kappa phase at uniform expansion of ~28% (Figure 5-4a). A DFT test calculation<sup>1</sup> was done for validation (Figure 5-4b). It indicates a barrierless transition from elastic deformation to quasi plastic dissociation, suggesting that the phase transformation in ReaxFF calculation may correspond to an amorphization mechanism.

For evaluation of boundary condition effects a test simulation of an analogous bulk structure with a  $\langle 10.0 \rangle \{ 00.1 \}$  crack, loading in [00.1] direction and lateral relaxation in [10.0] direction was carried out. The results of it indicate no lattice defects even at volume expansion of 59% and elongation of 80% (Figure 5-5). Moreover, there was not observed any phase transformation during the deformation process, which motivated further investigation by comparison with DFT calculations. For comparison an  $\alpha\text{-Al}_2\text{O}_3$  unit cell uniform expansion by 20% in [00.1] direction without lateral relaxation at 0 atm was performed, which was expected to exceed the instability limit of cracked structure energy vs. bulk [103]. At this deformation level the open surface structure was found to have a lower energy than the bulk structure. The DFT calculation<sup>2</sup> indicated no fracture in agreement with the ReaxFF calculation. However, the energy difference with respect to the minimum energy volume structure was about 17% lower than that of ReaxFF. Subsequently it was concluded that under bulk conditions overestimation of fracture/dissociation barriers may occur.

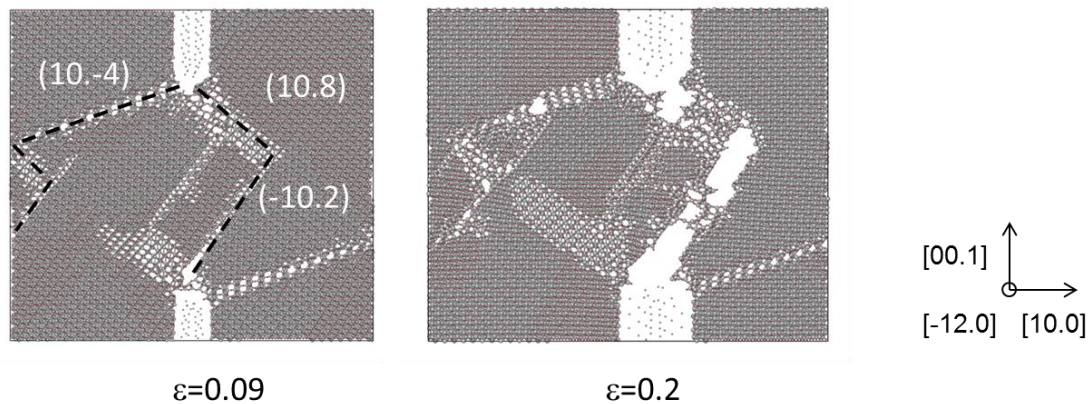
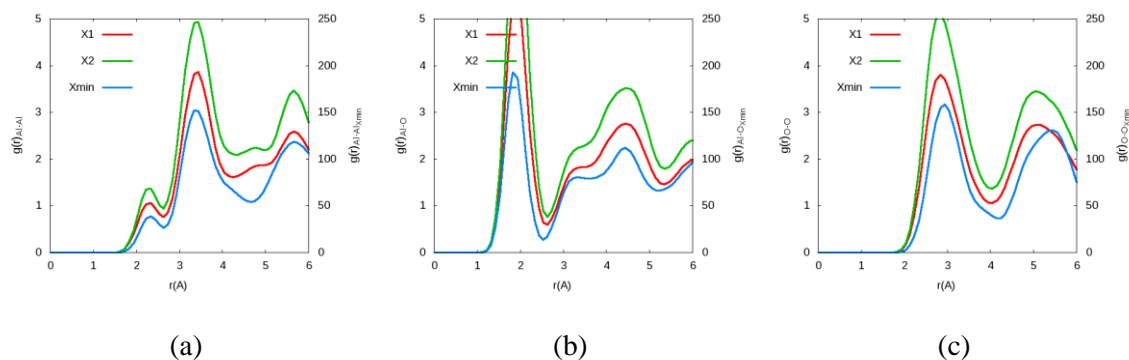
---

<sup>1</sup> Credit to group member Dr. G. Psfogiannakis.

<sup>2</sup> Credit to group member Dr. G. Psfogiannakis.

Table 5-1.  $\alpha$ -Al<sub>2</sub>O<sub>3</sub> elastic constants and fracture toughness values.

	C <sub>11</sub> +C <sub>12</sub> (GPa)	C <sub>13</sub> (GPa)	C <sub>33</sub> (GPa)	K <sub>Ic</sub> (MPa·m <sup>1/2</sup> ) <00.1>{10.0}	K <sub>Ic</sub> (MPa·m <sup>1/2</sup> ) <10.0>{00.1}
DFT/experiment	660 [156]; 604.35 <sup>3</sup>	116 [156]; 109.12 <sup>3</sup>	500 [156]; 455.84 <sup>3</sup>	2.345 [157]	4.54 [155]
ReaxFF (AIOH_Oct2013)	781.33	344.04	506.16	2.413	4.528

Figure 5-2.  $\alpha$ -Al<sub>2</sub>O<sub>3</sub> (152.5x4.9x152.3 Å supercell) <00.1>{10.0} crack propagation snapshots.Figure 5-3. Al-Al (a), Al-O (b), O-O (c) radial distribution functions for bulk stretched structure samples (X1, X2 from red designated phase areas in Figure 5-16) and volume minimized Al<sub>2</sub>O<sub>3</sub> unit cell (Xmin).<sup>3</sup> Credit to group member Dr. G. Psfogiannakis.

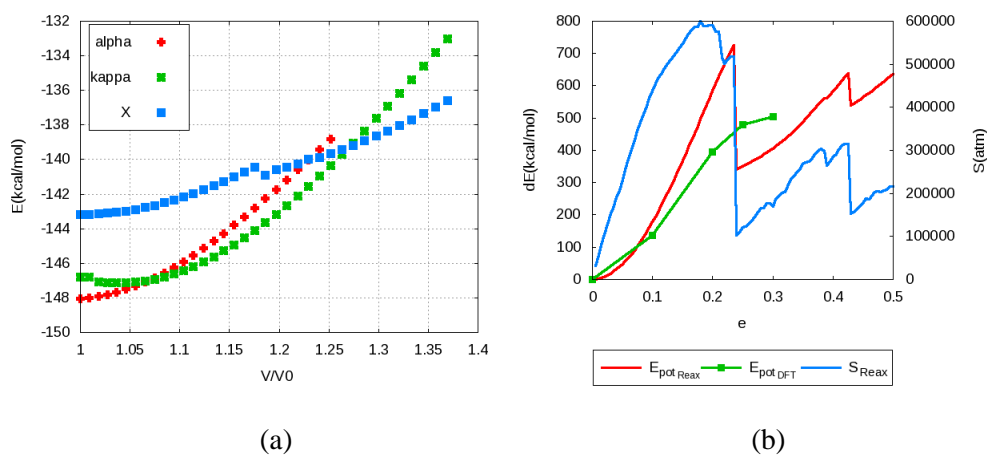


Figure 5-4. Uniform expansion equations of state of  $\text{Al}_2\text{O}_3$  phases (a) and [10.0] expansion equation of state of  $\alpha\text{-Al}_2\text{O}_3$  (b).

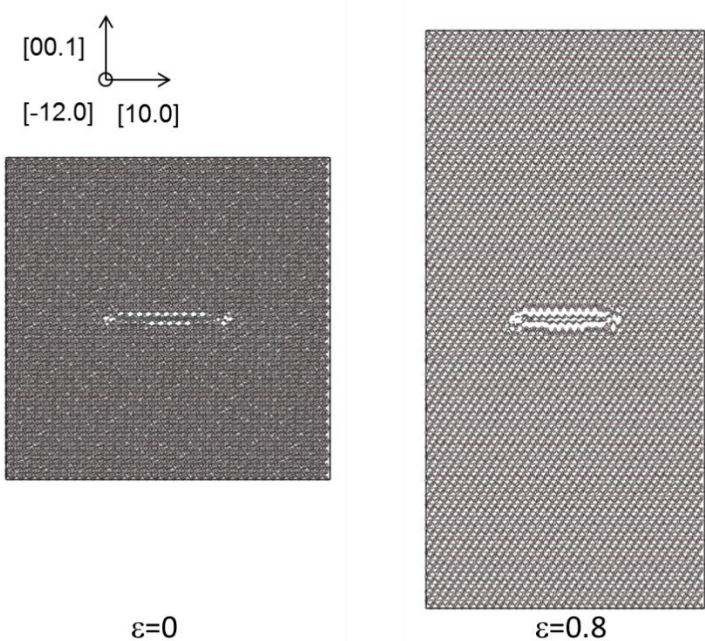


Figure 5-5.  $\alpha\text{-Al}_2\text{O}_3$  ( $152.5 \times 4.9 \times 152.3$  Å) [00.1] stretching with relaxation in [10.0]; configuration snapshots.

## 5.2.2 fcc-Al and fcc-Ni

### 5.2.2.1 Structures and method

Analogously to Al<sub>2</sub>O<sub>3</sub> (section 5.2.1), the elastic constants and fracture toughness values were estimated. For fcc-Al fracture toughness calculation a bulk supercell with 151.1x9.69x150.8 Å dimensions in directions [1-10]/[11-2]/[111], respectively, and a center located 2-layer wide (1-10)[111] He-filled crack was used. For fcc-Ni fracture toughness calculation a bulk supercell with 151.9x7.23x151.9 Å dimensions in directions [100]/[010]/[001], respectively, and a center located 1-layer wide (001)[100] He-filled crack was used. Plane strain boundary conditions were applied. Additionally the intrinsic (ISF) and unstable (USF) stacking fault energies for both materials were calculated.

### 5.2.2.2 Results

The fcc-Al elastic constant values, particularly the  $C_{44}$ , indicate overestimated stiffness as compared to the reference data (Table 5-2). This might be the reason for a significant overestimate of the fracture toughness value according to the strain energy release rate, as compared to the Griffith theory ( $0.52 \text{ MPa}\cdot\text{m}^{1/2}$ ) and the reference data. Instead, the ISF and USF energies indicate good agreement with reference data.

The fcc-Ni elastic constant values indicate underestimation of  $C_{11}$  and overestimation of  $C_{44}$  (Table 5-3). Similarly to the fcc-Al result, a significant overestimation of the fracture toughness is obtained according to the strain energy release rate calculation. Hence the overestimation of  $C_{44}$  appears to be a possible reason for the difference for both materials. In contrast to the USF energy, which indicates good agreement with reference data, the ISF energy estimate indicates artificial stability, which implies higher barriers for trailing partial dislocations.

Table 5-2. fcc-Al elastic constants, fracture toughness values, intrinsic and unstable stacking fault energies.

	$C_{11}$ (GPa)	$C_{12}$ (GPa)	$C_{44}$ (GPa)	$K_{Ic}$ (MPa·m <sup>1/2</sup> ) $\langle 1-10 \rangle \{111\}$	ISF(mJ/m <sup>2</sup> )	USF(mJ/m <sup>2</sup> )
DFT/experiment	104 [158]; 116 [159]	55.9 [158]; 64.8 [159]	29.5 [158]; 30.9 [159]	0.45 [110]; 0.52 [160]	140; 93 [160]	188; 143 [160]
ReaxFF (AlOH_Oct2013)	133	64.3	58.1	0.91	98	140

Table 5-3. fcc-Ni elastic constants, fracture toughness values, intrinsic and unstable stacking fault energies.

	$C_{11}$ (GPa)	$C_{12}$ (GPa)	$C_{44}$ (GPa)	$K_{Ic}$ (MPa·m <sup>1/2</sup> ) $\langle 001 \rangle \{100\}$	ISF(mJ/m <sup>2</sup> )	USF(mJ/m <sup>2</sup> )
Experiment/EAM/EMP	246.5 [161]	147.3 [161]	124.7 [161]	1 [162]	54 [163]	287 [163]
ReaxFF [100]	217.6	151.2	151.2	1.77	-17	236

### 5.3 $\alpha$ -Al<sub>2</sub>O<sub>3</sub> anisotropy and strain study

#### 5.3.1 Structures

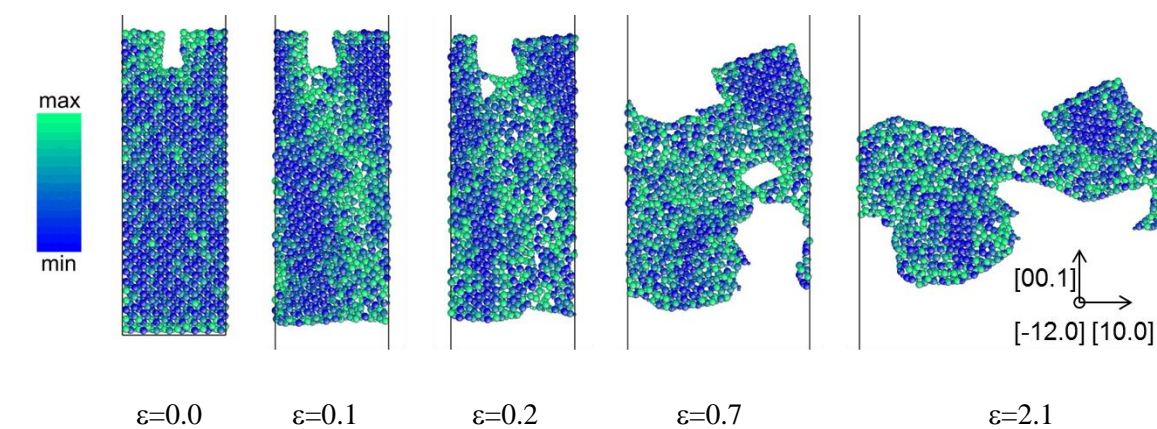
For this study 2 slab geometries of thickness 101.7 Å and rectangular surface notch/blunt edge crack orientations [00.1](10.0) and [00.1](-12.0) (A-plane) were defined. The (00.1) surface was defined as the open surface with the estimate that for subsequent study of Al<sub>2</sub>O<sub>3</sub>/Al interface structures the specific surface would be the most suitable [164] as well being the most stable [123]. The periodic dimensions were 33.8x4.9 Å ([10.0]/[1-2.0]) for tensile deformation in [10.0] direction and 8.5x34.2 Å ([10.0]/[1-2.0]) for tensile deformation in [-12.0] direction. The slab surfaces were Al-terminated, since these are known to be more stable than O-terminated surfaces [123]. Considering the relatively small [00.1] dimension, the given boundary conditions are considered as plane stress conditions.

### 5.3.2 Method

The simulations were performed with constant volume-temperature (NVT) ensemble regime at 300K with a temperature damping constant of 100 fs. The tension was applied by scaling the respective axis dimension at each iteration to simulate the engineering strain rate of  $5e-6 \text{ fs}^{-1}$ , the latter being 2-3 orders of magnitude lower than the hypervelocity impact loading rates used in studies [29, 146]. To reduce the loading induced nonequilibrium effects, the loading was applied in 10% increments, followed by relaxation periods of 20 ps. An additional strain analysis was done for the [10.0] direction loaded structure with cutoff radius of 6 Å and time increments of 10 ps.

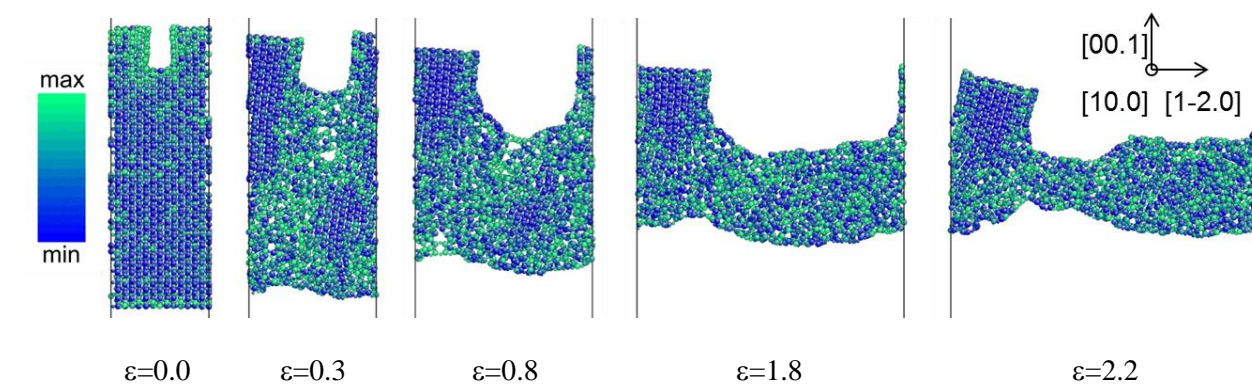
### 5.3.3 Results and Analysis

The deformation of the both structures proceeds through the occurrence of an amorphous shear band, which subsequently expands over the whole thickness of the structure (Figure 5-6). A few small crystalline grains are left inside the band. For the structure with strain applied in [10.0] direction the deformation forms voids in the shear band and the failure is observed at  $\epsilon=2$ . This deformation type has been observed experimentally both at room [165] and elevated temperatures [166]. Instead, for the structure with strain applied in [-12.0] direction the deformation yields a necking type transformation with the initially formed voids closing (Figure 5-7). The latter simulation was stopped at  $\epsilon=2.7$ . The amorphization phenomenon is interpreted as a combination of plastic shear deformation mechanism [148] and highly increased potential energy induced phase transformation due to loading [143]. The distinctly plastic deformation observed in both cases is attributed to the size effect related flaw tolerance [30, 167, 168] due to the high value of surface-to-volume ratio ( $\sim 200 \mu\text{m}^{-1}$ ) [169]. However, the potential energy and overall tensile stress plots indicate that overall structure behavior is identical (Figure 5-8). Hence for further studies the [10.0] stretching direction was selected due to its lower failure strain value.



$\epsilon$	$S_{\min}$ (GPa)	$S_{\max}$ (GPa)
0.0	19.5	40.4
0.1	23.6	52.6
0.2	25.0	55.0
0.7	27.8	59.9
2.1	28.5	59.5

Figure 5-6.  $\alpha$ -Al<sub>2</sub>O<sub>3</sub> slab (33.8x4.9x101.7 Å) [10.0] stretching snapshots; octahedral stress distribution.



$\epsilon$	$S_{\min}$ (GPa)	$S_{\max}$ (GPa)
0.0	19.5	40.4
0.3	26.2	56.7
0.8	27.9	59.8
1.8	28.3	59.4
2.2	27.7	59.1

Figure 5-7.  $\alpha$ -Al<sub>2</sub>O<sub>3</sub> slab (34.2x8.5x101.7 Å) [-12.0] stretching snapshots; octahedral stress distribution.

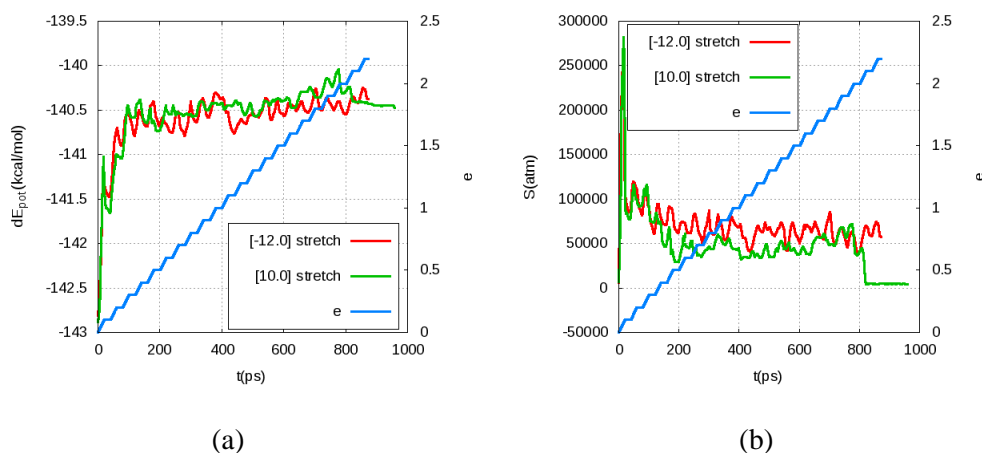


Figure 5-8. Potential energy (a) and tensile stress (b) vs. time: comparison for [10.0] and [-12.0] strained  $\alpha$ - $\text{Al}_2\text{O}_3$  slabs.

The distributions of maximum principal  $E_{\text{max}}$  and octahedral  $E_{\text{oct}}$  strains corresponding to Green and Almansi strain tensors (Figure 5-9) indicate that strains are concentrated in the amorphized regions, as expected. More distinct differences and trends can be observed by comparing the mean strain criterion values (Figure 5-10). A general observation for all curves is a discontinuous change in slope at  $\sim 450$  ps ( $\varepsilon=1$ ), which is attributed to crack propagation and the resulting rotation of the structure due to force moment balance. The rotation facilitates shear sliding failure in the amorphized region due to the angle of  $\sim 45^\circ$  with respect to the stretch direction. The mean  $E_{\text{max\_Green}}$  values increase close to linearly until failure, whereas the mean  $E_{\text{max\_Almansi}}$  values approach an asymptotic value of 0.5. Both trends can be explained in a simplified way by considering uniform uniaxial tension deformation gradient. By straightforward estimation of the respective infinite strain limits it is found that for Green strain the limit is infinity, whereas for Almansi strain the limit is 0.5, which is close to the observed value of  $\sim 0.4$ . Instead, the mean  $E_{\text{oct}}$  values for both tensors increase linearly until failure. This can be explained by estimating the  $E_{\text{oct}}$  limit of infinite strain for the simplified case of uniform simple shear deformation gradient, which equals infinity for both strain tensors due to the non-negative definition of the criterion. Furthermore, by considering the close similarity of  $E_{\text{max\_Green}}$  and  $E_{\text{oct\_Green}}$  curves it can be concluded that the failure is primarily due to shear deformation.

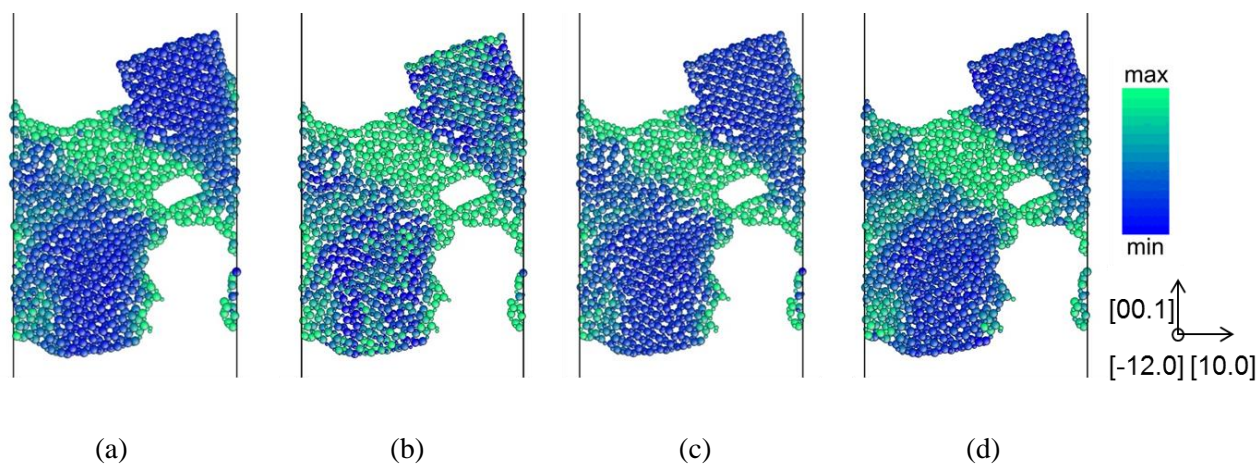


Figure 5-9. Maximum principal and octahedral strain distributions according to Green (a,c) and Almansi (b,d) strain tensors for [10.0] strained  $\alpha$ -Al<sub>2</sub>O<sub>3</sub> slab (33.8x4.9x101.7 Å,  $\epsilon=0.8$ ): distribution comparison.

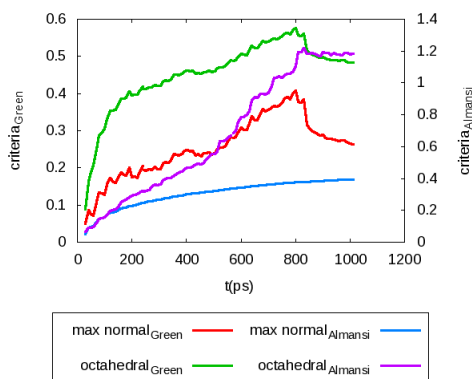


Figure 5-10. Mean maximum principal and octahedral strains according to Green and Almansi strain tensors for [10.0] strained  $\alpha$ -Al<sub>2</sub>O<sub>3</sub> slab.

To summarize:

- the [10.0] stretching direction was selected for further studies due to its lower failure strain value
- based on the close similarity of mean  $E_{\max\_Green}$  and  $E_{\text{oct}\_Green}$  values it could be concluded that the material failure is primarily due to shear deformation.

## 5.4 Loading rate and relaxation study

### 5.4.1 Structures and Method

In order to evaluate the effect of loading rate on the deformation behavior in  $\text{Al}_2\text{O}_3$  structures, two simulations using the [10.0] direction loaded 101.7 Å thick (00.1) slab structure with periodic dimensions of 33.8x4.9 Å ([10.0]/[-12.0]) and a [00.1](10.0) rectangular surface notch were performed. The NVT ensemble at 300K with temperature damping of 100 fs was used. Due to the relatively small [00.1] dimension, the given boundary conditions are considered as plane stress conditions.

In the first simulation a deformation loading rate of  $5\text{e-}4 \text{ fs}^{-1}$  was applied, which corresponds to the hypervelocity impact loading rate used in [29]. In the second simulation a single strain increment of 10% at  $5\text{e-}6 \text{ fs}^{-1}$  strain rate with box strain adjusted [17] NVT ensemble was performed, followed by NPT based relaxation to 0 atm using pressure damping constant of 5000 fs.

A large scale  $\text{Al}_2\text{O}_3$  (00.1) slab structure with thickness of 152.5 Å, periodic dimensions of 152.3x4.9 Å and identical surface notch/loading configuration was used for a lower strain rate comparison. For this structure loading regimes of  $5\text{e-}6 \text{ fs}^{-1}$  5% (5 ps) stretching alternating with variable relaxation periods, which would yield close to fully relaxed structures after each loading stage, and of  $5\text{e-}6 \text{ fs}^{-1}$  0.25% (0.5ps) strain increments alternating with 5ps relaxation periods were compared. Since the loading stages for the second regime were of comparatively small duration, the loading rate could be considered equivalent to effective constant loading rate of  $5\text{e-}7 \text{ fs}^{-1}$ . The simulations were performed with NPT ensemble at 300K and 0 atm with temperature damping of 100 fs, pressure damping of 5000 fs and 2 pressure chain thermostats. The boundary conditions were considered as plane stress due to 0 atm [-12.0] relaxation.

A large scale  $\text{Al}_2\text{O}_3$ -terminated fcc-Al slab structure was considered for evaluation of strain rate effects in the metal. The structure has periodic dimensions of 152.3x9.77 Å in directions [1-10]/[11-2],

respectively, and thickness of 123.4 Å. The (111) outer slab surfaces were interfaced with unit-cell thick (12.71 Å) Al<sub>2</sub>O<sub>3</sub> layers having an orientation identical to the structures above. The (00.1) oxide interface was defined as Al-terminated, which energetically matches OK scaled experimental results according to [164]. A rectangular notch was defined for one of the oxide layers. On the notch side the fcc stacking with respect to O positions of alumina, which has been found to be the most stable configuration among Al-terminated oxide surfaces and the closest to experimental values [164], was used, whereas for the defect free side the on-top stacking was applied for comparison. The strain rates of 5e-6/5e-5/5e-4 fs<sup>-1</sup> in [1-10] direction with alternating deformation cycles of 10/1/0.05 ps (dε=0.05/0.05/0.025) and relaxation cycles of 20/20/10 ps, respectively, were applied. The used ensemble settings are given in Table 5-4. The boundary conditions were considered as plane stress due to 0 atm [11-2] relaxation.

Table 5-4. Ensemble settings for α-Al<sub>2</sub>O<sub>3</sub> slab loading rate study.

Loading rate (fs <sup>-1</sup> )	Time step (fs)	Loading interval (ps)	Relaxation interval (ps)	Ensemble	Temperature damping (fs)	Pressure damping (fs)
5e-6	0.2	10	20	NPT	100	1000
5e-5	0.2	1	20	NPT	100	1000
5e-4	0.1	0.05	10	NPT/NVT [170]	300	5000

#### 5.4.2 Results and Analysis

For the first, multiple increment, small scale Al<sub>2</sub>O<sub>3</sub> slab simulation, the stress distribution (Figure 5-11) indicates an initial shock wave, which results in void coalescence caused failure at ε=0.4, accompanied by localized amorphization. The strain rate effect can be estimated by comparing the potential energy and stress responses with those of the same structure at 5e-6 loading rate (section 5.3.3). The plots indicate significantly lower strength and strain energy capacity (Figure 5-13), except for a transition state according to potential energy between ε=0.1 and ε=0.2. Charge distribution plots (Figure 5-12) indicate charge polarization in the fracture region before the fracture, which allows for the suggestion that it may facilitate the fracture. The asymmetry of the Al atom charge distribution after

fracture is similar to the charge distributions observed for brittle fracture of silicon both experimentally and in simulations [171].

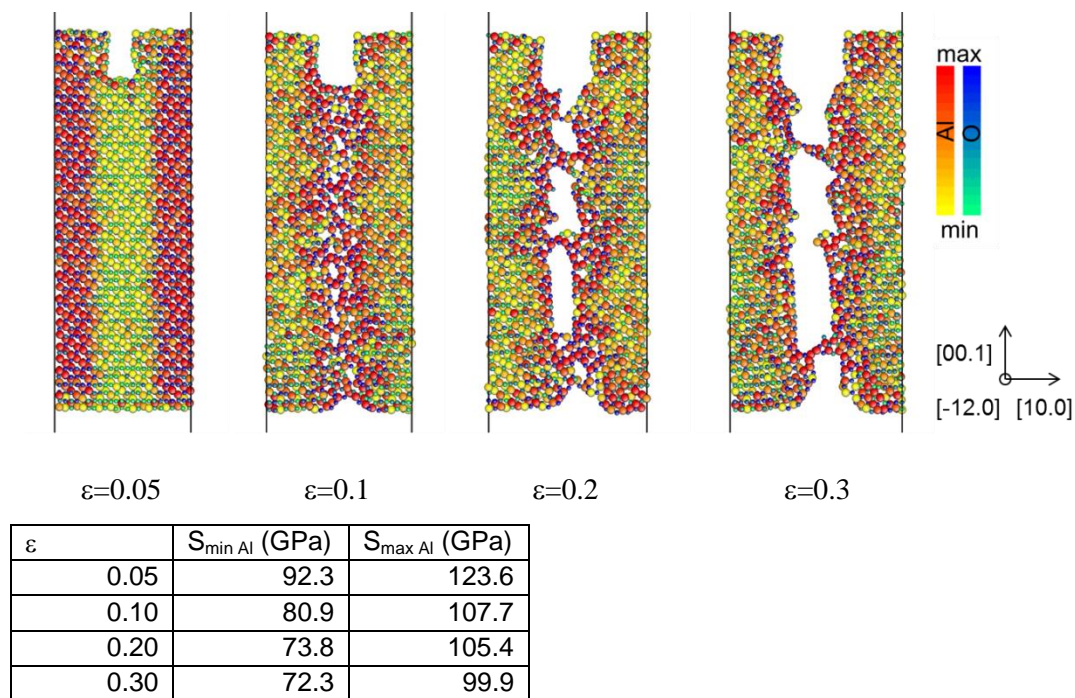


Figure 5-11.  $\alpha$ - $\text{Al}_2\text{O}_3$  slab ( $33.8 \times 4.9 \times 101.7 \text{ \AA}$ ) [10.0] stretching snapshots; max. normal stress distribution.

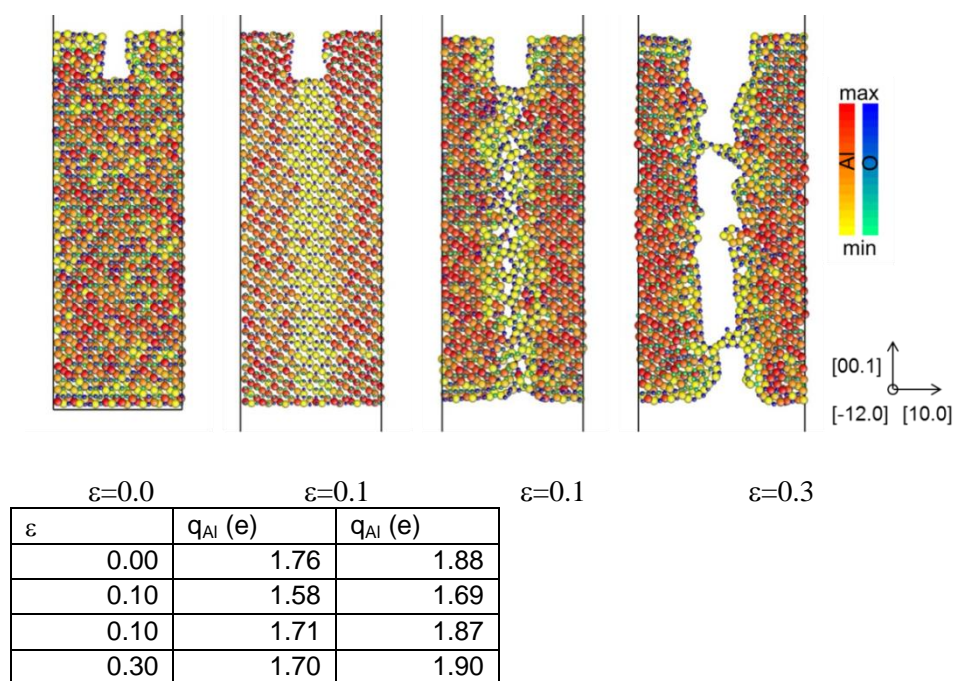


Figure 5-12.  $\alpha$ - $\text{Al}_2\text{O}_3$  slab ( $33.8 \times 4.9 \times 101.7 \text{ \AA}$ ) [10.0] stretching snapshots; charge distribution.

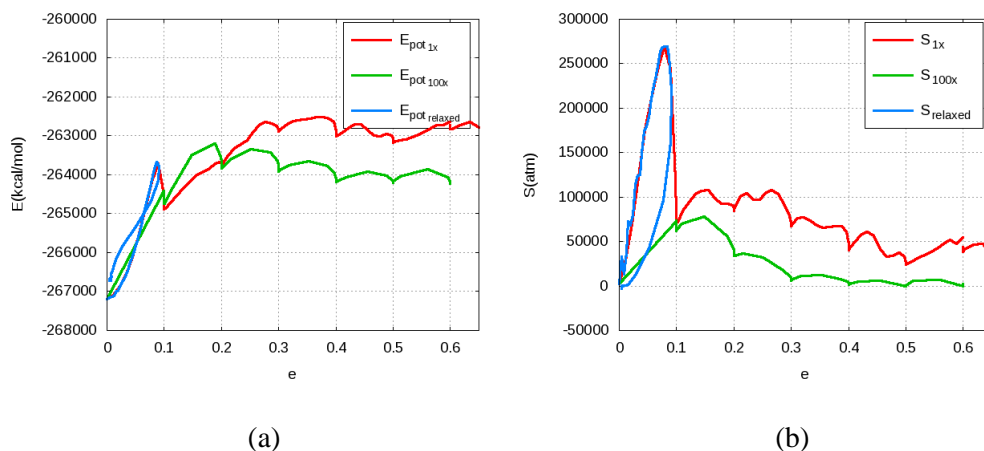
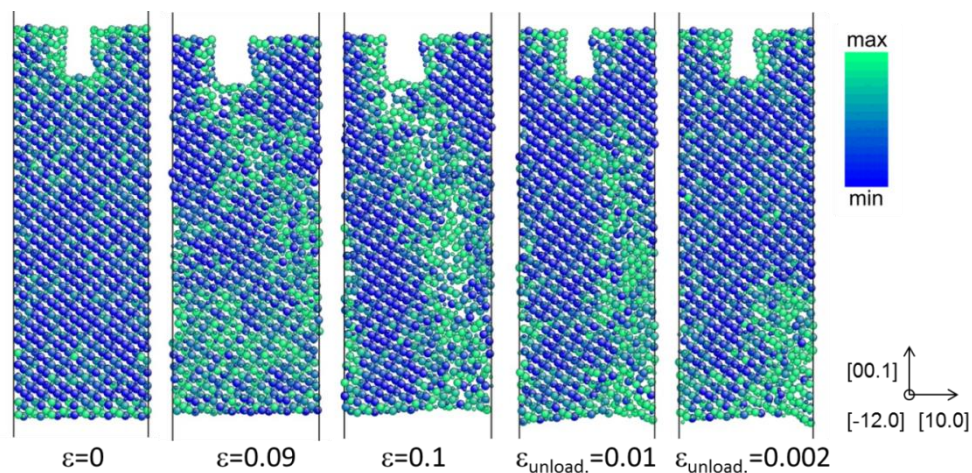


Figure 5-13. Potential energy (a) and tensile stress (b) vs. strain: comparison for [10.0] strained  $\alpha$ - $\text{Al}_2\text{O}_3$  slabs ( $1x=5e-6 \text{ fs}^{-1}$ ).

The second, single increment, small  $\text{Al}_2\text{O}_3$  slab simulation snapshots indicate that for the given applied strain level the amorphization is partially reversible upon load removal (Figure 5-14). This observation is confirmed by the radial distribution function plots and the minor change in potential energy compared to the initial state (Figure 5-15), which is attributed to the localized amorphous region.



$\epsilon$	S (GPa)	S (GPa)
0.0	19.5	40.4
0.09	30.0	50.9
0.10	25.7	53.4
0.01	20.4	45.7
0.002	20.2	42.8

Figure 5-14.  $[10.0]$  strained  $\alpha$ - $\text{Al}_2\text{O}_3$  slab ( $33.8 \times 4.9 \times 101.7 \text{ \AA}$ ) amorphization and re-crystallization snapshots; octahedral stress distribution.

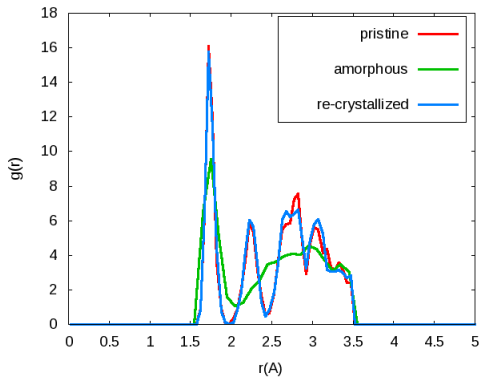


Figure 5-15.  $\alpha$ - $\text{Al}_2\text{O}_3$  radial distribution upon amorphization and subsequent re-crystallization.

The large scale  $\text{Al}_2\text{O}_3$  slab structure simulations yielded approx. ratio of 2.4 for the mean loading rates of the variable relaxation vs. constant relaxation loading regimes, respectively. The comparison of the potential and tensile stress curves indicates that both regimes are similar up to the emission of a dislocation along a  $\{-10.2\}$  plane (Figure 5-18). After the emission the variable relaxation/high increment loading regime indicates higher stiffness due to a higher level of potential energy reached. The increase in energy is apparently facilitated by the formation of a lower density phase band (Figure 5-16), analogous to the one discussed in section 5.2.1.2. Through this band a crack subsequently develops. Instead, the constant relaxation/small increment regime indicates no significant increase in potential energy after the dislocation emission, which is apparently related to formation of localized smaller density regions and crack formation along the dislocation path (Figure 5-17). The overall axial stress responses indicate similar differences for both structures (Figure 5-18b), which result in the failure strain of the constant relaxation regime structure ( $\sim 0.25$ ) being significantly less than that of the variable relaxation regime structure ( $\sim 0.4$ ). Yet the potential energy levels at failure (Figure 5-18a) have similar values for both structures, which implies that the energy capacity of the material at failure may be less sensitive to the loading regime.

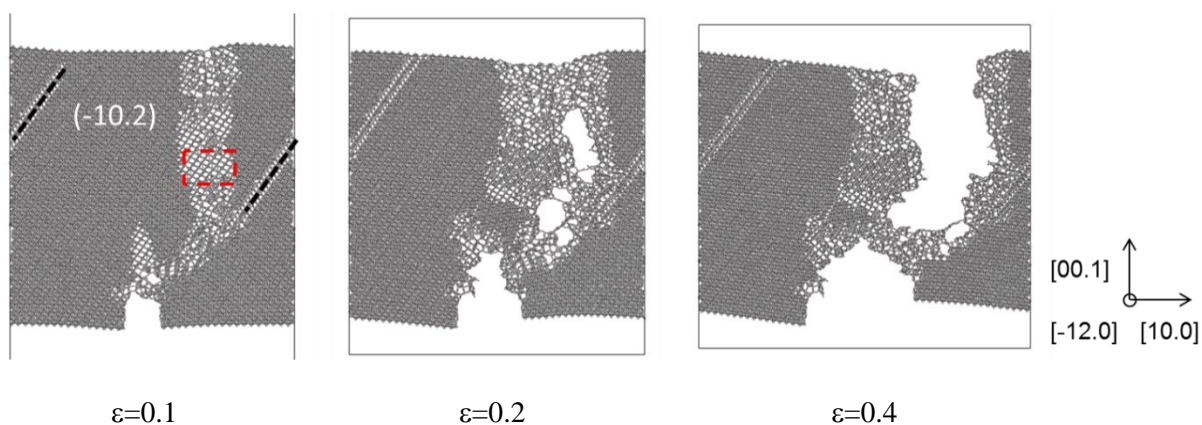


Figure 5-16.  $\alpha$ -Al<sub>2</sub>O<sub>3</sub> slab (152.3x4.9x152.5 Å) [10.0] deformation with variable relaxation time; configuration snapshots.

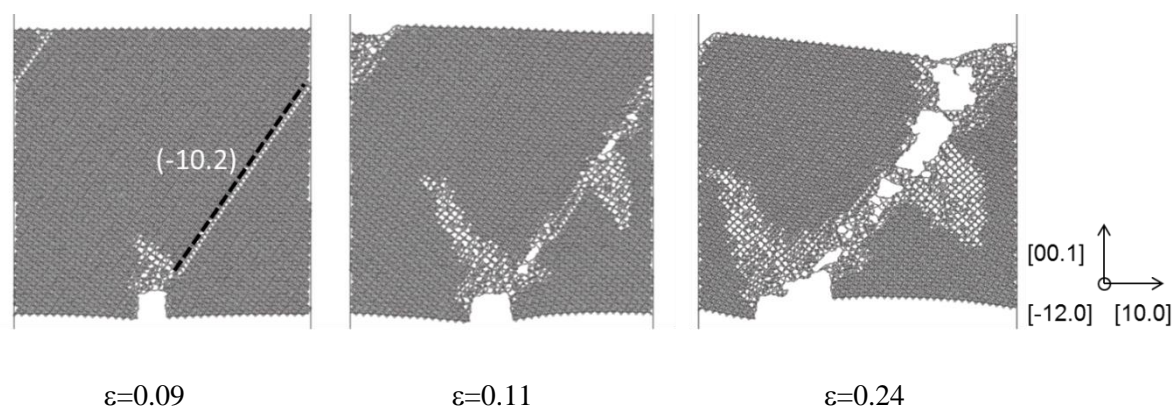


Figure 5-17.  $\alpha$ -Al<sub>2</sub>O<sub>3</sub> slab (152.3x4.9x152.5 Å) [10.0] deformation with constant relaxation time; configuration snapshots.

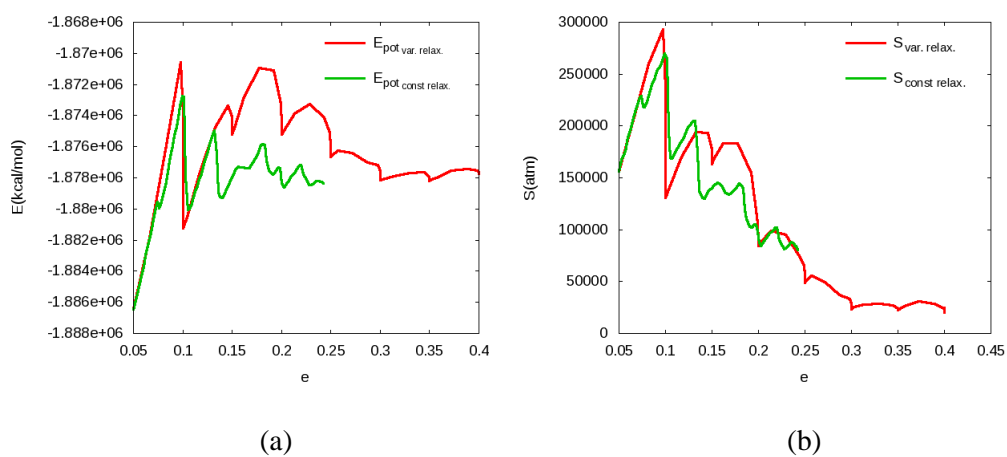


Figure 5-18. Potential energy (a) and tensile stress (b) vs. strain: loading regime comparison for [10.0] strained  $\alpha$ -Al<sub>2</sub>O<sub>3</sub> slabs.

The fcc-Al slab potential energy and tensile stress responses indicate that higher strain rates may enhance stiffness and plasticity as long as the material response remains ductile, as suggested by more rapid initial potential energy rise (peak values reached at  $\epsilon=0.15/0.1/0.03$ , resp.) and the lower failure strain ( $\epsilon=0.4$ ) for the lowest strain rate (Figure 5-21). The observation is in qualitative agreement with results from experimental studies with significantly lower strain rates [172]. Yet, since the failure mode for the 2 highest strain rates involves transition to a brittle cleavage fracture mode (Figure 5-19, Figure 5-20), the increase in expected failure strains at higher strain rates is likely due to the non-equilibrium dynamics effects (section 5.9.3). An additional observation regarding the relaxation of the different stacking cases at the Al/Al<sub>2</sub>O<sub>3</sub> interface is the different levels of rearrangement. For the on-top stacking case a significant rearrangement is formed by transition to an O-terminated interface layer, which is reported to have about an order higher adhesion energy than the respective Al-terminated interface [164]. Instead, for the fcc stacking case rearrangement by transition to an O-terminated interface layer is observed only in the proximity of the notch, while a transition to O-terminated free surface occurs at several locations (Figure 5-22). The latter observation is assumed to be a result of interface rearrangement, since no analogous rearrangement is observed for Al<sub>2</sub>O<sub>3</sub> slabs.

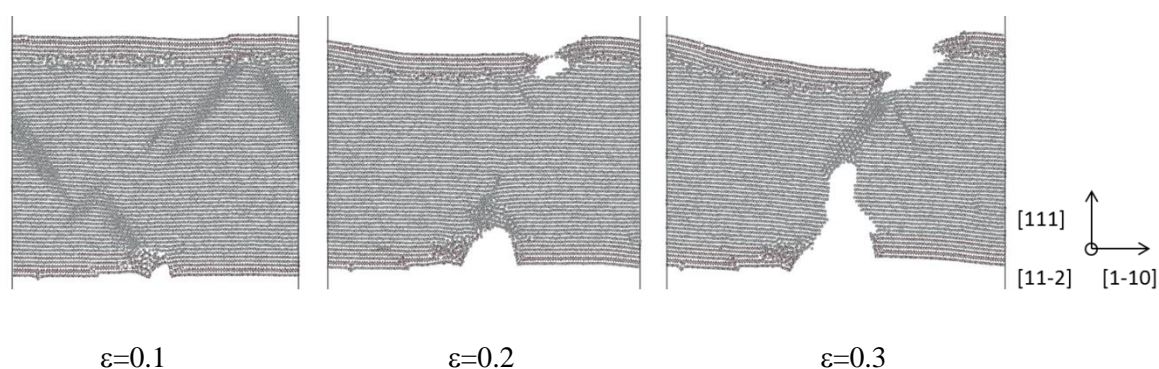


Figure 5-19. [1-10]  $5e-6 \text{ fs}^{-1}$  strained  $\alpha\text{-Al}_2\text{O}_3$ -terminated fcc-Al slab ( $152.3 \times 9.77 \times 148.8 \text{ \AA}$ ); configuration snapshots.

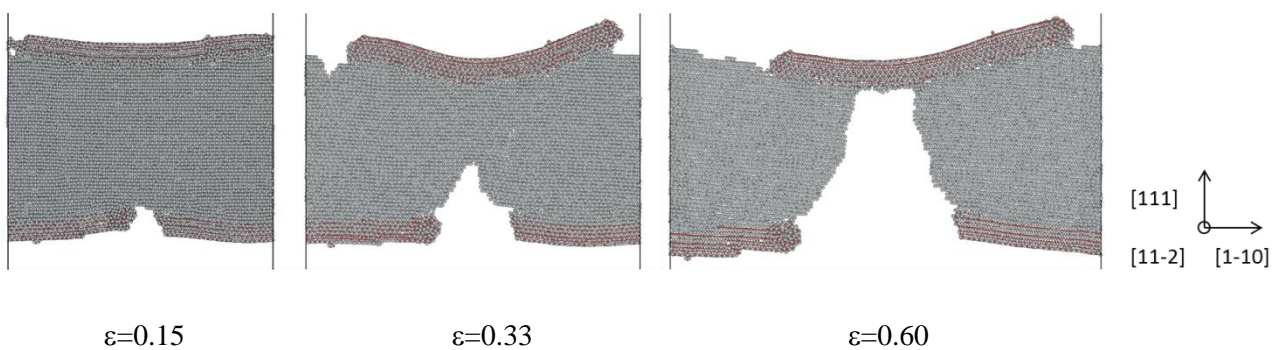


Figure 5-20. [1-10]  $5e-4 \text{ fs}^{-1}$  strained  $\alpha\text{-Al}_2\text{O}_3$ -terminated fcc-Al slab ( $152.3 \times 9.77 \times 148.8 \text{ \AA}$ ); configuration snapshots (Al – grey, O – red).

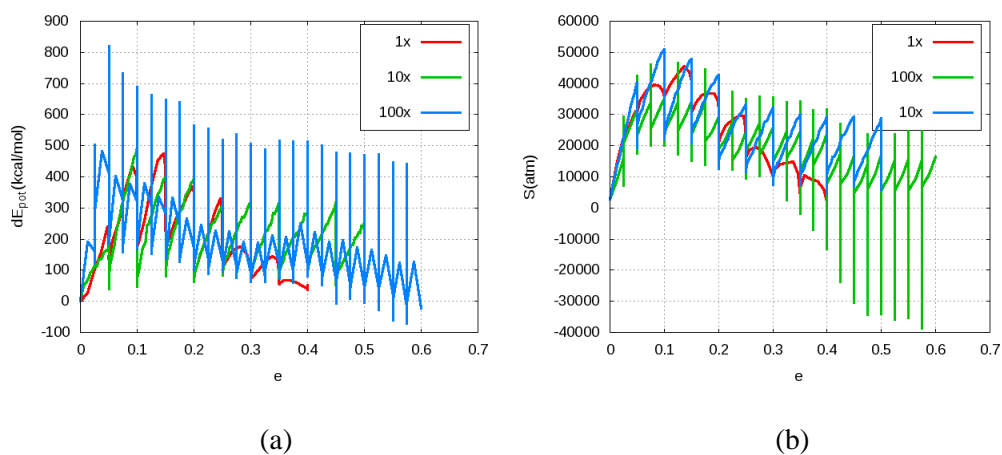


Figure 5-21. Potential energy (a) and tensile stress (b) vs. strain for [1-10] strained  $\alpha\text{-Al}_2\text{O}_3$ -terminated fcc-Al slab: loading rate comparison ( $1x=5e-6 \text{ fs}^{-1}$ ).

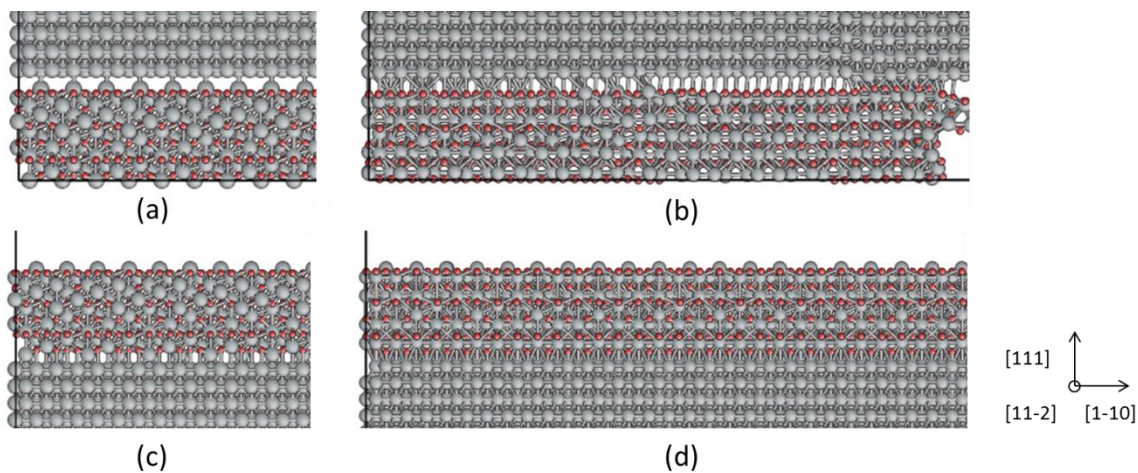


Figure 5-22. On-top (c,d) and fcc (a,b)  $\alpha\text{-Al}_2\text{O}_3$ /fcc-Al interface stacking (with respect to O) configurations prior to and after minimization (Al – grey, O – red).

### 5.4.3 Summary

$\alpha$ -Al<sub>2</sub>O<sub>3</sub> slabs:

- Significantly lower strength and strain energy capacity for the shock loading rate is predicted.
- Charge polarization it may facilitate the fracture.
- Amorphization is partially reversible upon load removal.
- Constant relaxation regime is expected to yield more brittle and reduced strength material response.
- Energy capacity of the material at failure may be less sensitive to the loading regime for loading rates below shock loading.

fcc-Al slab:

- Transition to brittle cleavage failure mode before fracture, at strain rate of  $5e-4 \text{ fs}^{-1}$ .
- Increasing strain rates below transition to brittle failure may enhance stiffness and plasticity according to failure strain.

## 5.5 $\alpha$ -Al<sub>2</sub>O<sub>3</sub> fatigue study

### 5.5.1 Structures and Method

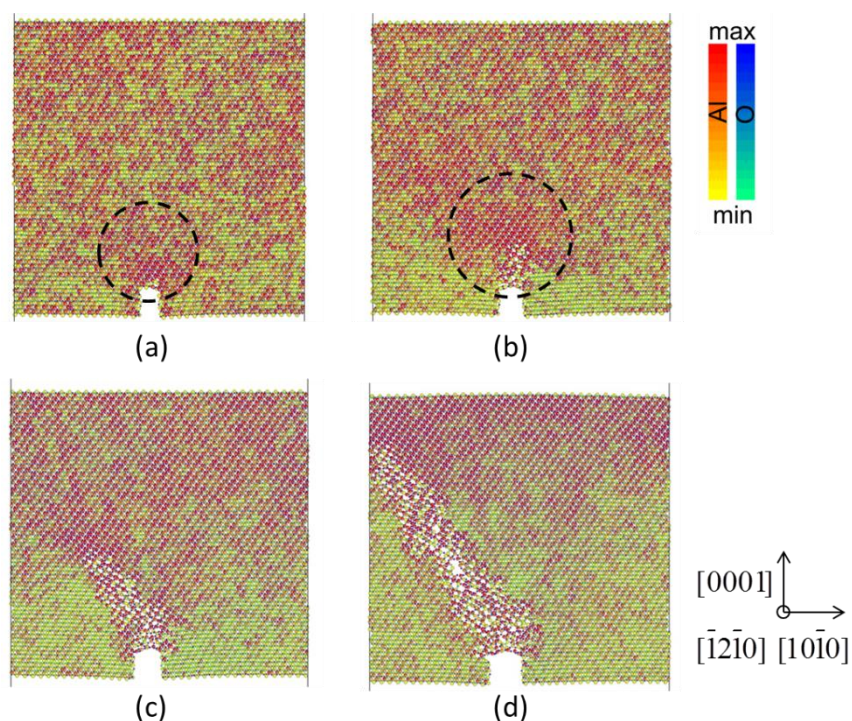
(00.1) slab structures with periodic dimensions of  $152.3 \times 4.88 \text{ \AA}$  in [10.0]/[-12.0] directions, respectively, thickness of  $152.5 \text{ \AA}$  and rectangular (10.0)[10.0] surface notch were used in the study.

Both dynamic and static cyclic deformation in [10.0] direction was simulated in order to evaluate finite temperature effects versus the static/low temperature case. For the dynamic simulation a loading rate of  $5e-6 \text{ fs}^{-1}$  in 0.25% (0.5ps) strain increments alternating with 5ps relaxation periods was applied. The loading frequency was  $1.9 \text{ ns}^{-1}$ . The NVT/NPT ensemble at 300K with 100 fs damping, 0 atm with 5000 fs damping and 1 thermostat chain on barostat was used. For the static simulations 0.25% strain increments with subsequent minimization were applied. In addition to the 0 atm volume minimized structure a 7% [10.0]/[-12.0] pre-strained structure was simulated for comparison. For static simulations

the [-12.0] dimension was kept fixed at its initial value. Thus plane stress conditions were obtained for the dynamic simulation and mixed plane strain/plane stress conditions in directions [-12.0]/[00.1] for the static systems. For all systems the tensile strain was increased up to a strain level after fracture initiation, subsequently reduced to a compression level within elastic response range and reloaded in tension up to a second fracture initiation. For the volume minimized static simulation a second loading cycle was performed. For comparison separate compression simulations from the initial state for all systems were performed for comparison.

### **5.5.2 Results and Discussion**

Stress distributions for all structures indicate structure-wide stress gradients up to crack surface vicinity (Figure 5-23), which correspond to purely elastic/brittle material response. The main numerical results are summarized in Table 5-5. These indicate that temperature enhances plasticity, since the system at 300K fails at a larger strain during the second tension cycle, as compared to the first cycle. Yet the overall brittleness is increased at 300K due to lower failure strains, stresses and potential energy as compared to the static simulations. Furthermore, the pre-expanded structure indicates lower failure stresses and potential energy as compared to the volume minimized static structure, although both failure strains are approximately identical and decreasing for repeated cycles. Thus it may be concluded that pre-expansion weakens the material response, as expected due to increased stress triaxiality, and that under the given loading conditions low cycle fatigue is likely to occur in the static systems, whereas shakedown [173] may occur for the 300K system.



configuration	$\epsilon$	$S_{\min \text{ Al}}$ (GPa)	$S_{\max \text{ Al}}$ (GPa)
a	0.00	86.6	109.6
b	0.02	93.8	120.5
c	0.09	94.9	127.1
d	0.10	85.4	124.4

Figure 5-23. [10.0] strained  $\alpha$ - $\text{Al}_2\text{O}_3$  slab ( $152.3 \times 4.9 \times 152.5$  Å) snapshots; max. normal stress distribution.

Table 5-5. 1<sup>st</sup> and 2<sup>nd</sup> loading cycle failure strains, stresses and potential energies for [10.0] strained  $\alpha$ - $\text{Al}_2\text{O}_3$  slab.

T(K)	$\epsilon_0$	$\epsilon_{f1}$	$\epsilon_{f2}$	$dS_{f1}$ (atm)	$dS_{f2}$ (atm)	$dE_{f1}$ (kcal/mol)	$dE_{f2}$ (kcal/mol)
300	0	0.095	0.13	270000	175000	20500	17000
0	0.07	0.150	0.120	390000	260000	60000	23000
0	0	0.145	0.125	600000	540000	106000	92000

More insights can be obtained from the potential energy and stress response plots (Figure 5-24).

Due to the positive shifts in minimum energy locus along potential energy and strain axes it can be concluded that temperature and pre-expansion reduce crack healing probability and facilitate kinematic hardening effect. Instead, the volume minimized static structure indicates no kinematic hardening and notable crack healing due to negligible increase in potential energy and evident closing of most of the cracks upon compression.

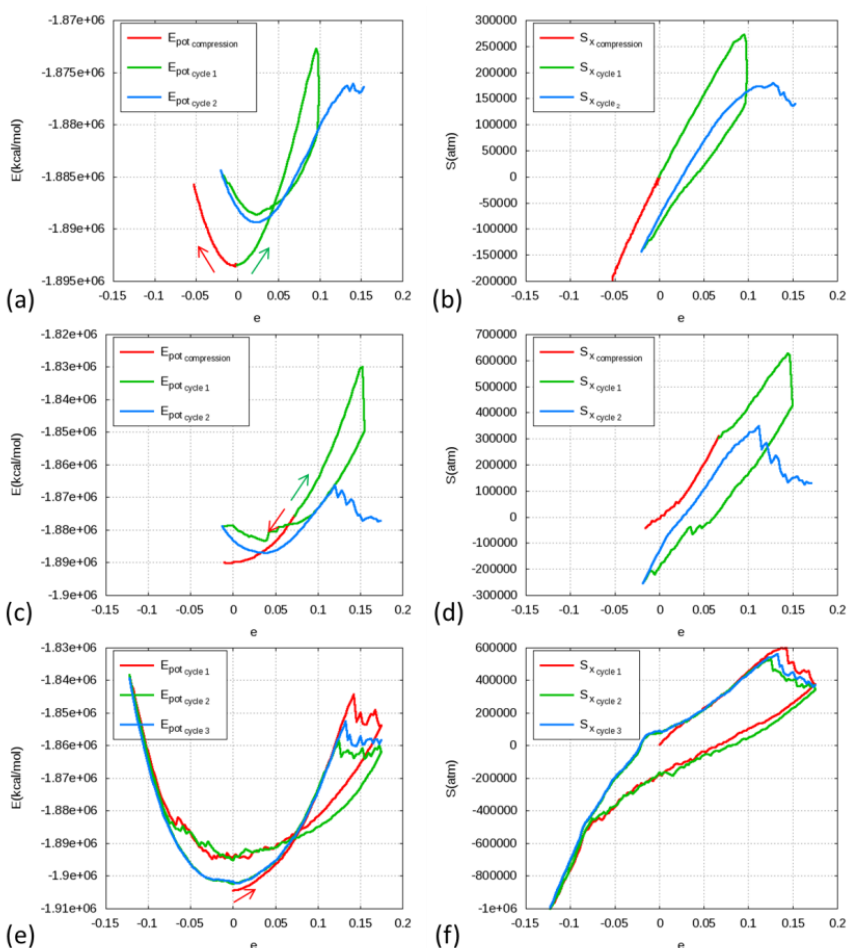


Figure 5-24. Potential energy and tensile stress vs. strain for [10.0] strained  $\alpha$ - $\text{Al}_2\text{O}_3$  slabs at 300K (a,b),  $\epsilon_0=0.0$ , and at 0K with  $\epsilon_0=0.07$  (c,d) and  $\epsilon_0=0.0$  (e,f).

The extent of strain rate effect for the 300K system could be estimated by performing a constant strain relaxation shortly before reaching the maximum strain of  $\epsilon=0.1$  during the first cycle (Figure 5-25), which indicates that fracture strain level is slightly overestimated compared to quasi-static loading, the deviation being ascribed to differences in dynamics of loading and amorphization/fracture propagation processes. Slight dynamics change in structure relaxation during unloading compared to constant strain level is also observed. Subsequently, the overall strain rate effect is not considered being significant.

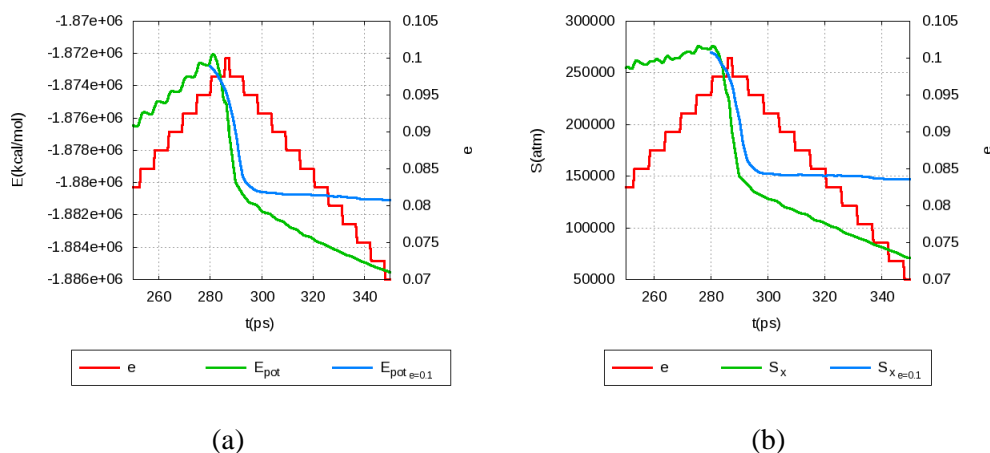


Figure 5-25. Potential energy (a) and tensile stress (b) vs. time for [10.0] strained  $\alpha$ - $\text{Al}_2\text{O}_3$  slab at 300K.

It is worth indicating that the volume distributed crack pattern of the volume minimized static structure is notably different from the pre-expanded static or 300K volume minimized systems, which indicate a single crack propagating along  $\{10.-2\}$  and  $\{10.2\}$  slip planes (Figure 5-26-Figure 5-28), respectively. Both  $\{10.-2\}$  and  $\{10.2\}$  are experimentally detected fracture planes [20, 155]. In the case of the 300K system a low density band forms prior to the crack formation, suggesting that a fracture mechanism at room temperature could be  $\{10.-2\}$  slip initiated layer-wise amorphization (Figure 5-29), in agreement with the unit cell [10.0] deformation results in section 5.2.1.2. It was also observed that repeated loading in the volume minimized static may reduce  $\{-10.8\}$  dislocation emission probability, thus favoring  $\{10.-2\}$  dislocations with a higher resolved normal stress (Figure 5-28).

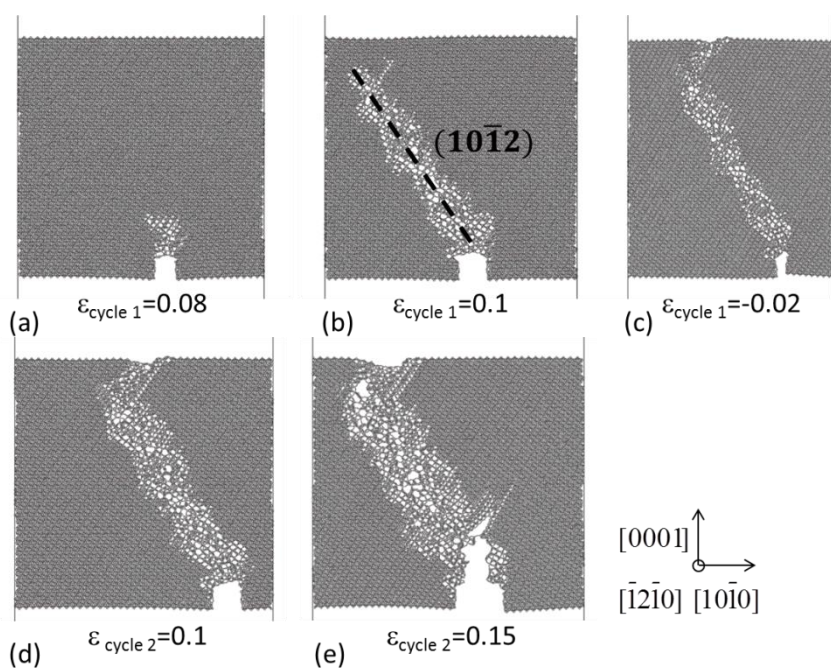


Figure 5-26. [10.0] strained  $\alpha\text{-Al}_2\text{O}_3$  slab ( $152.3 \times 4.9 \times 152.5 \text{ \AA}$ ) at 300K; configuration snapshots.

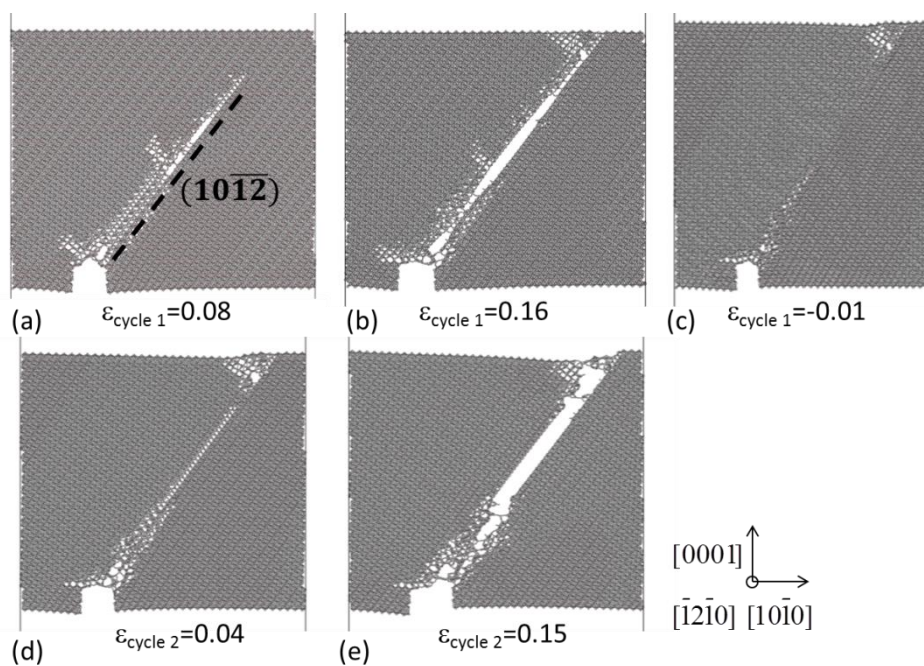


Figure 5-27. [10.0] strained  $\alpha\text{-Al}_2\text{O}_3$  slab ( $152.3 \times 4.9 \times 152.5 \text{ \AA}$ ) at 0K,  $\epsilon_0=0.07$ ; configuration snapshots.

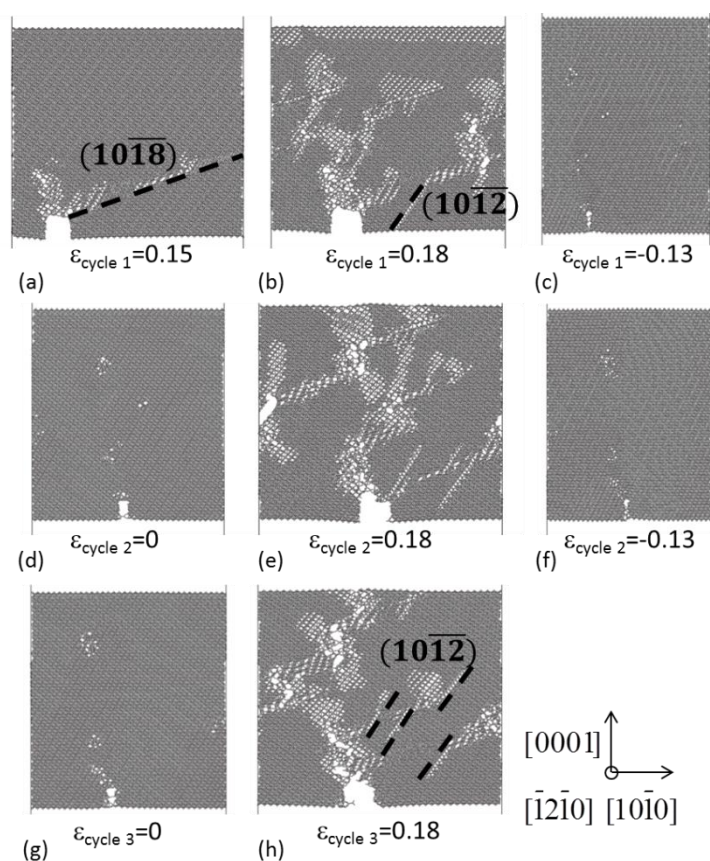


Figure 5-28. [10.0] strained  $\alpha$ -Al<sub>2</sub>O<sub>3</sub> slab (152.3x4.9x152.5 Å) at 0K,  $\epsilon_0=0.0$ ; configuration snapshots.

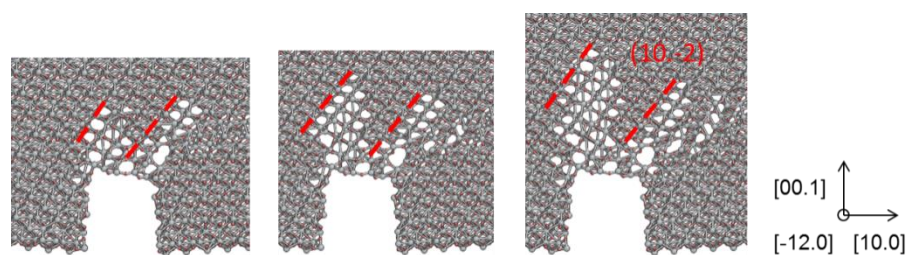


Figure 5-29. Suggested [10.0] strained  $\alpha$ -Al<sub>2</sub>O<sub>3</sub> slab {10.-2} slip facilitated amorphization mechanism.

The difference in crack distribution apparently correlates with the potential energy and stress responses after yielding, which indicate a gradual discontinuous reduction for the volume minimized static structure and a sharp drop for the other two structures. The volume distributed pre-cracks in the volume minimized static structure grow by void coalescence (Figure 5-28), which is in agreement with

experimental observations from fatigue studies of alumina coatings [133]. The crack healing, which was observed for this structure (Figure 5-28), reproduces earlier DFT based results [134]. According to these, such crack healing can be expected for structures with zero or negative pre-strain levels [134], which explains the negligible amount of healing for the pre-expanded structure (Figure 5-27). Subsequently, it was concluded that processing technologies which favor compressive residual stress formation, hence a reduced stress triaxiality, would be recommendable for large polycrystalline or single crystal  $\alpha$ -Al<sub>2</sub>O<sub>3</sub> structures under cyclic loading.

### 5.5.3 Summary

- Finite temperature and strain rate result in lower failure strains as compared to relaxation calculations, however low strength ductility with kinematic strain hardening may be possible.
- Positive pre-straining results in increased triaxiality, which significantly reduces crack healing probability, due to single crack propagation.
- Volume minimization results in multiple branching and/or amorphous band formation, which facilitates crack healing and shakedown possibility.
- Amorphization ahead of propagating cracks may occur due to multiple dislocation mechanism as a barrier-less phase transition, both at static and finite temperature conditions.

## 5.6 $\alpha$ -Al<sub>2</sub>O<sub>3</sub> stress corrosion study

### 5.6.1 Structures

For this study a (00.1) slab structure of thickness 152.5 Å, periodic dimensions 152.3x4.9 Å ([10.0]/[-12.0]) and a rectangular [00.1](10.0) surface notch was simulated.

The corrosive environment was created by adding 3456 water molecules at an initial density of 1.0 kg/l. For comparison and evaluation of liquid phase pressure effects a system with 4608 Ne atoms at a

density of 1.1 kg/l and the same slab structure without fluid phase were simulated. The choice of the particular noble gas species was based on its molecular weight, which was closest to that of water molecules. The density of Ne atoms was set so that its pressure would be identical to the water pressure at the given density.

### 5.6.2 Method

The structures were simulated at 300K using the NVT/NPT ensemble, the volume being fixed in the applied tension direction. The set pressures were 5000 and 0 atm for the systems with and without fluid phase, respectively. The pressure damping constant of 1000 fs and temperature damping constant of 100fs were used. The fluid phase containing structure pressure was set according to test simulation results for pure water systems at 1.0 kg/l. For ensemble effect comparison the slab structure in vacuum with constant volume-energy (NVE or microcanonical) ensemble was additionally simulated. The boundary conditions correspond to plane stress conditions due to the constant pressure setting in [-12.0] direction, except for the NVE simulation, which partially corresponds to plane strain conditions. In order to define conditions that would mimic the effect of plane strain in [00.1] direction, an additional constraint of zero [10.0] direction displacement in a 2 Å layer cross-section perpendicularly to the loading direction was imposed at a maximum distance from the crack.

The deformation rate of  $5e-6 \text{ fs}^{-1}$  in [10.0] direction with 5% increments and variable relaxation periods was applied. The simulations were run until complete rupture of the vacuum and Ne environment slabs. The water environment simulation was terminated at identical total simulation length.

### 5.6.3 Results and Analysis

The stress distribution snapshots for all systems indicate that the size effect, as discussed in section 5.3.3, is not prevalent, since loading induced stress concentration regions can be readily identified and the amorphization occurs in localized regions, which occupy a small fraction of the total volume.

The all systems observed failure mode initiates with amorphization and void assisted brittle crack propagation in (10.0) plane (Figure 5-30, Figure 5-31), indicated by a sharp decrease in potential energy and stress values (Figure 5-32). The observed failure behavior is qualitatively similar to experimentally and computationally observed void assisted plasticity failure in oxide shells of Al nanowires [174]. The occurrence of amorphous bands is interpreted, along the lines of discussion in section 5.2.1.2, as distorted lower density phase fragments, which may initiate fracture due to their lower strength values [149]. For the system with water, the brittle cleavage is followed by transition to dislocation facilitated slip failure along a  $\{-10.4\}$  plane, which is an experimentally observed cleavage plane [20] (Figure 5-31a). For the rest of systems the cleavage in (10.0) propagates until complete separation.

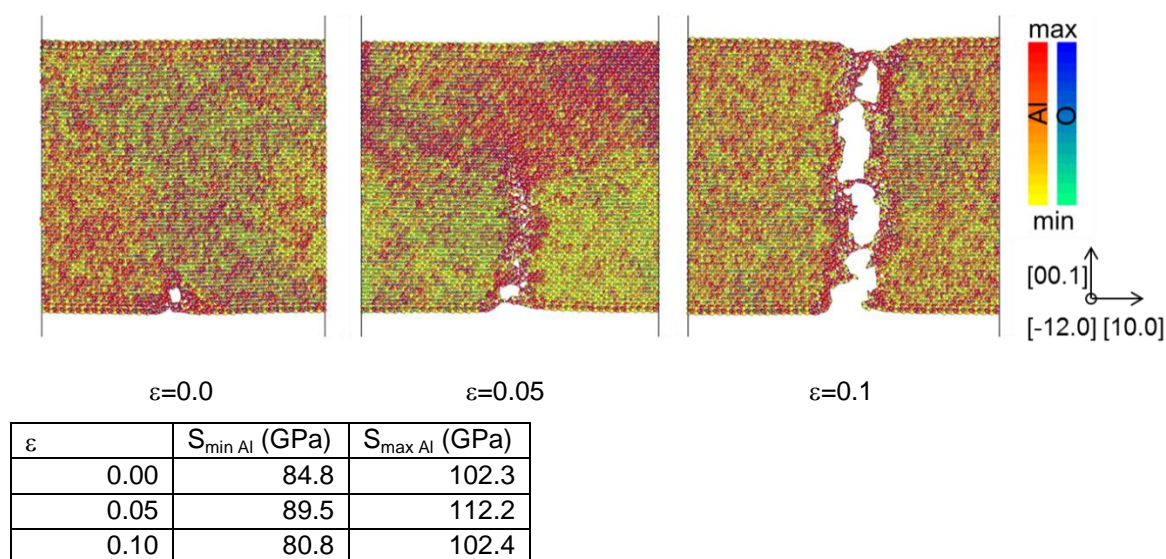
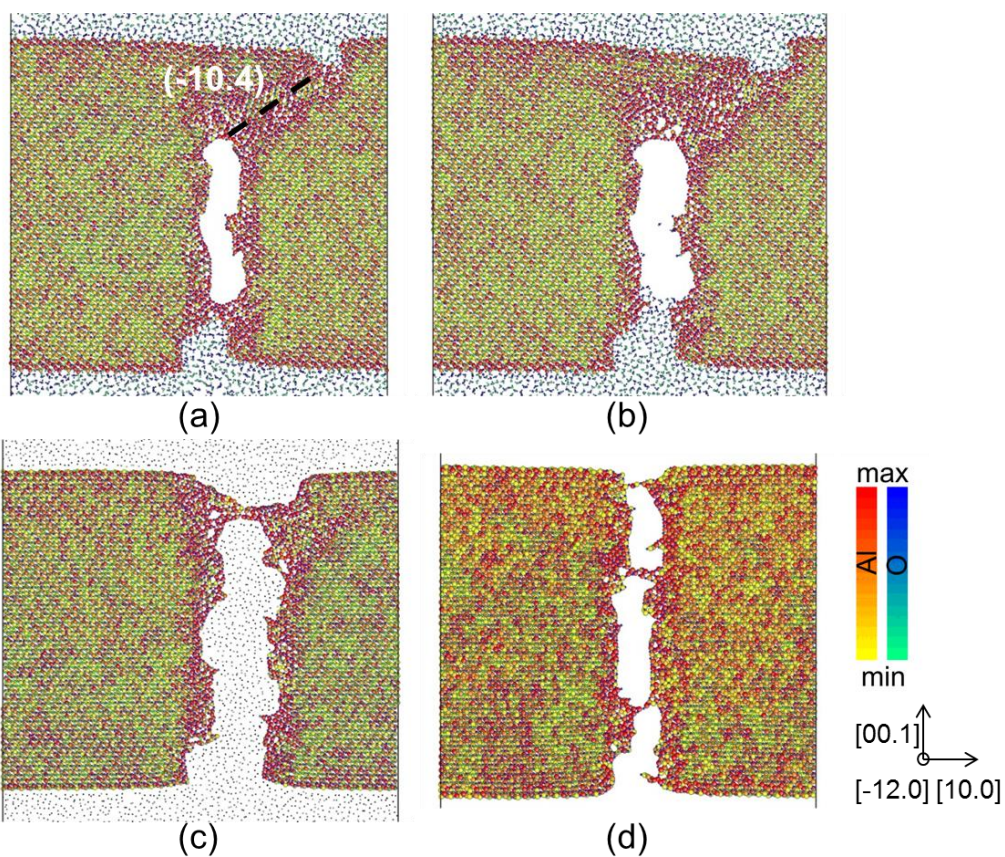


Figure 5-30. Vacuum placed  $\alpha$ - $\text{Al}_2\text{O}_3$  slab ( $152.3 \times 4.9 \times 152.5 \text{ \AA}$ ) [10.0] stretching snapshots: max. normal stress distribution.



configuration	$\varepsilon$	$S_{\min \text{ Al}}$ (GPa)	$S_{\max \text{ Al}}$ (GPa)
a	0.10	47.9	72.7
b	0.15	47.5	73.1
c	0.20	47.2	71.2
d	0.10	83.0	104.4

Figure 5-31.  $\text{H}_2\text{O}$  (a,b), Ne (c) and NVE/vacuum environment placed (d)  $\alpha\text{-Al}_2\text{O}_3$  slab ( $152.3 \times 4.9 \times 152.5 \text{ \AA}$ ) [10.0] stretching snapshots: max. normal stress distribution.

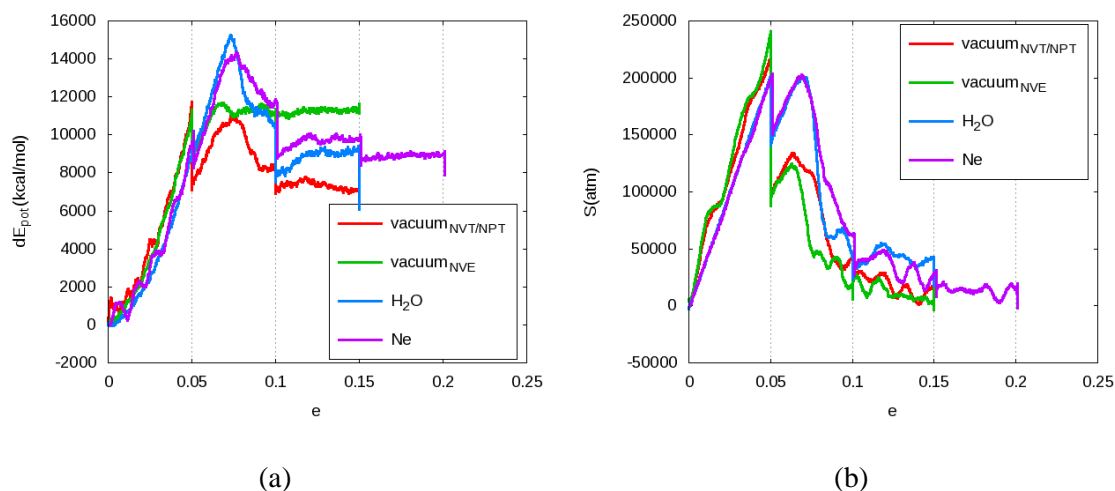


Figure 5-32. Potential energy (a) and tensile stress (b) vs. strain for [10.0] strained  $\alpha$ - $\text{Al}_2\text{O}_3$  slab: environment species/ensemble comparison.

The mean atomic octahedral and maximum principal stress  $\sigma_{\text{oct}}$  and  $\sigma_{\text{max}}$  values (Figure 5-33) allow for conclusion that the local shear deformation is the dominant failure mechanism, since, after the initial stress curve peak due to brittle fracture,  $\sigma_{\text{oct}}$  stays at a constant lower maximum value, whereas  $\sigma_{\text{max}}$  keeps decreasing stepwise until failure. For the NVE ensemble system the  $\sigma_{\text{oct}}$  indicates stiffening in contrast to the rest of systems. Yet the similarity of overall tensile stress  $\sigma_x$  and the  $\sigma_{\text{max}}$  responses indicates a macroscopically brittle failure mode. Thus the constant  $\sigma_{\text{oct}}$  levels are attributed to occurrence of residual stresses. The assumption is confirmed by the atomic  $\sigma_{\text{max}}$  distribution plots (Figure 5-30, Figure 5-31), which indicate distinct stress concentration in loaded parts of the structure in loaded state and geometric discontinuity regions prior to loading. After the failure of the structure the stresses are concentrated around the fracture surfaces, which is attributed to residual stresses, as indicated by the non-zero mean  $\sigma_{\text{oct}}$  and  $\sigma_{\text{max}}$  values after failure (Figure 5-33), except for  $\sigma_{\text{max}}$  of the NVE system.

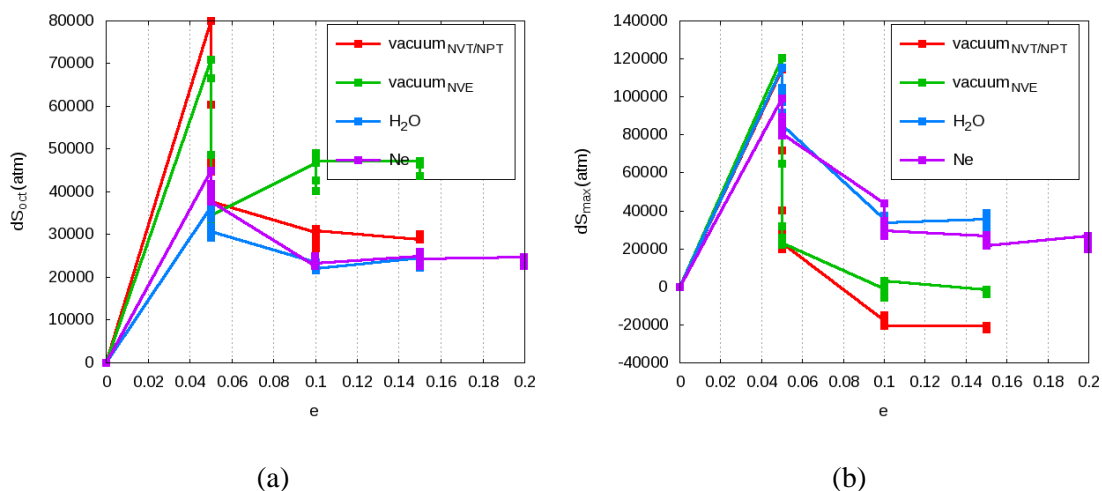


Figure 5-33. Mean atomic octahedral (a) and max. normal (b) stress vs. strain for [10.0] strained  $\alpha$ -Al<sub>2</sub>O<sub>3</sub> slab: environment species/ensemble comparison.

The fluid environment effects on failure behavior can be estimated by observing significantly higher peak  $\sigma_{oct}$  values and higher  $\sigma_{max}$  reductions after yielding for structures in vacuum, as well as higher yield and failure values for potential energy, except for the NVE system, and  $\sigma_{max}$  failure values for structures in fluid. However, the failure values for  $\sigma_{oct}$ , except for the NVE system, and the  $\sigma_x$  have similar values, as expected. These observations allow for the conclusion that pressurized fluid environment enhances energy capacity and plasticity of the structures, as confirmed by estimated significantly larger failure strain values (Figure 5-32b). These effects are being ascribed to hydrostatic pressure induced compression stress state of reduced stress triaxiality, which, in combination with resolved shear loading, may facilitate shear/dislocation based failure mechanisms in  $\alpha$ -Al<sub>2</sub>O<sub>3</sub> [29, 175, 176], and, in the water case, to stress softening of the slab surfaces due to formation of low stiffness Al hydroxide layer ( $K=50$  GPa [177]), as suggested by the occurrence of slip failure as crack tip approaches the second outer surface.

The differences between the NVE and NPT systems include the  $\sigma_{oct}$  stiffening after initiation of fracture and no reduction in potential energy after yielding. These are related to enhanced plasticity [21] of the material due to the increase in temperature up to about 425K after an initial exothermic reduction of about 10K during the elastic expansion. The failure strain identity with vacuum system could be

explained by simultaneous reduction of elastic moduli of the material [178] and thermodynamic melting [143] due to increasing overall and local temperatures, both of which reduce the strength of the material.

For the water containing system the amount of OH group vs. time indicates that the water/ $\text{Al}_2\text{O}_3$  reaction rate is close to linear at each constant strain level, which in combination with a constant level of physisorbed  $\text{H}_2\text{O}$  suggests that the reaction rate is limited by the water diffusion rate (Figure 5-34). The comparatively small number of physisorbed water molecules and  $\text{Al}(\text{OH})_2$  groups, which correspond to potential gas phase species, are in agreement with the finding that hydroxylation energies are always greater than the hydration energies [123]. The dominance of estimated  $\text{O}_{\text{surface}}\text{H}$  vs.  $\text{O}_{\text{adsorbed}}\text{H}$  groups is in qualitative agreement with ab initio simulation predictions at high OH coverages [124]. Although the total potential energy and loading stress plots at each relaxation stage indicate local equilibrium, from the non-equilibrium states of the slab potential energy and reaction species levels and the slow capillary water diffusion after opening of the internally formed void at  $\varepsilon=0.15$  it is evident that a significantly higher time scale is required to obtain quasi static crack propagation. This motivated exploring extended time scale/steady state methods, which are considered in section 5.7.

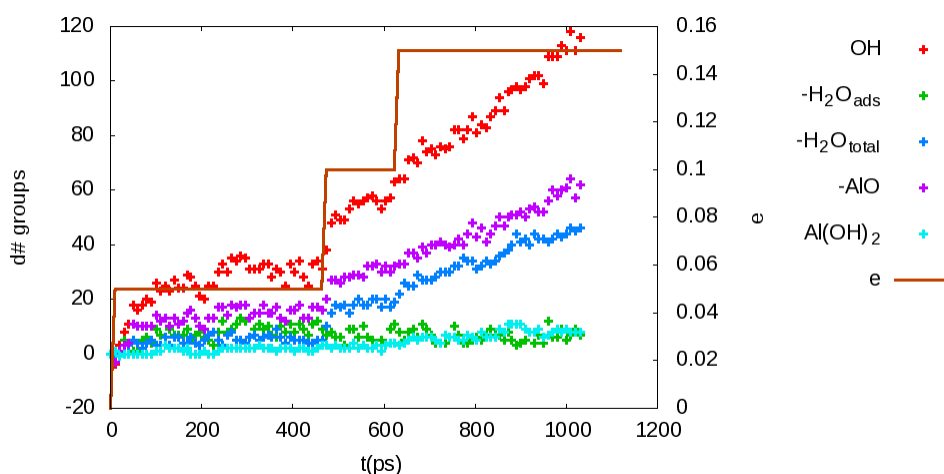


Figure 5-34. Number of atom groups vs. time for  $\text{H}_2\text{O}$  environment placed  $[10.0]$  strained  $\alpha\text{-Al}_2\text{O}_3$  slab.

It should be also noted that the plastic failure mechanisms observed above can be influenced by the quasi 2-dimensional (2D) definition of the structure due to the small value of its  $[-12.0]$  dimension. In

particular, the spacing of dislocations along the crack front is increased artificially, compared to a 3D structure [179, 180]. Moreover, artificial dislocation jogs may occur for dislocation lines that are not parallel to the z-axis direction [180]. Likewise, brittle crack propagation is limited to planes that are perpendicular to the periodic initial defect cross-section plane or artificial steps in planes not perpendicular to the initial defect cross-section plane.

#### **5.6.4 Summary**

- Hydrostatic pressure in Ne/H<sub>2</sub>O containing systems has been found to enhance localized ductility at crack tip compared to structures in vacuum.
- A change of fracture plane during crack propagation in the H<sub>2</sub>O containing system indicates a potential corrosion effect of mechanically weakened/embrittled hydroxylated slab surface.
- Corrosion effects for further crack propagation in pressured water system are limited by water diffusivity. Correspondingly, creep type failure is predicted.

#### **5.7 Extended time scale/steady state $\alpha$ -Al<sub>2</sub>O<sub>3</sub> study**

Motivated by the results of loading rate comparison (section 5.4) and stress corrosion (section 5.6) studies, which indicate the computationally available limits and the importance of considering the time dependent effects, selected extended time scale methods were applied for estimating the steady state of the studied systems.

## 5.7.1 Extended time scale crack propagation

### 5.7.1.1 Method

For the study of crack propagation in  $33.8 \times 4.88 \text{ \AA}$  ( $[10.0]/[-12.0]$ ) periodic and  $101.7 \text{ \AA}$  thick slab with  $[00.1](10.0)$  rectangular notch and  $(00.1)$  open surface the parallel replica dynamics (PRD) method with 10 replicas was used [181]. The method is defined as the original dynamics preserving MD simulation time scaling proportionally to the number of independent replicas of a system, which are run in parallel under certain conditions. The conditions according to the mathematical formalization [182] are that

- a quasi-static distribution (QSD) of independent and identically distributed states can be reached during a dephasing stage of the replicas, run prior to the parallel run;
- no new rare event occurs within a given correlation time interval, which is seen as an approximation of the time to reach the QSD after a rare event occurs during a parallel run.

The choice of the method was based on the assumption that crack propagation in the static loading limit may be considered as a sequence of rare events, signaled by change in atom connectivity. The particular event criterion has been applied successfully in low temperature pyrolysis [183], which motivated evaluating its applicability for crack propagation.

For the current application, the event distribution peak value based threshold value of 4 was used (Figure 5-35). The velocity autocorrelation (VAC) function transition time (0.3 ps) was assumed as an empirical estimate for the minimum correlation time. PRD specific parameters, as described in [12], include event checking frequency of 20 fs and de-phasing and correlation time periods of 3 ps (based on VAC time estimate). The slab was pre-strained at  $d\varepsilon/dt=5e-7 \text{ fs}^{-1}$  up to 9% in  $[10.0]$  direction. For all simulation phases the NVT/NPT ensemble, corresponding to plane stress conditions, was used at 300K and 0 atm in  $[-12.0]$  direction with temperature damping of 100 fs, pressure damping 1000 ps and 2 thermostat chain on the barostat.

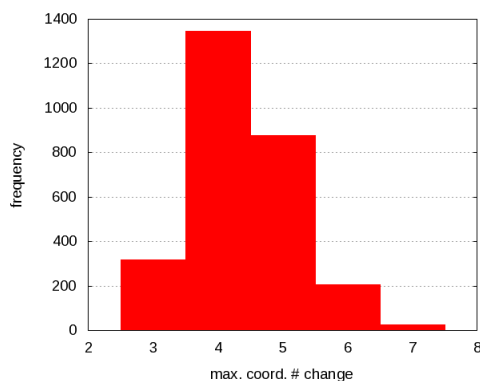


Figure 5-35. Bond breaking event distribution for [10.0] strained  $\alpha$ -Al<sub>2</sub>O<sub>3</sub> slab.

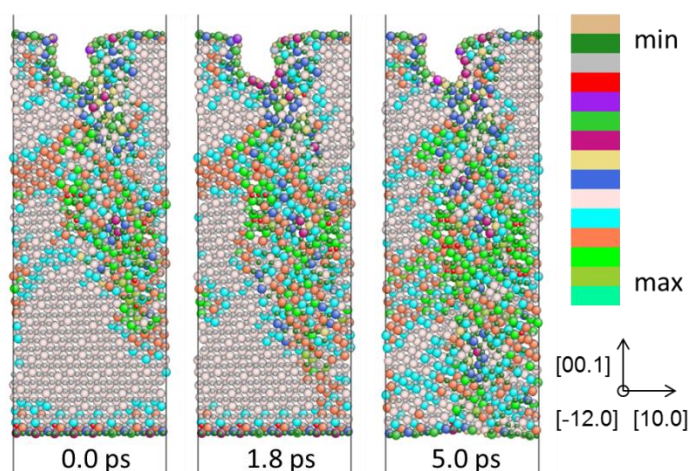
### 5.7.1.2 Results and Discussion

The parallel replica time statistics (Table 5-6) indicate simulation time scaling, defined as clock time/simulation time, of about 7, whereas the 6 coincident replicas for the 2<sup>nd</sup> crack propagation event imply that a higher threshold or longer correlation/de-phasing times could be used. The lack of propagation events and the steady state according to the potential energy and stress curves for about 0.1 ns of the scaled simulation time after the 2<sup>nd</sup> event were assumed to be sufficient for concluding that new event probability was negligible.

Table 5-6. Parallel replica dynamics event statistics for [10.0] strained  $\alpha$ -Al<sub>2</sub>O<sub>3</sub> slab.

Event #	Correlated	Coincident	Clock (ps)	Simulation time (ps)
0	0	0	0.0	0
1	0	1	1.8	0.18
2	0	6	5.0	3.2
-	-	-	109.3	16.3

The coordination number distribution (Figure 5-36) indicates propagation of an amorphous lower density band through the slab thickness. The qualitative similarity with earlier results with identical structures (Figure 5-14), along with absence of new events after 0.1 ns of clock time, allow for conclusion that the previously used loading rate settings for structures in vacuum (sections 5.3-5.6) were sufficient for comparison with experimental loading rates.

Figure 5-36. Coordination number (max=19, min=2) distribution for [10.0] strained  $\alpha$ -Al<sub>2</sub>O<sub>3</sub> slab (33.8x4.88x101.7 Å).

The obtained results suggest that connectivity based PRD is a viable approach for significantly reducing computation time in incremental low strain rate vacuum environment crack simulations. For maximizing the effectiveness of the method particular care has to be taken for selecting the correlation/de-phasing times and threshold values using test simulations similar to the one described above. A suggested modification for the particular application would be implementation of continuous

strain rate regime during the PRD runs instead of the incremental pre-straining approach used presently, which would, however, require re-interpretation of the time and associated strain rate scaling.

## 5.7.2 Steady state stress corrosion study

### 5.7.2.1 Method

A grand canonical Monte Carlo method (GC MC) [13] was chosen for testing its applicability for steady state stress corrosion simulations due to slow water diffusion process in narrow crack confinement (section 5.6.3). The method has been previously implemented in combination with MD simulations for studies of SiO<sub>2</sub> surface interactions with hypersonic flows [184] and oxygen chemisorption on platinum (111) surface [185]. For the study the hybrid GCMC/MD approach, originally implemented for assessment of the thermodynamic stability of oxide formations [186], was applied<sup>4</sup>. It combines alternate GCMC and MD runs of arbitrary equilibrium based setting. The GCMC runs include structure energy minimization prior to the move acceptance probability calculations. Since this imposes a bias in the MC algorithm, an accessible volume calculation approach has been used as a means for eliminating the bias effect [186, 187].

For the current study a 33.8x4.88 Å ([10.0/[-12.0]]) periodic and 50.85 Å thick slab with a [00.1](10.0) rectangular notch and (00.1) open surface with an initial non-periodic dimension of 60 Å was used. The vacuum regions of the periodic box were set to be filled with H<sub>2</sub>O molecules according to the GCMC specific molecule placement/removal/displacement moves. The GCMC specific settings include 1000 step initial equilibration, followed by a 430 step and subsequent 300 step runs (additionally 200 step runs for convergence comparison) alternating with MD runs. Van der Waals radius of Al atom has been used as the minimum molecule placement radius. The constant potential-volume-temperature (μVT)

---

<sup>4</sup> Credit to group member T. Senftle.

ensemble at 300K and a [188] published chemical potential estimate for water at 4000 atm pressure was used. The MD simulations were performed with NVT ensemble using temperature damping of 100 fs. Due to the relatively small [00.1] dimension, the given boundary conditions are considered as plane stress conditions. During each run the slab was stretched in [10.0] direction at  $d\varepsilon/dt=5e-6 \text{ fs}^{-1}$  by 1% (2 ps). System volume preservation was imposed by simultaneously reducing the [00.1] dimension.

### 5.7.2.2 Results and Discussion

The reduction in the slope accepted water molecule displacements despite preservation of the slope of the total number of water molecules (Figure 5-39) and increase in the slope of relative energy (Figure 5-37a, defined as  $E_{\text{Reax-nH}_2\text{O}}/\mu$ ) after ~2200 iterations suggest that a saturation in water density may coincide with tension related elastic straining of the slab structure. Subsequently, the convergence of the total number of water molecules along with potential energy were assumed as sufficient conditions for water molecule displacement move convergence at each volume increment. Thus the applicability of the method was estimated by the convergence behavior with respect to energy and the total number of water molecules in the system at each strain increment (Figure 5-37) and between the 200 and 300 step incremental runs (Figure 5-38). These allow for the conclusion that the method is a viable tool for obtaining steady state structures of low diffusivity systems (Figure 5-31b, Figure 5-40), provided that appropriate GCMC incremental run lengths and MD deformation rates are chosen. Yet it should be noted that details of the reaction mechanisms occurring during the transition processes would not be available from the MCGC runs, which highlights the significance of the intermediate MD runs.

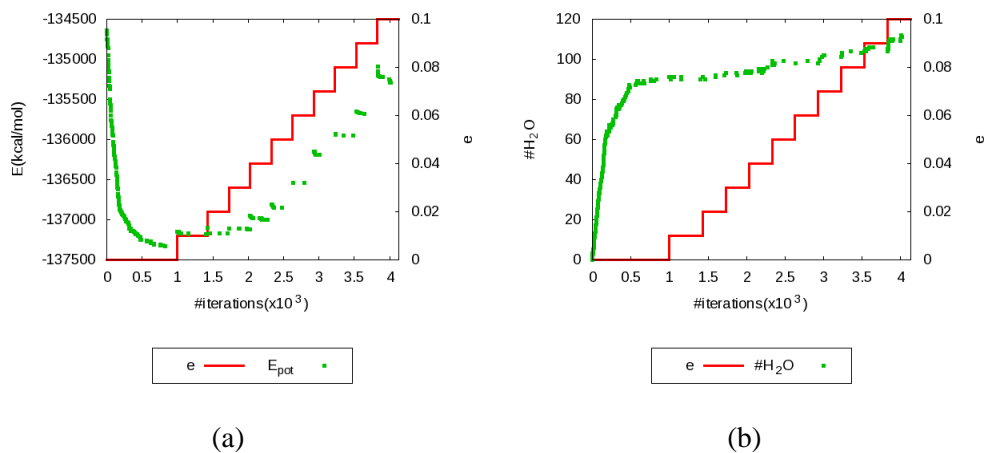


Figure 5-37. Relative energy (a) and number of H<sub>2</sub>O molecules (b) vs. iterations for GCMC/MD [10.0] strained  $\alpha$ -Al<sub>2</sub>O<sub>3</sub> slab.

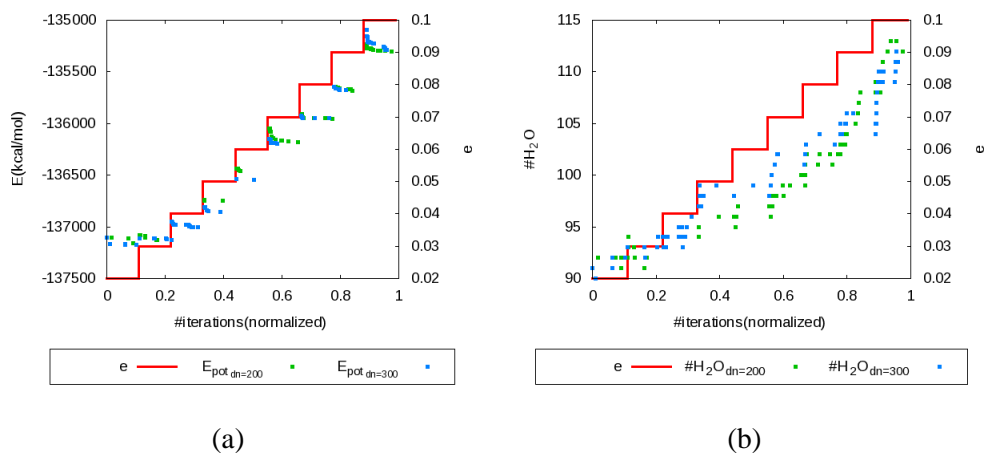


Figure 5-38. Relative energy (a) and number of H<sub>2</sub>O molecules (b) vs. iterations for GCMC/MD [10.0] strained  $\alpha$ -Al<sub>2</sub>O<sub>3</sub> slab: comparison of incremental runs with different numbers of iterations.

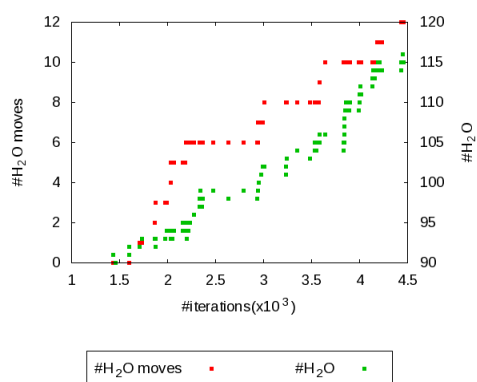


Figure 5-39. Numbers of H<sub>2</sub>O molecule displacement moves and total number of H<sub>2</sub>O molecules vs. iterations for GCMC/MD [10.0] strained  $\alpha$ -Al<sub>2</sub>O<sub>3</sub> slab.

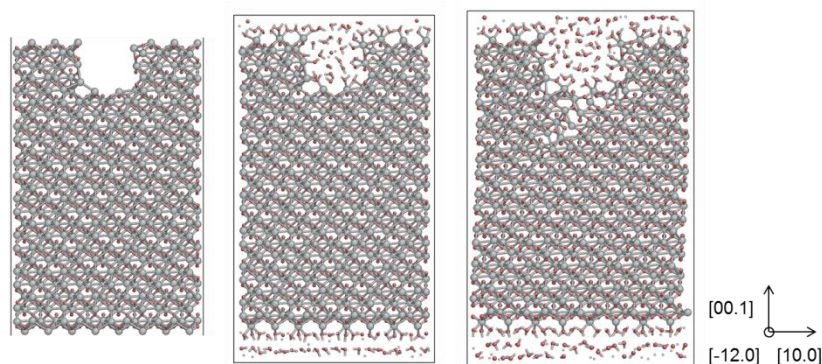


Figure 5-40. GCMC/MD [10.0] strained  $\alpha$ -Al<sub>2</sub>O<sub>3</sub> slab (33.8x4.88x50.9 Å) configuration snapshots (Al – grey, O – red, H – white).

## 5.8 fcc-Ni stress corrosion study

### 5.8.1 Structures and Method

For the study a {111} slab with periodic dimensions of 29.8x8.6 Å ([1-10]/[11-2]), thickness of 30.4 Å and an elliptical 3 layers wide [111](11-2) notch was simulated. 256 H<sub>2</sub>O molecules at an initial density of 1.0 kg/l were added for the corrosive environment simulation. NVT/NPT ensemble at 300K with 100 fs damping and 4000 atm with 5000 fs damping and 2 chain thermostats on barostat was used. Due to the relatively small [111] dimension, the given boundary conditions are considered as plane stress conditions in [111] direction. In contrast, plane strain conditions are considered in [11-2] direction, which was kept fixed at its value after equilibration for all systems except for one. For the latter system a constant pressure boundary condition was applied in [11-2] direction for comparison. A loading regime of  $5e-6 \text{ fs}^{-1}$  0.25% (0.5 ps) [1-10] direction strain increments alternating with 5 ps relaxation periods was applied. For temperature effects estimation an additional simulation with H<sub>2</sub>O molecules at 600K was performed. A cutoff radius of 10 Å and simulation time increments of 20 ps were used for the atomic strain calculation.

## 5.8.2 Results and Discussion

It was observed that during early stage of equilibration of the slab structure in vacuum the notch would heal itself by rearrangement to a single layer step (Figure 5-41). Therefore it was decided to simulate additionally a slab structure in vacuum with a pre-oxidized notch in order to prevent the closure.

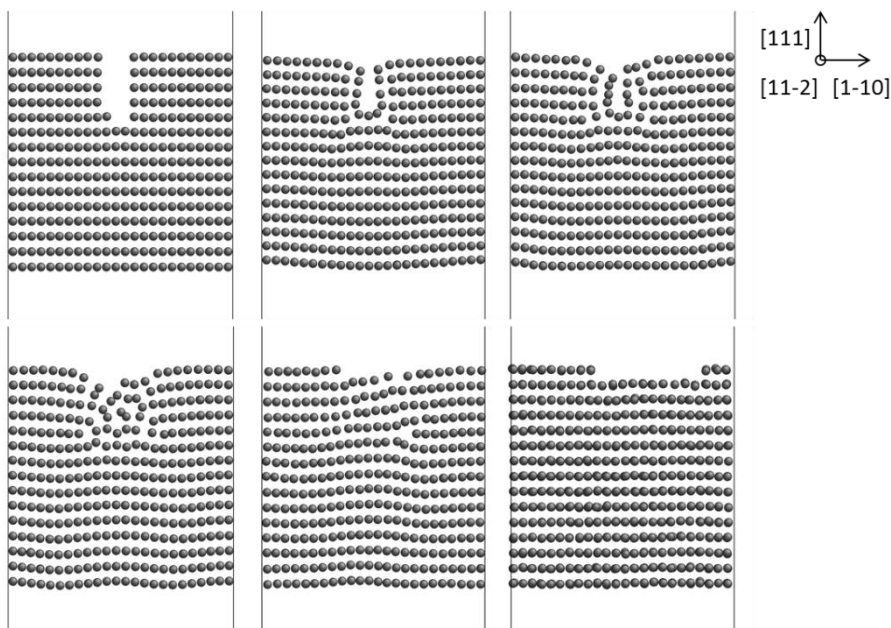


Figure 5-41. Equilibration of fcc-Ni slab ( $29.8 \times 8.6 \times 30.4$  Å) in vacuum (300K, 0 atm); configuration snapshots.

For the constant [11-2] pressure system multiple symmetric tilt grain formation events, as well as a temporary transition to the [100]/[010]/[001] lattice orientation (Figure 5-42) were observed. Furthermore, the octahedral atomic strain distribution is found to be fairly uniform with respect to distance from the surfaces, which is attributed to small surface relaxation in an fcc metal as compared to a metal oxide [103] (Figure 5-43). Instead, the strain is concentrated in grains as they are being formed. Similarly, the octahedral stress distribution is found to be uniform across the grain bulk, having stress concentration in 1-2 surface layers and along grain boundaries (Figure 5-44).

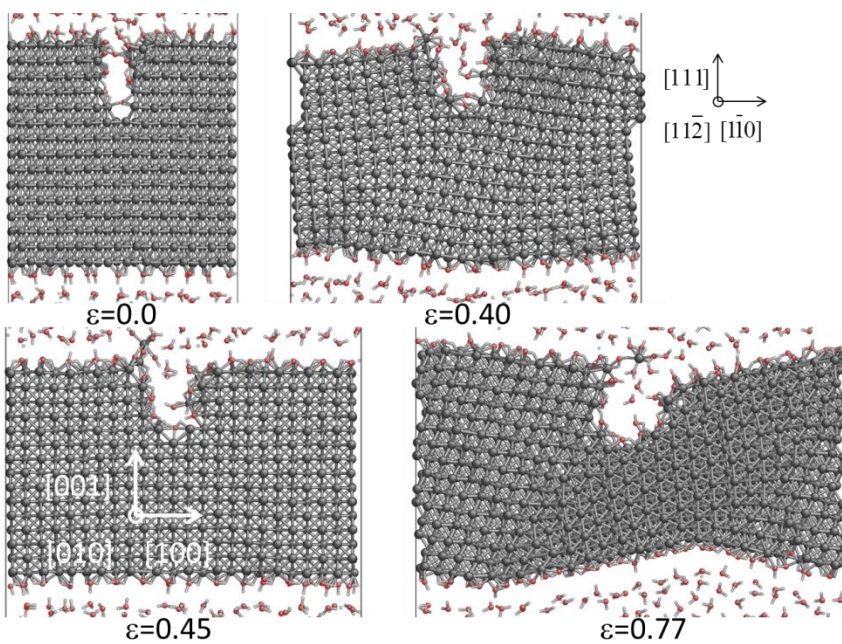
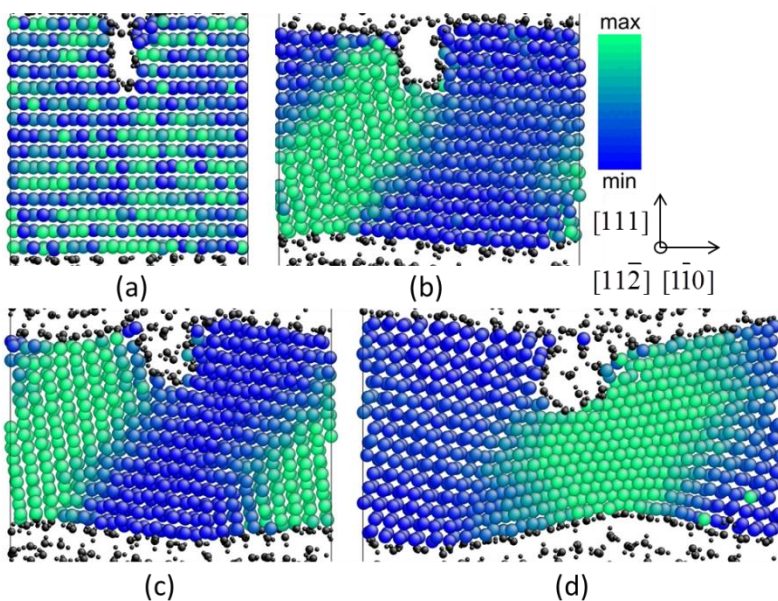
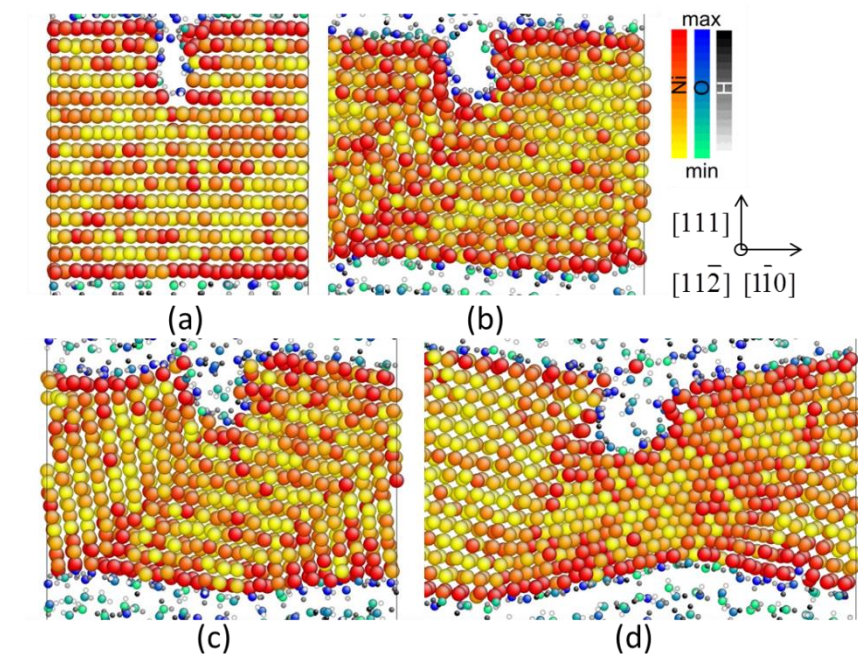


Figure 5-42. [1-10] strained fcc-Ni slab ( $29.8 \times 8.6 \times 30.4 \text{ \AA}$ ) in water (300K,  $P_{[11-2]} = \text{const}$ ); configuration snapshots (Ni – black, O – red, H – white).



configuration	$\varepsilon$	$E_{\min}$	$E_{\max}$
a	0.00	0.10	0.23
b	0.27	0.48	0.64
c	0.39	0.53	0.81
d	0.76	0.43	0.96

Figure 5-43. [1-10] strained fcc-Ni slab ( $29.8 \times 8.6 \times 30.4 \text{ \AA}$ ) in water (300K,  $P_{[11-2]} = \text{const}$ ); octahedral Almansi strain distribution.



configuration	$\varepsilon$	$S_{\min \text{ Ni}}$ (GPa)	$S_{\max \text{ Ni}}$ (GPa)
a	0.00	7.6	19.3
b	0.27	8.9	23.6
c	0.36	10.7	25.2
d	0.76	9.5	24.8

Figure 5-44. [1-10] strained fcc-Ni slab ( $29.8 \times 8.6 \times 30.4 \text{ \AA}$ ) in water (300K,  $P_{[11-2]} = \text{const}$ ); octahedral stress distribution.

In contrast, no grain formation or lattice re-orientation was observed in the fixed [11-2] dimension systems (Figure 5-51). Subsequently, a significantly lower failure strain ( $\sim 0.6$  vs.  $> 0.8$  according to Figure 5-45b and Figure 5-42) is predicted for the latter, which is expected due to the increased stress triaxiality [189]. The observation is supported by comparatively low yielding stress and strain energy capacity of the constant [11-2] pressure system (Figure 5-45). Complementarily, it is suggested that partially the large differences may be related to the underestimated ISF of fcc-Ni (section 5.2.2.2).

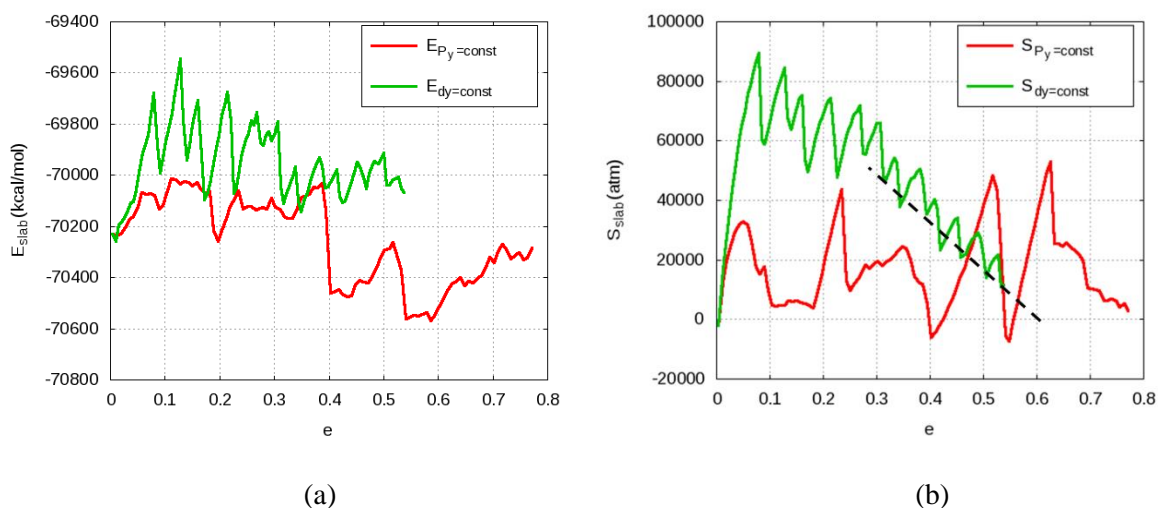


Figure 5-45. Potential energy (a) and tensile stress (b) vs. strain for [1-10] strained fcc-Ni slab in water: boundary condition comparison.

The effects of  $H_2O$  environment can be estimated by considering the potential energy responses (Figure 5-46a), which indicate that the constantly hydroxylated Ni surfaces nucleate dislocations with lower energy barriers than the structures in vacuum, in contrast to static QM-CADD calculations with a single O adatom [101]. This results in a lower failure strain than for the structures in vacuum. Yet it is also observed that the pre-oxidized structure yields significantly higher dislocation emission barriers for the second and third emissions than the structure in vacuum. It is suggested that reduced triaxiality effect due to the water pressure could be attributed to the observed differences. Furthermore, since the pre-oxidized structures were equilibrated before applying the deformation, it is suggested that the reduction of dislocation barriers for the structures in water can be also ascribed to insufficient time for the formation of a stable surface film due to the applied strain rate. This would be consistent with the rupture-slip dissolution mechanism [104, 105], since rupture, as indicated by the increased initial dislocation emission barriers, is likely to occur with the pre-oxidized structures in vacuum, whereas dissolution and constant oxidation processes with low-barrier slip increments are applicable to the structures in water. The effects of elevated temperature at 600K can be distinguished most clearly by reduction in dislocation nucleation barriers after transition to the necking failure mechanism (Figure 5-46a), which occurs earlier

than for the analogous system at 300K. Likewise, the behavioral differences are manifested in the overall tensile stress responses (Figure 5-46b), which indicate the highest stiffness for the vacuum structure with closed notch, followed by the pre-oxidized notch structure in vacuum and the structures with H<sub>2</sub>O interface.

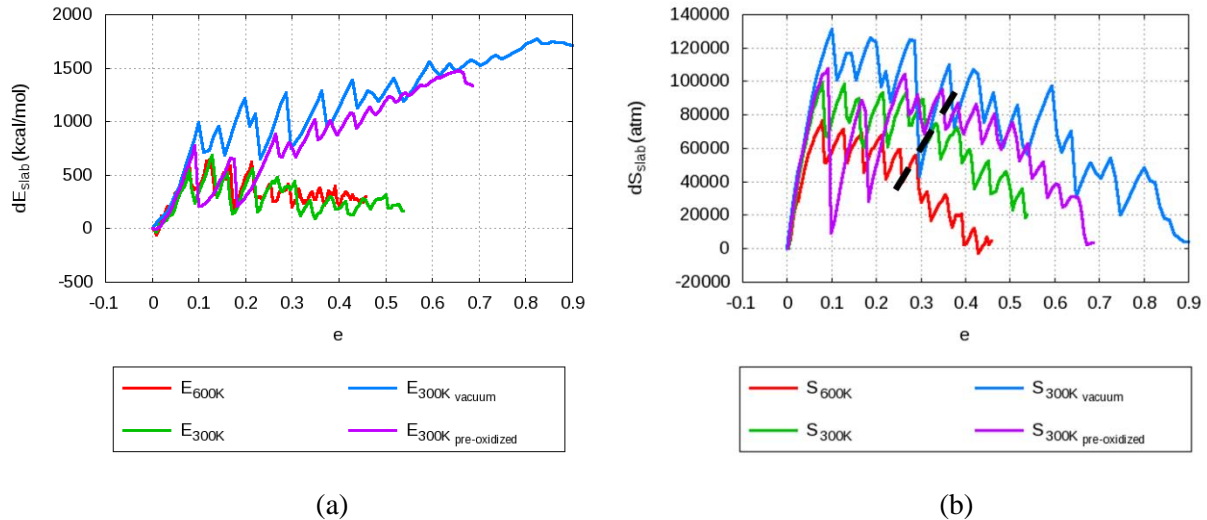


Figure 5-46. Potential energy (a) and tensile stress (b) vs. strain for [1-10] strained fcc-Ni slab: temperature and environment comparison.

Similarly to the quasi 2D assumptions explained in section 5.6.3, the observed  $\{113\}$  slip planes in the systems with fixed [11-2] dimension were considered as a 2D equivalent of the expected slip in  $\{111\}$  planes of an fcc metal [160, 163, 190, 191] (Figure 5-47). The quasi 2D constraints were also attributed to the observed step formation mechanism, facilitated by an expanded dislocation core (Figure 5-48). Since the potential energy change for the transition did not indicate any metastable transition state, no transient grain formation was assumed to be present (Figure 5-49). The single dislocation barriers could be readily identified by consecutive peaks in the potential energy and stress plots (Figure 5-46). Likewise, it was observed that for all structures that contain a notch there occurs a transition between two approximately constant peak stress slopes after symmetry preserving  $\{113\}$  dislocations start to nucleate, thus facilitating a necking type failure due to rising stress concentration (Figure 5-51a,c,d, Figure 5-50). Instead, for the structure with closed notch only single  $\{113\}$  plane dislocations and no necking transition

were observed (Figure 5-51b). Additionally it is suggested that a flaw tolerance related size effect, as discussed in section 5.3.3, may manifest in the single type dislocation/grain formation mechanisms observed in the study.

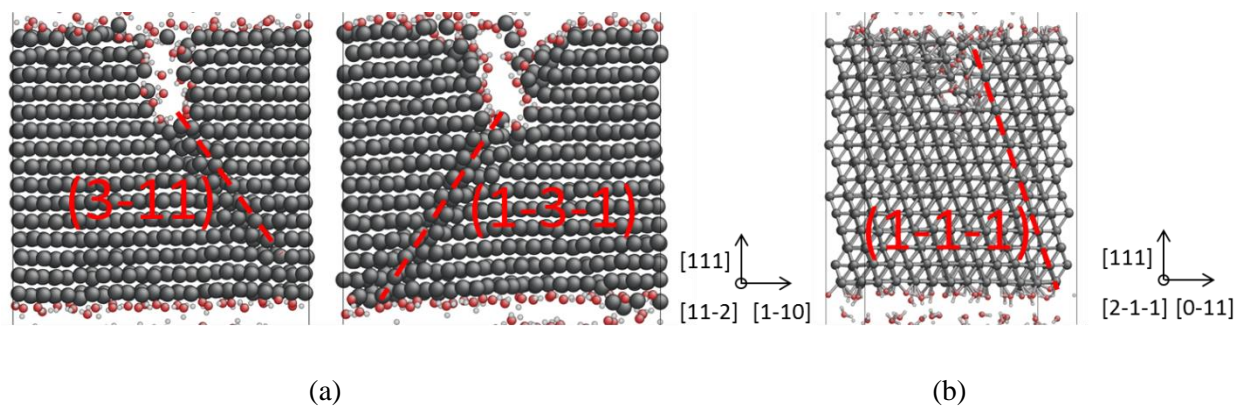


Figure 5-47. [1-10] strained fcc-Ni slab ( $29.8 \times 8.6 \times 30.4 \text{ \AA}$ ) in water (600K,  $dx_{[11-2]} = \text{const}$ ); dislocation planes.

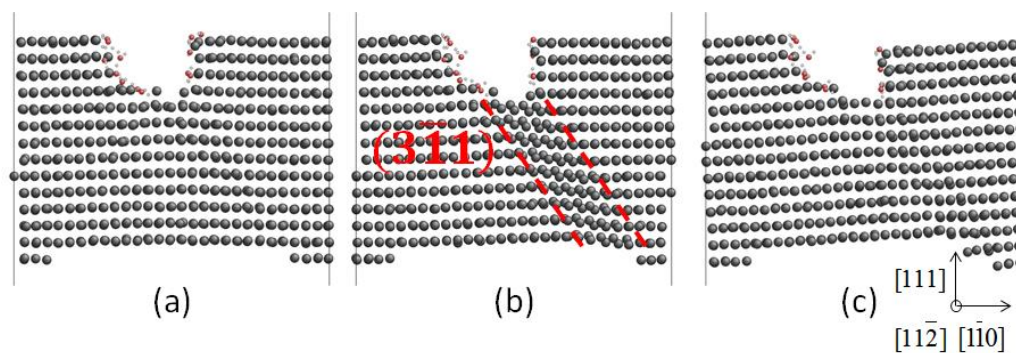


Figure 5-48. [1-10] strained pre-oxidized fcc-Ni slab ( $29.8 \times 8.6 \times 30.4 \text{ \AA}$ ) in vacuum (300K,  $dx_{[11-2]} = \text{const}$ ); step formation mechanism at  $\epsilon = 0.272$ .

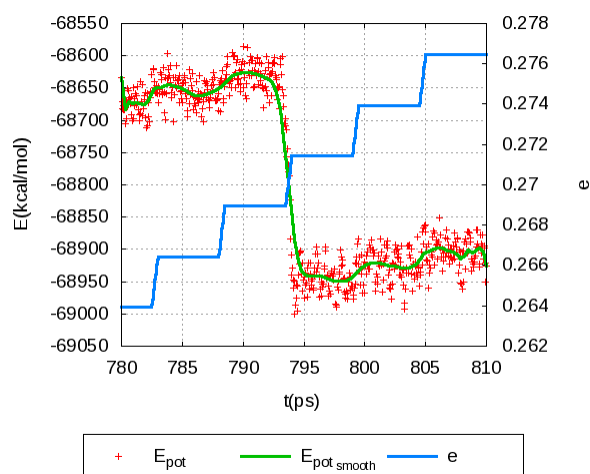
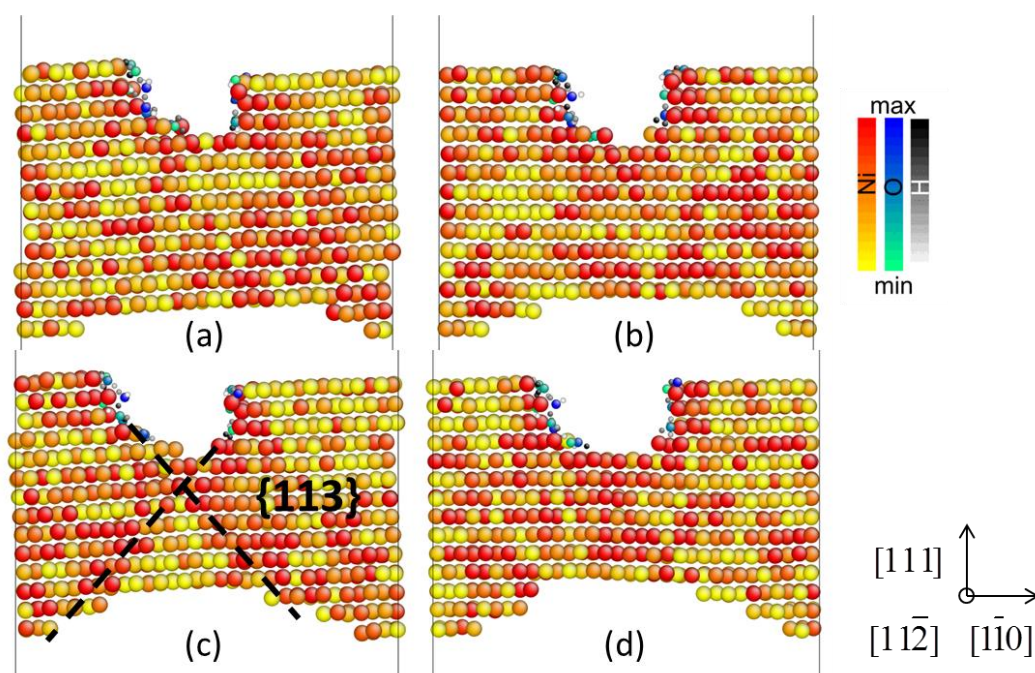


Figure 5-49. Potential energy and strain vs. time for [1-10] strained pre oxidized fcc-Ni slab (300K,  $dx_{[11-2]}=const$ ): step formation transition.



configuration	$\epsilon$	$S_{\min \text{ Ni}}$ (GPa)	$S_{\max \text{ Ni}}$ (GPa)
a	0.27	9.0	19.3
b	0.30	8.4	18.6
c	0.36	9.3	19.6
d	0.40	9.2	19.4

Figure 5-50. [1-10] strained pre-oxidized fcc-Ni slab ( $29.8 \times 8.6 \times 30.4 \text{ \AA}$ ) in vacuum (300K,  $dx_{[11-2]}=const$ ); neck formation; octahedral stress distribution.

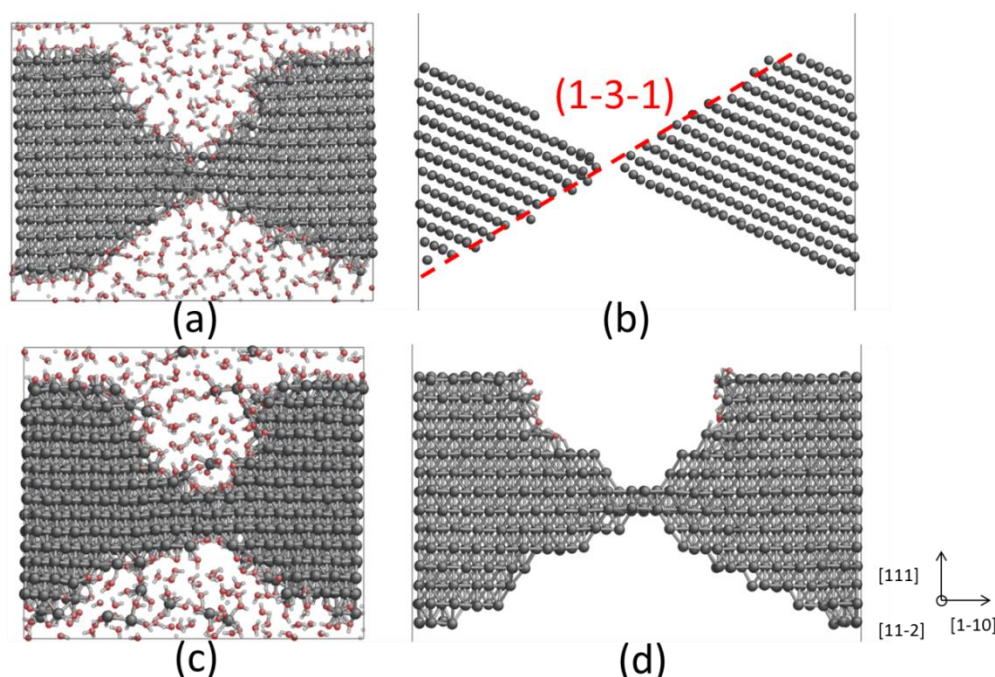


Figure 5-51. [1-10] strained fcc-Ni slab ( $29.8 \times 8.6 \times 30.4 \text{ \AA}$ ) failure comparison ( $dx_{[11-2]} = \text{const}$ ): structures in water at 300K (a) and 600K (c) and structures in vacuum without pre-oxidation (b) and with pre-oxidized notch (d) (Ni – black, O – red, H – white).

The only reaction product in the 300K simulations is Ni hydroxide, which is in marginal agreement with ab initio phase diagram of [109], but not with experimental data [192] (Figure 5-52a,b). However, the oxide formation at 600K is in agreement both with ab initio and experimental results [109, 192] (Figure 5-52c). Since no new oxide is formed during the deformation, it is suggested that longer time scales would be required for an OH dissociation reaction to occur. This could be attributed to higher activation energy and low endothermicity of the hydroxyl ion dissociation reaction with respect to nearest Ni (111) neighbor configuration, according to DFT calculations [193]. Interestingly, [109] also finds that the Ni {111}/H<sub>2</sub>O interface always activates H<sub>2</sub>O dissociation regardless of the applied electrochemical potential. Based on the reaction species dynamics (Figure 5-52a,b) it could be also concluded that the boundary condition effect was manifested in the lower rate of increase of physisorbed H<sub>2</sub>O and OH groups for the constant [11-2] pressure system, presumably due to lower strain energy (Figure 5-45a) and smaller number of surface reaction sites (Figure 5-42, Figure 5-51a). Reaction products also include small

numbers of  $\text{Ni}(\text{H}_2\text{O})_X$  ( $X=2..5$ ) type species for the system at 600K, originating primarily at surface steps and notch/crack surfaces (Figure 5-51c). These could be related to the reduction in Ni work function (ionization energy) upon  $\text{H}_2\text{O}$  adsorption, obtained by a many-electron embedding theory [194], as well as indicate weak Ni atom bonding at surfaces less stable than  $\{111\}$ . Furthermore, it is observed that the hydrostatic pressure of water may correlate with the amount of  $\text{H}_3\text{O}^+$  ions in the liquid (Figure 5-52b,c), since lower increase of  $\text{H}_3\text{O}^+$  is observed at 600K than at 300K. Likewise, the pressure rise is observed to be insignificant at 600K, as compared to 300K, presumably due to higher  $\text{H}_2\text{O}$  diffusivity. It should be added that the absence of oxide layers formation, which may occur upon application of external electric field [100], precludes stress corrosion cracking effects as observed in [102].

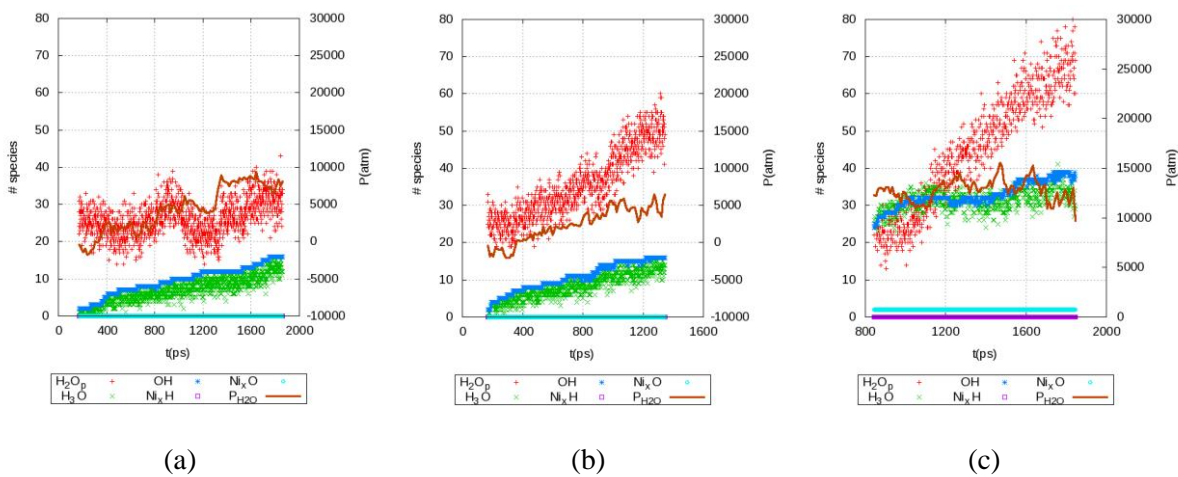


Figure 5-52. Reaction species and water pressure vs. time for  $[1-10]$  strained fcc-Ni slab in water: 300K systems with  $P_{[11-2]}=\text{const}$  (a) and  $dx_{[11-2]}=\text{const}$  (b) and a  $dx_{[11-2]}=\text{const}$  system at 600K (c).

### 5.8.3 Summary

- Stress triaxiality reduces Ni strength through increased dislocation emission barriers and increased reactivity, the latter resulting from higher strain energy.
- Pre hydroxylation in limited amount may significantly increase dislocation emission energy barriers, corresponding to thin film rupture
- Constant pressure corrosive environment may reduce dislocation emission energy barriers, depending on the applied strain rate.

- Overall effect of corrosive environment results in lower material failure strain and lower strain energy capacity, as compared to the structures in vacuum, due to necking type transformations and reduced dislocation barriers.
- Elevated temperature below an active oxide formation temperature range, at a strain rate above that of stable surface layer formation, reduces material's ductility and strength due to reduced dislocation emission barriers, increased reactivity and dissolution at the surfaces.

## **5.9 fcc-Al hydrogen embrittlement study**

### **5.9.1 Structures**

For the HE study an fcc-Al oxide-terminated slab structure, identical to the one used in the strain rate study for the metal case except for a half-elliptical notch instead of the rectangular one (section 5.4.1), was considered.

For the hydrogen interactions two systems were implemented. In the first system 162 H atoms located in place of 162 Al vacancies, distributed in pairs periodically throughout the Al slab part. In the second system 162 H atoms were distributed randomly in the Al slab part. For the latter system no initial vacancies were introduced in the structure. It should be stressed that the chosen concentrations are intended to represent local oversaturated densities, since the experimental hydrogen solubility is of an order of  $10^{-8}$  H/Al atomic fractions [119].

### **5.9.2 Method**

The simulations were performed with the NVT/NPT ensemble at 300K with temperature damping of 100 fs and 0 atm lateral pressure with damping of 10000 fs. Deformation rate of  $5e-6$  fs<sup>-1</sup> with 0.25% 0.5 ps stretching in [1-10] direction alternating with 2.5 ps relaxation periods was used. The boundary

conditions correspond to plane stress conditions. For the structure without H impurities an additional stiffness enhancing constrain was imposed by fixing [1-10] direction displacements for a 6 Å layer of atoms perpendicular to the loading direction at a maximum distance from the notch. For evaluation of strain rate and constant strain effects additional simulations of the hydrogen containing systems at fixed strain levels were performed, starting from selected configurations of the deformation simulations. A cutoff radius of 10 Å and simulation time increments of 20 ps were used for the atomic strain calculation.

### 5.9.3 Results and Discussion

The similarity of stress responses (Figure 5-53b) indicates that overall deformation in all cases involves a similar level of plasticity. However, the potential energy response indicates that the energy capacity of the material, characterized by the energy levels reached after yielding, drops most significantly for the structure with H-filled vacancies, that of the bulk distributed H being slightly higher. The observations are confirmed by the structure snapshots (Figure 5-54 – Figure 5-56), which indicate void initiated ( $\epsilon=0.25$ ) ductile slip failure along grain boundaries for the pure metal case (Figure 5-54), whereas the structure with H-filled vacancies fails after a void coalescence facilitated locally plastic fracture ( $\epsilon=0.2$ ), without slab cross section size reduction before fracture, propagates through the metal thickness (Figure 5-56), revealing H populated surfaces. The mechanism is identified as adsorption-induced dislocation emission (AIDE) [114] type. Similarly, the bulk distributed hydrogen structure failure initiates with a brittle fracture along a newly formed grain boundary ( $\epsilon=0.18$ ), revealing H populated surfaces (Figure 5-55). The mechanism is identified as hydrogen-enhanced decohesion [113] type, yet, due to the presence of isolated voids at grain boundaries, the AIDE mechanism is also assumed to be active. In the latter case crack propagates further in a sliding manner along grain boundaries, which explains the closer similarity with the pure metal case and is in qualitative agreement with the finding [195] that H may facilitate brittle fracture and dislocation emission simultaneously. It is also observed that

for the same system only a single grain is formed, which merges with the initial lattice after the formation of a second crack. Since no grain formation or lattice re-orientation was observed for similar fcc-Ni systems with a fixed [11-2] dimension (section 5.8.2), it is suggested that less extensive grain formation events would occur for analogous boundary conditions also in the current systems.

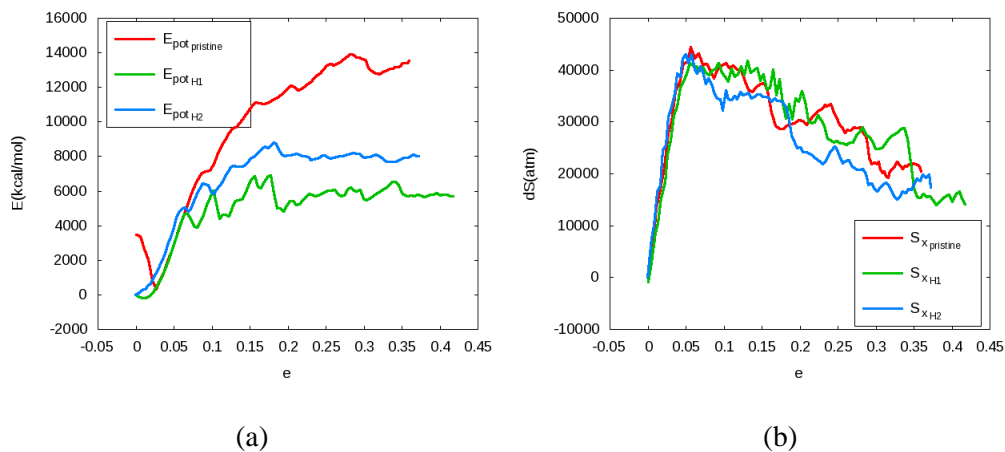


Figure 5-53. Potential energy (a) and tensile stress (b) vs. strain: comparison for [1-10] strained  $\alpha$ - $\text{Al}_2\text{O}_3$ -terminated fcc-Al slab (H1 - structure with initial H-filled vacancies, H2 - structure with bulk distributed H, without initial vacancies).

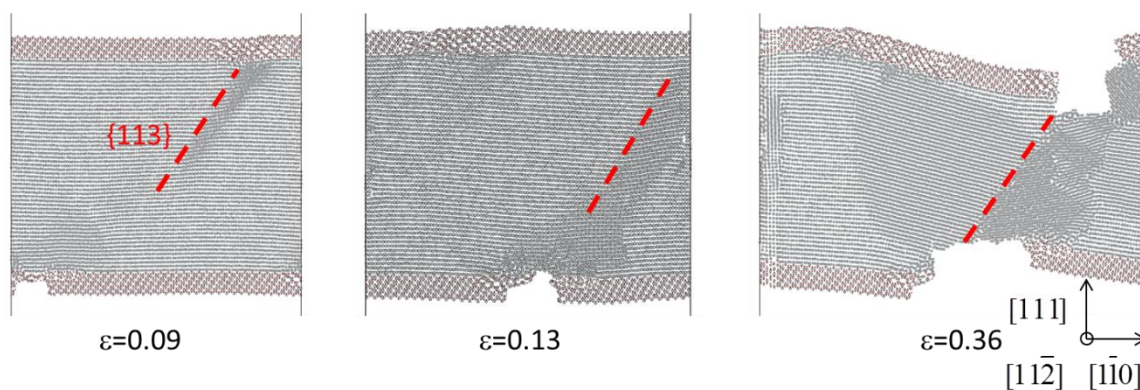


Figure 5-54. [1-10] strained  $\alpha$ - $\text{Al}_2\text{O}_3$ -terminated fcc-Al slab ( $152.3 \times 9.77 \times 148.8$  Å); configuration snapshots (Al – grey, O – red).

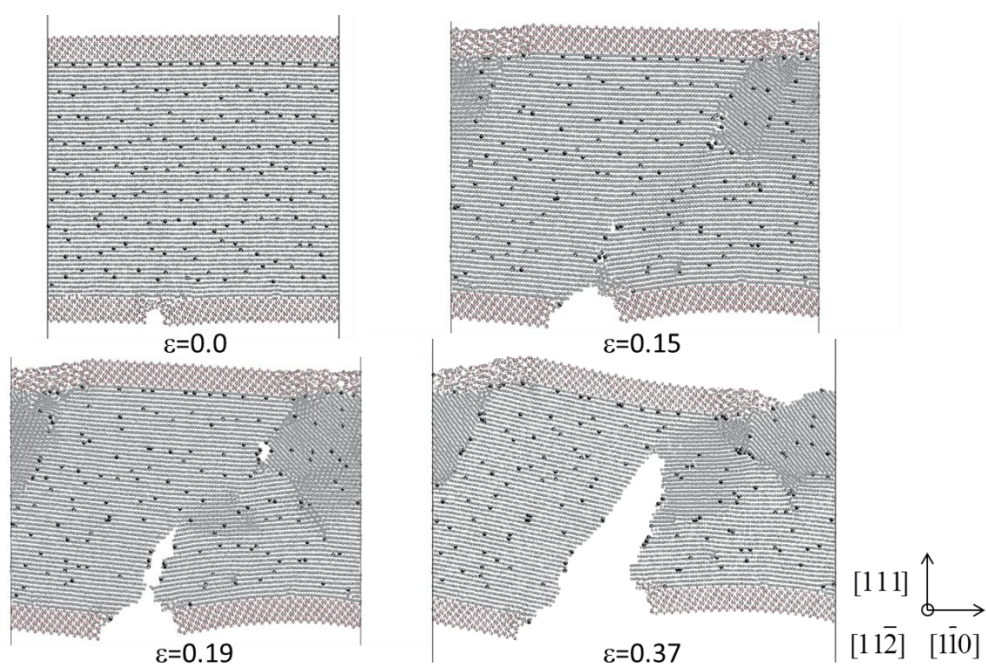


Figure 5-55. [1-10] strained  $\alpha$ -Al<sub>2</sub>O<sub>3</sub>-terminated fcc-Al slab (152.3x9.77x148.8 Å) with bulk distributed H, without initial vacancies; configuration snapshots (Al – grey, O – red, H – black).

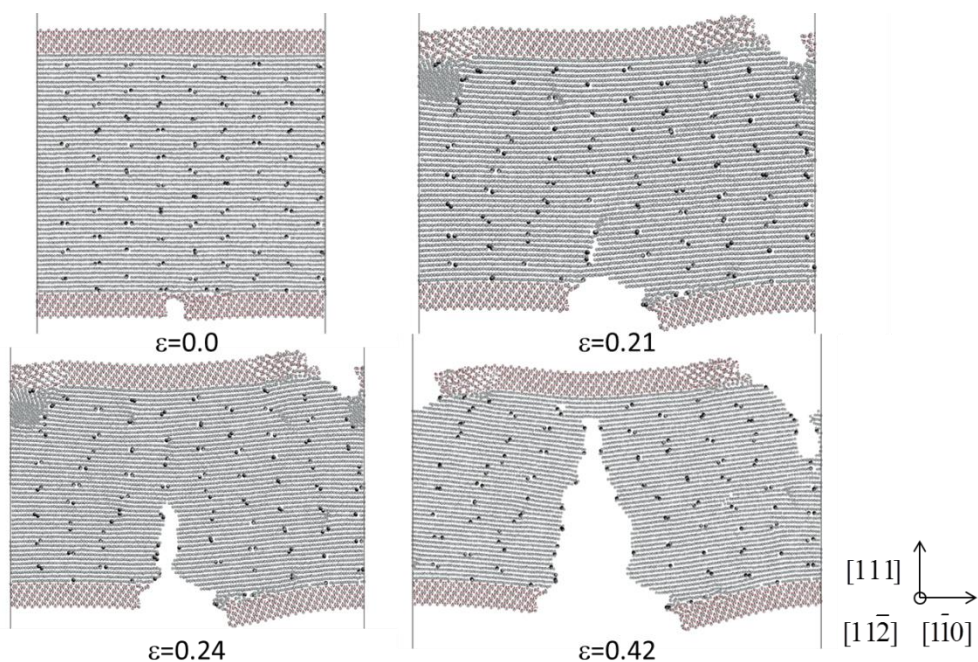
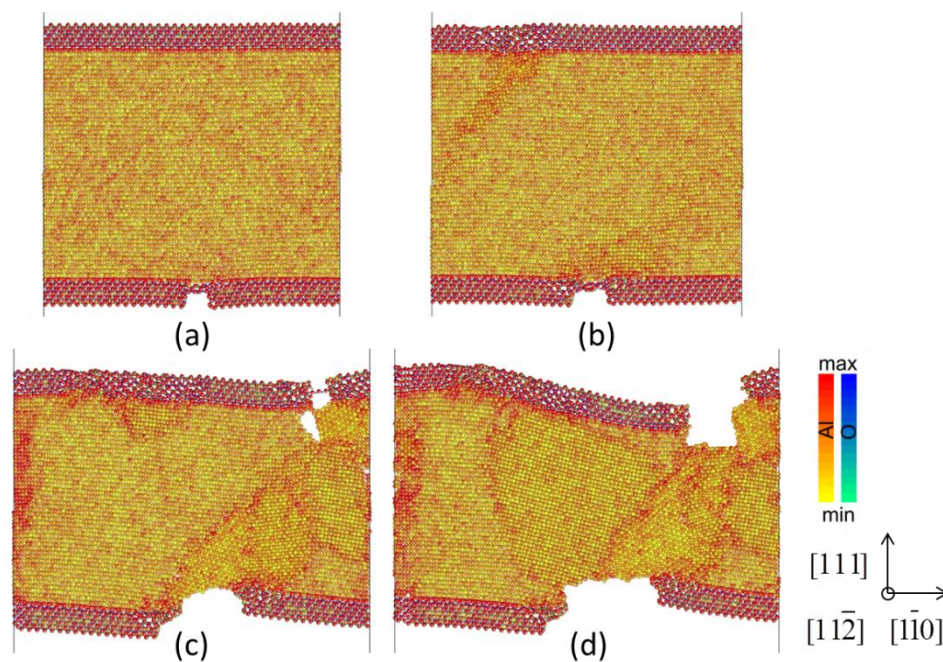


Figure 5-56. [1-10] strained  $\alpha$ -Al<sub>2</sub>O<sub>3</sub>-terminated fcc-Al slab (152.3x9.77x148.8 Å) with initial H-filled vacancies; configuration snapshots (Al – grey, O – red, H – black).

The observed dislocations are emitted predominantly along  $\{113\}$  planes instead of expected  $\{111\}$  slip for cracks in single crystal Al structures [160] or fcc metals generally [162, 163, 191, 196]. Analogously to section 5.8.2, the difference may be due to the quasi 2D boundary condition in  $[11-2]$  direction,  $\{113\}$  being the 2D projection of a  $\{111\}$  plane. The particular plane, however, can be also related to experimental findings for low angle  $\langle 112 \rangle$  tilt axis grain boundary formation in fcc-Al [197]. More generally, scale effects due to change in surface to volume ratio [198] at small strain levels [199] could account for the dislocation behavior in response to the particular boundary conditions.

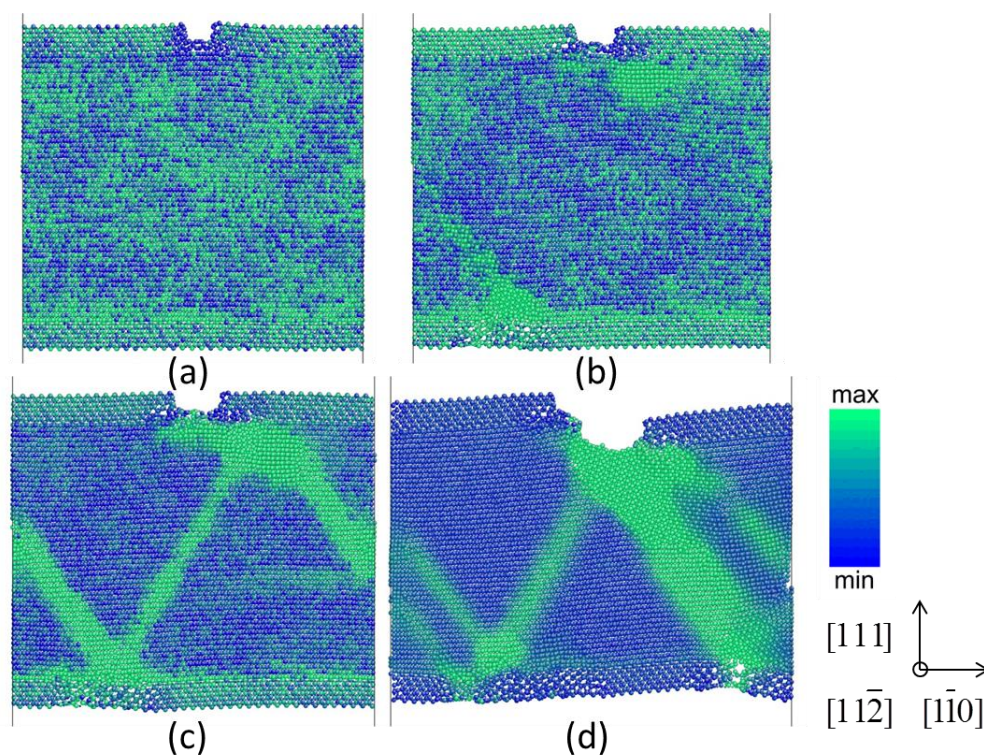
The overall behavior of void and slip assisted fracture, as present in the pristine Al simulation results, has been observed both experimentally and computationally in an aluminum alloy for positive average stress triaxiality below  $\sim 0.4$  [189], which corresponds to the estimated stress triaxiality of  $\sim 0.33$  for a uniaxially deformed structure with lateral stress relaxation in the current study. Yet the presence of H on crack surfaces indicates its effect on weakening the material prior to failure and the related void formation, which can be attributed to strong H-vacancy bonding [118] and the mechanism of surface-H facilitated transport of other H atoms to a surface [195]. Another possible mechanism is related to the increase in dislocation nucleation energy barriers [101, 111], which may cause stresses at the crack tip that exceed yield stress of the metal. This mechanism is in agreement with the current results, since less grain formation, particularly in the structure with initial vacancies, is observed for the H containing structures. Moreover, the extent of dislocation nucleation barriers ( $\varepsilon=0.1$  and  $\varepsilon=0.18$ ) clearly indicates H effect in the structure with initial vacancies, as compared against almost barrier-less dislocation emission in pristine Al (Figure 5-53). However, the H migration to the crack tip, in contrast to the high H concentration model in [111], does not exceed segregation on grain boundaries or in the vicinity of other defects. That can be attributed to the obtained stress distributions (Figure 5-57), which do not indicate extended stress gradient around the crack tip, as compared to analogous  $\text{Al}_2\text{O}_3$  structures (Figure 5-23), instead suggesting localized stress concentration along grain boundaries, dislocations and other defects.

Similarly, distinct octahedral strain localization is observed along traces of slip bands, which form bridges between grain locations (Figure 5-58), as well as in the oxide layers and at oxide/metal interfaces before the dislocation nucleation.



configuration	$\varepsilon$	$S_{\min \text{ Al}}$ (GPa)	$S_{\max \text{ Al}}$ (GPa)
a	0.00	2.1	13.2
b	0.09	1.8	16.7
c	0.17	2.2	17.4
d	0.35	2.5	17.0

Figure 5-57. [1-10] strained  $\alpha$ - $\text{Al}_2\text{O}_3$ -terminated fcc-Al slab ( $152.3 \times 9.77 \times 148.8 \text{ \AA}$ ) snapshots; max. normal stress distribution.



configuration	$\varepsilon$	$E_{\min}$	$E_{\max}$
a	0.03	0.22	0.36
b	0.09	0.35	0.45
c	0.10	0.38	0.51
d	0.22	0.39	0.79

Figure 5-58. [1-10] strained  $\alpha$ -Al<sub>2</sub>O<sub>3</sub>-terminated fcc-Al slab (152.3x9.77x148.8 Å) snapshots; octahedral Almansi strain distribution.

Two known H diffusion related mechanisms were distinguished in the simulations. First, the Gorski effect, which is attributed to long-range order relaxation by migration of solutes to regions of dilatation under stress gradient conditions until balance/equilibrium between chemical potential and solute concentration gradients is obtained. The mechanism is supported by simulation snapshots which indicate H accumulation at grain boundaries, voids and interfaces (Figure 5-55, Figure 5-56) [200]. Second, the Zener effect, which is defined as stress caused directional short-range order relaxation of interstitial atom pairs or solute-vacancy pairs due to lower symmetry strain fields [200]. The mechanism is in agreement with the obtained diffusivity estimates for different strain levels (Figure 5-60), which indicate a nonlinear relation between fcc-Al stress and the H diffusivities. Furthermore, a hysteresis type

relation above  $1e4$  atm is obtained with a saturation limit of about  $2.5e-6$  cm<sup>2</sup>/s, which suggests that plastic deformations may induce higher H migration, most likely occurring in high stress concentration regions, e.g., grain boundaries. Likewise, the saturation limit is assumed to result from plastic deformation that limits the extent of local elastic strain, which accounts for the diffusion mechanisms discussed above. A further insight can be obtained by comparing diffusivities of sample sets of H atoms distributed in the bulk and on the surfaces (Figure 5-59), which indicate that the mean squared displacement of the surface H atoms approaches a constant value, hence a comparatively negligible diffusivity. This result correlates with the low H diffusivity in the H-filled vacancies structure (Table 5-7), which indicates that the H atoms primarily get trapped close to the vacancies or other defects. The latter observations significantly reduce the crack tip diffusion mechanism possibility [111]. This behavior is found to be in qualitative agreement with DFT calculated H diffusion barriers between tetrahedral and octahedral sites vs. migration away from a vacancy [118], the ab initio MD results based theory for diffusion dependence on concentrations of lattice and trapped site H atoms [117] as well as in quantitative agreement with experimental data (Table 5-7). Furthermore, the agreement of non-strained bulk distributed H structure H diffusivities with ab initio reference data (Table 5-7) suggests that only lattice or only vacancies/defects placed H diffusivities are not strictly dependent on the respective H concentrations.

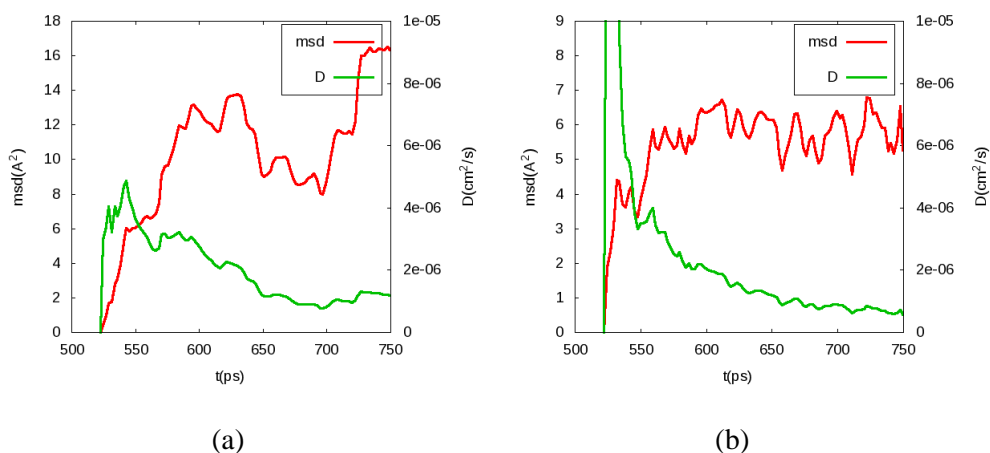


Figure 5-59. Comparison of bulk (a) and surface (b) 10-atom sample H diffusivities and mean square displacement in [1-10] strained  $\alpha$ - $\text{Al}_2\text{O}_3$ -terminated fcc-Al slab with bulk distributed H, without initial vacancies, at  $\epsilon=0.37$ .

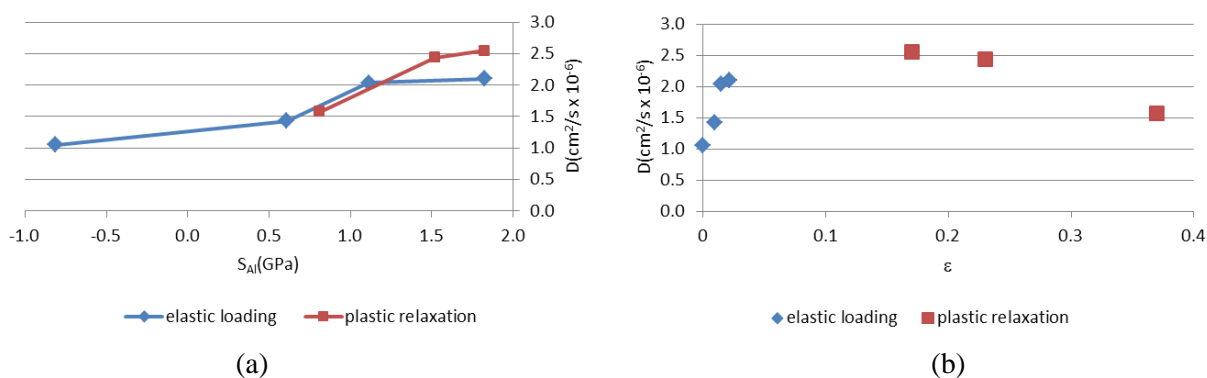


Figure 5-60. H diffusivity vs. tensile stress (a) and strain (b) in [1-10] strained  $\alpha$ - $\text{Al}_2\text{O}_3$ -terminated fcc-Al slab with bulk distributed H, without initial vacancies.

Table 5-7. H diffusivity comparison for fcc-Al.

	$D[\text{cm}^2/\text{s}]$
Experiment [119]	$\sim 1.5\text{e-}7$
DFT [117, 118]*	$\sim 1.7\text{e-}6$
Reax ( $\epsilon=0$ , no vacancies)	$\sim 1\text{e-}6$
Reax ( $\epsilon=0$ , vacancy trapped)	$< 3\text{e-}7$
* estimated using an Arrhenius relation without vacancy effects	

The strain rate effects for the structure with bulk distributed H were evaluated by comparing the potential energy and stress responses (Figure 5-61) for the dynamic stretching and fixed deformation relaxation at different tension strain levels. The fixed strain relaxation at maximum potential energy, which coincides with crack initiation, yields void formation (Figure 5-62), which significantly reduces the potential energy and stress. In contrast, there are no potential energy or stress reductions at strain levels before yielding and comparatively small and slow reductions at strain levels after crack propagation. This indicates that, except for the crack propagation stage, the applied strain rate approaches a quasi-static state. Related strain rate effects in plastic materials have been described by an MD validated empirical temperature dependent phonon damping terms, which result in an increase of flow stress, if a threshold strain rate value is exceeded [198].

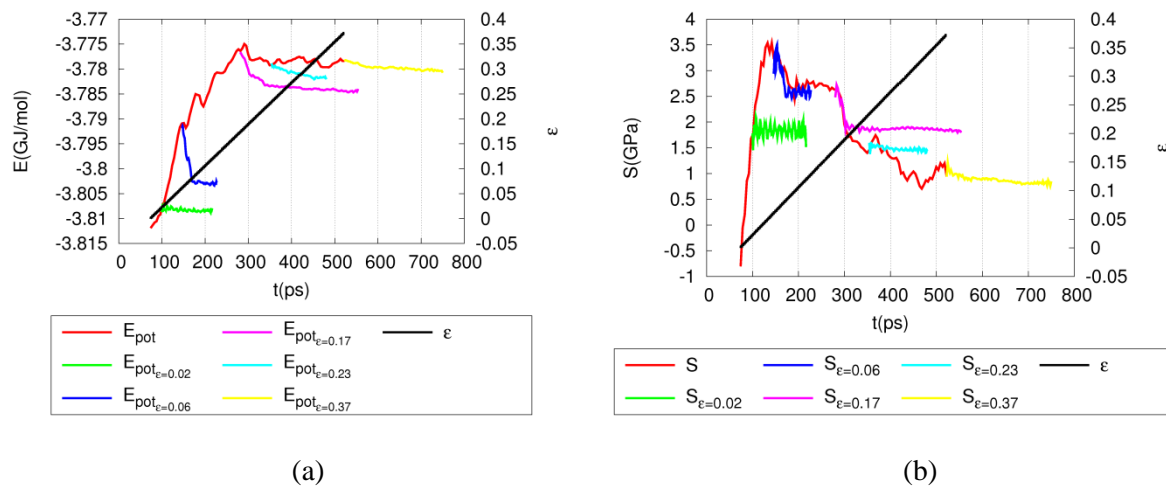


Figure 5-61. Potential energy (a) and tensile stress (b) vs. time: loading rate comparison for [1-10] strained  $\alpha$ - $\text{Al}_2\text{O}_3$ -terminated fcc-Al slab with bulk distributed H, without initial vacancies.

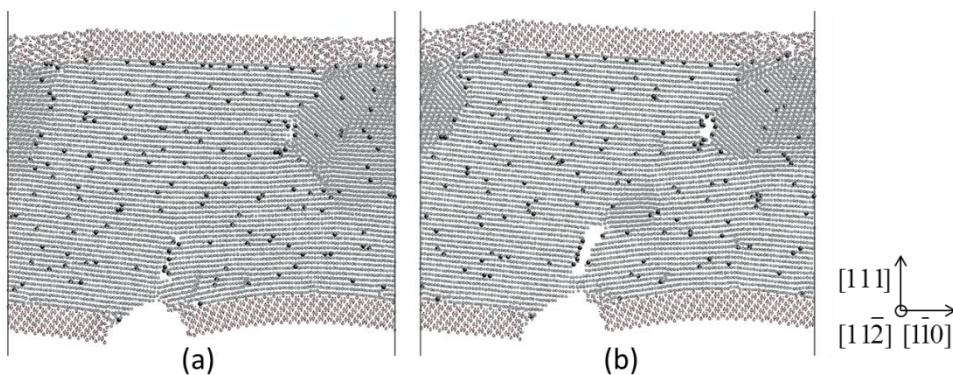


Figure 5-62. Relaxation of  $[1-10]$  strained  $\alpha\text{-Al}_2\text{O}_3$ -terminated fcc-Al slab ( $152.3 \times 9.77 \times 148.8 \text{ \AA}$ ) with bulk distributed H, without initial vacancies, at  $\varepsilon=0.17$ ; configuration snapshots at 280 ps (a) and 550ps (b) (Al – grey, O – red, H – black).

#### 5.9.4 Summary

- Under partial confinement conditions due to surface oxide layers, pristine material fails due to dislocation slip along grain boundaries and void formation.
- Hydrogen in initially defect free material migrates locally to newly formed grain boundaries and facilitates void assisted intergranular brittle crack initiation. Due to slow H surface migration further crack propagation occurs by dislocation slip.
- Hydrogen in uniformly volume distributed vacancies has significantly lower diffusivity than in defect free material, resulting in comparatively high dislocation emission barriers, limited grain formation and void initiated locally plastic fracture failure without slab cross section size reduction before fracture.
- Both hydrogen containing systems yield reduced predicted failure strains and strain energy capacity. Since the material strength is not significantly affected, the changes in material response are attributed to embrittlement effects.
- Finite temperature and strain rate effects on HE are manifested through diffusivity temperature dependence, the extent of relaxation at crack initiation and propagation, and negligible hydride region formation. Subsequently, the HE effect is expected to increase for quasi static-strain rates.
- Hydrogen diffusivity dependence on microstructure is evident due to the presence of hysteresis in diffusivity as a function of tensile stress, which indicates an increase during plastic deformation, compared to purely elastic deformation.

## 5.10 Conclusion and Outlook

The presented studies have highlighted diverse atomistic chemical/mechanical failure mechanisms in common alloy metals and a protective oxide coating material, which may be relevant for application in similar environments under equivalent mechanical and thermal conditions. Particular concern should be taken regarding mesoscale dimension and larger time scale effects, which are not fully considered in the current studies and would motivate the application of extended time scale and multiple spatial scale methods. Yet the current studies are considered as useful upper nanoscale references for further study.

Within the context of environmentally assisted mesoscopic material failures, further studies of interest would include multigrain/polycrystalline structures with added impurity/dopant elements, as well as structures representing particular industrial alloy component combinations. Focus on specific application-based boundary conditions and environments could yield more accurate behavior predictions. Furthermore, for the purpose of computational materials design, the approach of scanning structure combinations with respect to element and phase content would be of relevance.

## References

1. Griffin, T., et al., *Advanced Zero Emissions Gas Turbine Power Plant*. Journal of Engineering for Gas Turbines and Power, 2005. **127**(1): p. 81-85.
2. Anderson, R.E., et al. *Adapting gas turbines to zero emission oxy-fuel power plants*. in *2008 ASME Turbo Expo, June 9, 2008 - June 13, 2008*. 2008. Berlin, Germany: American Society of Mechanical Engineers.
3. Alvin, M.A., *Materials and Component Development for Advanced Turbine Systems: Project Summary*. ASME Conference Proceedings, 2010. **2010**(43963): p. 1005-1016.
4. Pint, B.A., J.R. DiStefano, and I.G. Wright, *Oxidation resistance: One barrier to moving beyond Ni-base superalloys*. Materials Science & Engineering A (Structural Materials: Properties, Microstructure and Processing), 2006. **415**(1-2): p. 255-63.
5. Dogan, O.N., P.E. King, and M.C. Gao, *Integrated Design and Rapid Development of Refractory Metal Based Alloys for Fossil Energy Applications*. DOE/NETL-IR-2008-209, 22nd Annual Conference on Fossil Energy Materials, July 8-10, 2008, Pittsburgh, PA, 2008.
6. Burke, K., *Perspective on density functional theory*. Journal of Chemical Physics, 2012. **136**(15).
7. Chenoweth, K., A.C.T. van Duin, and W.A. Goddard, III, *ReaxFF reactive force field for molecular dynamics simulations of hydrocarbon oxidation*. Journal of Physical Chemistry A, 2008. **112**(Copyright 2008, The Institution of Engineering and Technology): p. 1040-53.
8. Root, S., et al., *Shock compression of hydrocarbon foam to 200 GPa: Experiments, atomistic simulations, and mesoscale hydrodynamic modeling*. Journal of Applied Physics, 2013. **114**(10): p. -.
9. Van Duin, A.C.T., et al., *ReaxFF: A reactive force field for hydrocarbons*. Journal of Physical Chemistry A, 2001. **105**(Compendex): p. 9396-9409.
10. Yu, S., et al., *Self-diffusion in the intermetallic compounds NiAl and Ni3Al: An embedded atom method study*. Physica B: Condensed Matter, 2007. **396**(1-2): p. 138-144.
11. te Velde, G., et al., *Chemistry with ADF*. Journal of Computational Chemistry, 2001. **22**(9): p. 931-967.
12. *LAMMPS Users Manual*. [cited 2013; Available from: <http://lammps.sandia.gov>.
13. Frenkel, D. and B. Smit, *Understanding Molecular Simulation - From Algorithms to Applications*. 2nd ed. Computational Science Series, ed. M.K. D. Frenkel, M.Parrinello, B. Smit. 2002: Academic Press.
14. Berendsen, H.J.C., et al., *Molecular dynamics with coupling to an external bath*. J . Chem. Phys., 1984. **81**(8): p. 7.
15. *NIST Computational Chemistry Comparison and Benchmark Database*. 2013; 16a:[Available from: <http://cccbdb.nist.gov/>
16. van Duin, A.C.T., *ReaxFF User Manual*. 2002.
17. Tuckerman, M., B.J. Berne, and G.J. Martyna, *Reversible multiple time scale molecular dynamics*. Journal of Chemical Physics, 1992. **97**(3): p. 1990-2001.
18. Dowling, N.E., *Mechanical Behavior of Materials*. 3 ed. 2007: Pearson Prentice Hall.
19. Nielsen, O.H. and R.M. Martin, *First-principles calculation of stress*. Physical Review Letters, 1983. **50**(9): p. 697-700.
20. Matsuo, H., et al., *Electron microscopy analysis for crack propagation behavior of alumina*. International Journal of Fatigue, 2010. **32**(3): p. 592-8.

21. Li, J.-F. and R. Watanabe, *Brittle-to-ductile transition and high-temperature deformation in ZrO<sub>2</sub>(Y<sub>2</sub>O<sub>3</sub>) and Al<sub>2</sub>O<sub>3</sub> ceramics as evaluated by small punch test*. Materials Transactions, JIM, 1999. **40**(6): p. 508-513.
22. Zhou, M. *Theoretical interpretation of the virial stress*. in *44th AIAA/ASME/ASCE/AHS/ASC Structures, Structural Dynamics, and Materials Conference, April 7, 2003 - April 10, 2003*. 2003. Norfolk, VA, United states: American Inst. Aeronautics and Astronautics Inc.
23. Gullett, P.M., et al., *A deformation gradient tensor and strain tensors for atomistic simulations*. Modelling and Simulation in Materials Science and Engineering, 2008. **16**(1).
24. Zimmerman, J.A., D.J. Bammann, and H. Gao, *Deformation gradients for continuum mechanical analysis of atomistic simulations*. International Journal of Solids and Structures, 2009. **46**(2): p. 238-253.
25. Haupt, P., *Continuum Mechanics and Theory of Materials* 2nd ed. 2002: Springer.
26. Zimmerman, J.A., et al., *Surface step effects on nanoindentation*. Physical Review Letters, 2001. **87**(16): p. 165507-1.
27. Kelchner, C.L., S.J. Plimpton, and J.C. Hamilton, *Dislocation nucleation and defect structure during surface indentation*. Physical Review B (Condensed Matter), 1998. **58**(17): p. 11085-8.
28. Li, J., *AtomEye: An efficient atomistic configuration viewer*. Modelling and Simulation in Materials Science and Engineering, 2003. **11**(2): p. 173-177.
29. Zhang, C., et al., *Fracture initiation mechanisms in -alumina under hypervelocity impact*. Applied Physics Letters, 2007. **91**(12): p. 121911-1.
30. Buehler, M.J., et al., *Cracking and adhesion at small scales: atomistic and continuum studies of flaw tolerant nanostructures*. Modelling and Simulation in Materials Science and Engineering, 2006. **14**(5): p. 799-816.
31. Khare, R., et al., *Coupled quantum mechanical/molecular mechanical modeling of the fracture of defective carbon nanotubes and graphene sheets*. Physical Review B (Condensed Matter and Materials Physics), 2007. **75**(7): p. 75412-1.
32. Tsai, J.-L., S.-H. Tzeng, and Y.-J. Tzou, *Characterizing the fracture parameters of a graphene sheet using atomistic simulation and continuum mechanics*. International Journal of Solids and Structures, 2010. **47**(3-4): p. 503-509.
33. Li, J., *AtomEye: an efficient atomistic configuration viewer*. Modelling and Simulation in Materials Science and Engineering, 2003. **11**(2): p. 173.
34. Xue, J., W. Zhao, and G.K. Wolf, *The corrosion properties of Al/Al<sub>2</sub>O<sub>3</sub> multilayered coatings on CK45 steel deposited by IBAD*. Surface & Coatings Technology, 2004. **187**(2-3): p. 194-8.
35. Quinn, G.D., *Delayed failure of a commercial vitreous bonded alumina*. Journal of Materials Science, 1987. **22**(7): p. 2309-18.
36. Ebrahimi, M.E., J. Chevalier, and G. Fantozzi, *Slow crack-growth behavior of alumina ceramics*. Journal of Materials Research, 2000. **15**(1): p. 142-147.
37. Otte, H.M. and A.G. Crocker, *Crystallographic Formulae for Hexagonal Lattices*. physica status solidi (b), 1965. **9**(2): p. 441-450.
38. Mauder, C., et al., *Development of m-plane GaN anisotropic film properties during MOVPE growth on LiAlO<sub>2</sub> substrates*. Journal of Crystal Growth, 2010. **312**(11): p. 1823-1827.
39. Pint, B.A., J.R. DiStefano, and I.G. Wright, *Oxidation resistance: One barrier to moving beyond Ni-base superalloys*. Materials Science & Engineering A (Structural Materials: Properties, Microstructure and Processing), 2006. **415**(Copyright 2006, IEE): p. 255-63.
40. Nganbe, M. and M. Heilmaier, *High temperature strength and failure of the Ni-base superalloy PM 3030*. International Journal of Plasticity, 2009. **25**(Compendex): p. 822-837.
41. Speight, K.G., *Lange's Handbook of Chemistry* 2005, McGraw-Hill.
42. Svistunova, T., *Corrosion-Resistant Alloys for Very Highly Corrosive Media*. Metal Science and Heat Treatment, 2005. **47**(7): p. 383-389.

43. Tawancy, H., *Comparative corrosion behavior of Ni–Mo and Ni–Mo–Cr alloy for applications in reducing environments*. Journal of Materials Science, 2006. **41**(24): p. 8359-8362.
44. G. Wang, M.A.V.H., P.N. Ross, M.I. Baskes *Quantitative prediction of surface segregation in bimetallic Pt–M alloy nanoparticles (M = Ni, Re, Mo)*. Progress in Surface Science, 2005. **79**: p. 18.
45. M. Polak, L.R., *The competition between surface segregation and compositional ordering in alloys: theory and experimental observations of segregation versus temperature peaked curves*. Colloids and Surfaces A: Physicochemical and Engineering Aspects, 2002. **208** p. 8.
46. Vasenkov, A., et al., *Reactive molecular dynamics study of Mo-based alloys under high-pressure, high-temperature conditions*. Journal of Applied Physics, 2012. **112**(1): p. 013511.
47. Edgar, E.L., *Periodic Table of the Elements*. 1993, Gaston, Oregon.
48. P.H.T. Philipsen, E.J.B., *Cohesive energy of 3 d transition metals: Density functional theory atomic and bulk calculations*. Physical Review B, 1996. **54**(8): p. 8.
49. A. Ignatiev, F.J., H.D. Shih, *The structure of the clean Mo[001] surface*. Phys. Rev. B, 1975. **11**(12): p. 8.
50. Fleet, M.E., *The Crystal Structure of alpha-Ni7S6*. Acta Cryst., 1972. **B28**: p. 5.
51. Sidgwick, N.V., *The chemical elements and their compounds*. 1950: Clarendon Press. 1703.
52. Letzig, D., J. Klower, and G. Sauthoff, *Screening of NiAl-base Ni-Fe-Al alloys for structural high temperature applications and development of a new Ni-30Fe-10Al-Cr alloy*. Zeitschrift fur Metallkunde, 1999. **90**(9): p. 712-21.
53. Deevi, S.C. and V.K. Sikka, *Nickel and iron aluminides: an overview on properties, processing, and applications*. Intermetallics, 1996. **4**(5): p. 357-75.
54. Foiles, S.M. and M.S. Daw, *Application of the embedded atom method to Ni3Al*. Journal of Materials Research, 1987. **2**(1): p. 5-15.
55. Daw, M.S. and M.I. Baskes, *Embedded-atom method: derivation and application to impurities, surfaces, and other defects in metals*. Physical Review B (Condensed Matter), 1984. **29**(12): p. 6443-53.
56. Eunkoo, L. and L. Byeong-Joo, *Modified embedded-atom method interatomic potential for the Fe-Al system*. Journal of Physics: Condensed Matter, 2010. **22**(17): p. 175702 (9 pp.).
57. Mekhrabov, A.O. and M.V. Akdeniz, *Modelling and Monte Carlo simulation of the atomic ordering processes in Ni3Al intermetallics*. Modelling and Simulation in Materials Science and Engineering, 2007. **15**(2): p. 1-12.
58. Hui, L., B. Xiufang, and W. Guanghou, *Molecular dynamics computation of the liquid structure of Fe50Al50 alloy*. Materials Science and Engineering A, 2001. **298**(1-2): p. 245-250.
59. Helander, T. and J. Agren, *A phenomenological treatment of diffusion in Al-Fe and Al-Ni alloys having B2-BCC ordered structure*. Acta Materialia, 1999. **47**(4): p. 1141-52.
60. Mendeleev, M.I., A.O. Rodin, and B.S. Bokstein. *Computer simulation of diffusion in dilute Al-Fe alloys*. in *7th International Conference on Diffusion in Materials, October 28, 2008 - October 31, 2008*. 2009. Lanzarote, Spain: Trans Tech Publications Ltd.
61. Mendeleev, M.I., A.O. Rodin, and B.S. Bokstein. *Computer simulation of Fe diffusion in liquid Al and along Al grain boundaries*. in *International Conference on Grain Boundary Diffusion, Stresses and Segregation, DSS 2010, June 1, 2010 - June 4, 2010*. 2011. Moscow, Russia: Trans Tech Publications Ltd.
62. Debiaggi, S.B., P.M. Decorte, and A.M. Monti, *Diffusion by vacancy mechanism in Ni, Al, and Ni3Al: calculation based on many-body potentials*. Physica Status Solidi B, 1996. **195**(1): p. 37-54.
63. Duan, J., Y.N. Osetsky, and D.J. Bacon. *Atomistic study of self-diffusion in Ni, Al and Ni3Al*. in *Proceedings of the Fifth International Conference on Diffusion in Materials (DIMAT 2000), July 17, 2000 - July 21, 2000*. 2001. Paris, France: Trans Tech Publications Ltd.

64. Frank, S. and C. Herzig. *The effect of composition and temperature on grain boundary diffusion of 63Ni in Ni3Al alloys*. in *4th Conference on High Temperature Intermetallics, 27 April-1 May 1997*. 1997. Switzerland: Elsevier.
65. Horbach, J., et al., *Self-diffusion and interdiffusion in Al80Ni20 melts: simulation and experiment*. Physical Review B (Condensed Matter and Materials Physics), 2007. **75**(17): p. 174304-1.
66. Jinsong, D., *Atomistic simulations of diffusion mechanisms in off-stoichiometric Al-rich Ni3Al*. Journal of Physics: Condensed Matter, 2007. **19**(8): p. 9 pp.
67. Li, W., B. Xiufang, and Z. Jingxiang, *Computer simulation of supercooled liquid and glassy Ni3Al*. Physics and Chemistry of Glasses, 2002. **43**(6): p. 280-2.
68. Schmidt, C. and J.L. Bocquet. *Calculation of the diffusion parameters in an ordered Ni3Al-alloy for a relaxed lattice*. in *Diffusion Mechanisms in Crystalline Materials. Symposium, 13-16 April 1998*. 1998. Warrendale, PA, USA: Mater. Res. Soc.
69. Zhang, L., I. Steinbach, and Y. Du, *Phase-field simulation of diffusion couples in the Ni-Al system*. International Journal of Materials Research, 2011. **102**(4): p. 371-380.
70. Das, S.K., J. Horbach, and T. Voigtmann, *Structural relaxation in a binary metallic melt: molecular dynamics computer simulation of undercooled Al80Ni20*. Physical Review B (Condensed Matter and Materials Physics), 2008. **78**(6): p. 064208-1.
71. Divinski, S.V., et al., *Ni self-diffusion in NiAl: an experimental investigation of the temperature and composition dependencies and atomistic simulation of diffusion mechanisms*. Diffusion and Defect Data Pt.B: Solid State Phenomena, 2000. **72**: p. 203-208.
72. Evteev, A.V., et al., *Molecular dynamics simulation of diffusion in a (110) B2-NiAl film*. Intermetallics, 2011. **19**(7): p. 848-854.
73. Griesche, A., et al. *Atomic diffusion and its relation to thermodynamic forces in Al-Ni melts*. in *7th International Conference on Diffusion in Materials, October 28, 2008 - October 31, 2008*. 2009. Lanzarote, Spain: Trans Tech Publications Ltd.
74. Dai, Y., S. Zhu, and F. Wang. *Study on Ni/Al interface diffusion at initial time by using molecular dynamics method*. in *2011 International Symposium on Chemical Engineering and Material Properties, ISCEMP 2011, November 4, 2011 - November 6, 2011*. 2012. Shenyang, Liaoning, China: Trans Tech Publications.
75. Van Duin, A.C.T., et al., *ReaxFF: A reactive force field for hydrocarbons*. Journal of Physical Chemistry A, 2001. **105**(41): p. 9396-9409.
76. Vasenkov, A., et al., *Reactive molecular dynamics study of Mo-based alloys under high-pressure, high-temperature conditions*. Journal of Applied Physics, 2012. **112**(1).
77. LaBrosse, M.R., J.K. Johnson, and A.C.T. van Duin, *Development of a Transferable Reactive Force Field for Cobalt*. J. Phys. Chem. A, 2010. **114**(Copyright (C) 2010 American Chemical Society (ACS). All Rights Reserved.): p. 5855-5861.
78. Keith, J.A., et al., *Reactive forcefield for simulating gold surfaces and nanoparticles*. Physical Review B, 2010. **81**: p. 235404-1/235404-8.
79. Zou, C., A.C.T. van Duin, and D. Sorescu, *Theoretical investigation of hydrogen adsorption and dissociation on iron and iron carbide surfaces using the ReaxFF reactive force field method*. Topics in Catalysis, 2012. **55**: p. 391-401.
80. Mueller, J.E., A.C.T. van Duin, and W.A. Goddard, III, *Development and Validation of ReaxFF Reactive Force Field for Hydrocarbon Chemistry Catalyzed by Nickel*. Journal of Physical Chemistry C, 2010. **114**: p. 4939-4949.
81. Chenoweth, K., et al., *Development and application of a ReaxFF reactive force field for oxidative dehydrogenation on vanadium oxide catalysts*. Journal of Physical Chemistry C, 2008. **112**(37): p. 14645-14654.

82. Russo, M., et al., *Molecular Dynamic Simulation of Aluminum-Water Reactions Using the ReaxFF Reactive Force Field*. International Journal of Hydrogen Energy, 2011. **36**: p. 5828-5835.
83. Verners, O., Y.K. Shin, and A.C.T. van Duin, *Molecular dynamics simulation of Al grain mixing in Fe/Ni matrices and its influence on oxidation*. Journal of Applied Physics, 2013. **114**(2): p. 023501.
84. Friak, M. and J. Neugebauer. *Ab initio study of the anomalous volume-composition dependence in Fe-Al alloys*. 2010. Langford Lane, Kidlington, Oxford, OX5 1GB, United Kingdom: Elsevier Ltd.
85. Wang, Y., Z.K. Liu, and L.Q. Chen, *Thermodynamic properties of Al, Ni, NiAl, and Ni<sub>3</sub>Al from first-principles calculations*. Acta Materialia, 2004. **52**(9): p. 2665-2671.
86. Liu, H.B., et al., *Atomic simulation of amorphization and crystallization of Ni<sub>3</sub>Al during rapid solidification*. Philosophical Magazine B (Physics of Condensed Matter: Statistical Mechanics, Electronic, Optical and Magnetic Properties), 1997. **76**(1): p. 75-89.
87. Assadi, H. and A.L. Greer, *Application of disorder trapping theory to the solidification of Ni<sub>3</sub>Al*. ISIJ International, 1995. **35**(6): p. 574-579.
88. Swann, P.R., W.R. Duff, and R.M. Fisher, *Electron metallography of ordering reactions in Fe-Al alloys*. Met Trans, 1972. **3**(2): p. 409-419.
89. Kaye, G.W.C. and T.H. Laby, *Tables of physical and chemical constants*. 15 ed. 1993, London: Longman.
90. James, A.M. and M.P. Lord, *Macmillan's Chemical and Physical Data*. 1992, London: Macmillan.
91. Taylor, A., *Lattice Parameters of Binary Nickel Cobalt Alloys*. Journal of the Institute of Metals, 1950. **77**(6): p. 585-594.
92. Kohlhaas, R., P. Donner, and N. Schmitz-Pranghe, *Z. Angew. Phys.*, 1967. **23**.
93. Witt, W., *An absolute precision measurement of lattice constants on ge and al monocrystals with electron diffraction*. Z. Naturforsch, 1967. **22**(1): p. 92-95.
94. Lynch, S.P., *Mechanisms and kinetics of environmentally assisted cracking: current status, issues, and suggestions for further work*. Metallurgical and Materials Transactions A, 2013. **44**(3): p. 1209-29.
95. Was, G.S., D. Farkas, and I.M. Robertson, *Micromechanics of dislocation channeling in intergranular stress corrosion crack nucleation*. Current Opinion in Solid State and Materials Science, 2012. **16**(3): p. 134-142.
96. Sen, F.G., et al., *Oxidation induced softening in Al nanowires*. Applied Physics Letters, 2013. **102**(5).
97. Zhang, Q., et al., *Adhesion and nonwetting-wetting transition in the Al/ $\alpha$ -Al<sub>2</sub>O<sub>3</sub> interface*. Physical Review B, 2004. **69**(4): p. 045423.
98. Ojwang, J.G.O., et al., *Parametrization of a reactive force field for aluminum hydride*. Journal of Chemical Physics, 2009. **131**(4): p. 044501 (13 pp.).
99. Van Duin, A.C.T., et al., *Development and validation of a ReaxFF reactive force field for Cu cation/water interactions and copper metal/metal oxide/metal hydroxide condensed phases*. Journal of Physical Chemistry A, 2010. **114**(35): p. 9507-9514.
100. Assowe, O., et al., *Reactive molecular dynamics of the initial oxidation stages of Ni(111) in pure water: Effect of an applied electric field*. Journal of Physical Chemistry A, 2012. **116**(48): p. 11796-11805.
101. Zamora, R.J., et al., *Ab initio prediction of environmental embrittlement at a crack tip in aluminum*. Physical Review B (Condensed Matter and Materials Physics), 2012. **86**(6): p. 060101 (5 pp.).

102. Das, N.K., et al., *Early stage SCC initiation analysis of fcc Fe–Cr–Ni ternary alloy at 288°C: A quantum chemical molecular dynamics approach*. Corrosion Science, 2009. **51**(4): p. 908-913.
103. Jarvis, E.A.A., R.L. Hayes, and E.A. Carter, *Effects of Oxidation on the Nanoscale Mechanisms of Crack Formation in Aluminum*. ChemPhysChem, 2001. **2**(1): p. 55-59.
104. Andresen, P.L. and F.P. Ford, *Life prediction by mechanistic modeling and system monitoring of environmental cracking of iron and nickel alloys in aqueous systems*. Materials Science & Engineering A: Structural Materials: Properties, Microstructure and Processing, 1988. **A103**(1): p. 167-184.
105. Shoji, T., et al. *Modeling stress corrosion cracking growth rates based upon the effect of stress/strain on crack tip interface degradation and oxidation reaction kinetics*. 2009. New York, NY, USA: ASME.
106. Hall, M.M., Jr., *An alternative to the Shoji crack tip strain rate equation*. Corrosion Science, 2008. **50**(10): p. 2902-5.
107. Lim, Y.S., H.P. Kim, and S.S. Hwang, *Microstructural characterization on intergranular stress corrosion cracking of Alloy 600 in PWR primary water environment*. Journal of Nuclear Materials, 2013. **440**(1-3): p. 46-54.
108. Stiller, K., *Investigations of grain boundary microchemistry in nickel base superalloys*. Surface Science, 1991. **246**: p. 225-30.
109. Taylor, C., R.G. Kelly, and M. Neurock, *First-Principles Calculations of the Electrochemical Reactions of Water at an Immersed Ni (111) /H<sub>2</sub>O Interface*. Journal of the Electrochemical Society, 2006. **153**(12): p. E207-E214.
110. Yi, S., P. Qing, and L. Gang, *Quantum mechanical modeling of hydrogen assisted cracking in aluminum*. Physical Review B (Condensed Matter and Materials Physics), 2013. **88**(10): p. 104109 (6 pp.).
111. Song, J. and W.A. Curtin, *A nanoscale mechanism of hydrogen embrittlement in metals*. Acta Materialia, 2011. **59**(4): p. 1557-1569.
112. Song, J. and W.A. Curtin, *Atomic mechanism and prediction of hydrogen embrittlement in iron*. Nat Mater, 2013. **12**(2): p. 145-151.
113. Oriani, R.A., *Whitney Award Lecture—1987: Hydrogen—The Versatile Embrittler*. Corrosion, 1987. **43**(7): p. 390-397.
114. Lynch, S.P., *Environmentally assisted cracking: Overview of evidence for an adsorption-induced localised-slip process*. Acta Metallurgica, 1988. **36**(10): p. 2639-2661.
115. Birnbaum, H.K. and P. Sofronis, *Hydrogen-enhanced localized plasticity—a mechanism for hydrogen-related fracture*. Materials Science and Engineering: A, 1994. **176**(1–2): p. 191-202.
116. Zeng, C.A., J.P. Hu, and C.Y. Ouyang, *Hydrogen solution in tetrahedral or octahedral interstitial sites in Al*. Journal of Alloys and Compounds, 2011. **509**(37): p. 9214-9217.
117. Gunaydin, H., et al., *First-principles theory of hydrogen diffusion in aluminum*. Physical Review Letters, 2008. **101**(7).
118. Wolverton, C., V. Ozolins, and M. Asta, *Hydrogen in aluminum: first-principles calculations of structure and thermodynamics*. Physical Review B (Condensed Matter and Materials Physics), 2004. **69**(14): p. 144109-1.
119. Scully, J.R., G.A. Young Jr, and S.W. Smith, *Hydrogen solubility, diffusion and trapping in high purity aluminum and selected Al-base alloys*. Materials Science Forum, 2000. **331**: p. 1583-1600.
120. Lu, G. and E. Kaxiras, *Hydrogen Embrittlement of Aluminum: The Crucial Role of Vacancies*. Physical Review Letters, 2005. **94**(15): p. 155501.
121. Taylor, K.L. and A.H. Sherry, *The characterization and interpretation of ductile fracture mechanisms in AL2024-T351 using X-ray and focused ion beam tomography*. Acta Materialia, 2012. **60**(3): p. 1300-1310.

122. Jagodzinski, Y.N., L.N. Larikov, and A.Y. Smouk. *Void formation in hydrogen charged metals induced by plastic deformation as the initial stage of embrittlement*. in *Proceedings of the 1994 5th International Conference on the Effect of Hydrogen on the Behavior of Materials, September 11, 1994 - September 14, 1994*. 1996. Moran, WY, USA: Minerals, Metals & Materials Soc (TMS).
123. de Leeuw, N.H. and S.C. Parker, *Effect of chemisorption and physisorption of water on the surface structure and stability of -alumina*. *Journal of the American Ceramic Society*, 1999. **82**(11): p. 3209-16.
124. Hass, K.C., et al., *Chemistry of water on alumina surfaces: reaction dynamics from first principles*. *Science*, 1998. **282**(5387): p. 265-268.
125. Hupa, L., et al., *Chemical durability of glazed surfaces*. *Journal of the European Ceramic Society*, 2007. **27**(2-3): p. 1811-16.
126. Barinov, S.M., et al., *Dynamic fatigue of ceramics based on aluminum oxide*. *Refractories and Industrial Ceramics*, 1996. **37**(11): p. 375-377.
127. Okabe, T., M. Kido, and T. Miyahara, *Fatigue fracture behavior of oxide ceramics in water*. *Engineering Fracture Mechanics*, 1994. **48**(1): p. 137-146.
128. Shi, B., et al., *Stress Corrosion Cracking and Hydrogen-Induced Cracking of an Alumina Ceramic*. *Journal of the American Ceramic Society*, 2005. **88**(2): p. 353-356.
129. Chen, C.P. and W.J. Knapp. *Fatigue fracture of an alumina ceramic at several temperatures*. 1974. New York, NY, USA: Plenum.
130. Attaoui, H.E., et al., *Quantitative Analysis of Crack Shielding Degradation During Cyclic Fatigue of Alumina*. *Journal of the American Ceramic Society*, 2005. **88**(1): p. 172-178.
131. Gilbert, C.J., et al., *Cyclic fatigue in monolithic alumina: mechanisms for crack advance promoted by frictional wear of grain bridges*. *Journal of Materials Science*, 1995. **30**(3): p. 643-654.
132. Hu, X. and Y.W. Mai, *Crack-bridging analysis for alumina ceramics under monotonic and cyclic loading*. *Journal of the American Ceramic Society*, 1992. **75**(4): p. 848-53.
133. Kovarik, O., et al., *Young's modulus and fatigue behavior of plasma-sprayed alumina coatings*. *Journal of Thermal Spray Technology*, 2005. **14**(2): p. 231-8.
134. Jarvis, E.A.A. and E.A. Carter, *A Nanoscale Mechanism of Fatigue in Ionic Solids*. *Nano Letters*, 2006. **6**(3): p. 505-509.
135. Li, M. and F. Guiu, *Subcritical fatigue crack growth in alumina—II. Crack bridging and cyclic fatigue mechanisms*. *Acta Metallurgica et Materialia*, 1995. **43**(5): p. 1871-1884.
136. Hanlian, L., T. Xinying, and H. Chuanzhen, *Effect of Al<sub>2</sub>O<sub>3</sub> particle size on the mechanical properties of alumina-based ceramics*. *Materials Science & Engineering A (Structural Materials: Properties, Microstructure and Processing)*, 2007. **452-453**: p. 545-51.
137. Koike, J., et al. *Effects of grain boundary amorphous phase on high-temperature ductility in alumina polycrystals*. in *11th International Conference on the Strength of Materials, 25-29 Aug. 1997*. 1997. Switzerland: Elsevier.
138. Tomaszewski, H., M. Boniecki, and H. Weglarz, *Effect of grain size on R-curve behaviour of alumina ceramics*. *Journal of the European Ceramic Society*, 2000. **20**(14-15): p. 2569-2574.
139. Ma, Q. and D.R. Clarke, *Piezospectroscopic determination of residual stresses in polycrystalline alumina*. *Journal of the American Ceramic Society*, 1994. **77**(2): p. 298-302.
140. Sherman, D. and I. Be'ery, *Fracture mechanisms of sapphire under bending*. *Journal of Materials Science*, 2000. **35**(5): p. 1283-1293.
141. Swanson, P.L., et al., *Crack-interface grain bridging as a fracture resistance mechanism in ceramics. I. Experimental study on alumina*. *Journal of the American Ceramic Society*, 1987. **70**(4): p. 279-89.

142. Sklarczyk, C., *The acoustic emission analysis of the crack processes in alumina*. Journal of the European Ceramic Society, 1992. **9**(6): p. 427-35.
143. Ma, E., *Amorphization in mechanically driven material systems*. Scripta Materialia, 2003. **49**(10 SPEC.): p. 941-946.
144. Swamy, V., et al., *Size-dependent pressure-induced amorphization in nanoscale TiO<sub>2</sub>*. Physical Review Letters, 2006. **96**(13): p. 135702-1.
145. Wang, L., et al., *Size-dependent amorphization of nanoscale Y<sub>2</sub>O<sub>3</sub> at high pressure*. Physical Review Letters, 2010. **105**(9).
146. Kawai, N., et al., *Dynamic deformation and fracture of mullite (3Al<sub>2</sub>O<sub>3</sub>.2SiO<sub>2</sub>) ceramics under hypervelocity impact*. International Journal of Impact Engineering, 2008. **35**(12): p. 1612-15.
147. Wang, J., et al., *Unifying two criteria of Born: Elastic instability and melting of homogeneous crystals*. Physica A: Statistical Mechanics and its Applications, 1997. **240**(1-2): p. 396-403.
148. Ovid'ko, I.A., *Nanoscale amorphization as a special deformation mode in nanowires*. Scripta Materialia, 2012. **66**(6): p. 402-5.
149. Barbour, J.C., et al. *The mechanical properties of alumina films formed by plasma deposition and by ion irradiation of sapphire*. in *10th International Conference on Radiation Effects in Insulators, 18-23 July 1999*. 2000. Netherlands: Elsevier.
150. Gandhi, A.S. and V. Jayaram, *Plastically deforming amorphous ZrO<sub>2</sub>-Al<sub>2</sub>O<sub>3</sub>*. Acta Materialia, 2003. **51**(6): p. 1641-1649.
151. Kumar, S., et al., *Can Amorphization take Place in Nanoscale Interconnects?* Nanotechnology, 2012. **23**(9): p. 095701 (8 pp.).
152. Mitchell, T.E., K.P.D. Lagerlof, and A.H. Heuer, *DISLOCATIONS IN CERAMICS*. Materials Science and Technology, 1985. **1**(11): p. 944-949.
153. Yoshida, H., Y. Ikuhara, and T. Sakuma, *High temperature plastic deformation related to grain boundary chemistry in cation-doped alumina*. Materials Science and Engineering A, 2004. **387-389**(1-2 SPEC. ISS.): p. 723-727.
154. Bataille, A., et al., *Deformation behaviour of iron-doped alumina*. Journal of the European Ceramic Society, 2005. **25**(6): p. 857-862.
155. Schultz, R.A., M.C. Jensen, and R.C. Bradt, *Single crystal cleavage of brittle materials*. International Journal of Fracture, 1994. **65**(4): p. 291-312.
156. Boettger, J.C., *High-precision, all-electron, full-potential calculation of the equation of state and elastic constants of corundum*. Physical Review B: Condensed Matter, 1997. **55**(2): p. 750-750.
157. Mitamura, Y. and Y. Wang, *Fracture toughness of single crystal alumina in air and a simulated body environment*. Journal of Biomedical Materials Research, 1994. **28**(7): p. 813-817.
158. Pham, H.H., et al., *Finite-temperature elasticity of fcc Al: Atomistic simulations and ultrasonic measurements*. Physical Review B (Condensed Matter and Materials Physics), 2011. **84**(6): p. 064101 (10 pp.).
159. Vallin, J., et al., *Elastic constants of aluminum*. Journal of Applied Physics, 1964. **35**(6): p. 1825-1826.
160. Hung, L. and E.A. Carter, *Ductile processes at aluminium crack tips: Comparison of orbital-free density functional theory with classical potential predictions*. Modelling and Simulation in Materials Science and Engineering, 2011. **19**(4).
161. Simmons, G. and H. Wang, *Single crystal elastic constants and calculated aggregate properties. A handbook*. 1971, London, UK: MIT Press. ixx+370.
162. Terentyev, D., E.E. Zhurkin, and G. Bonny, *Emission of full and partial dislocations from a crack in BCC and FCC metals: An atomistic study*. Computational Materials Science, 2012. **55**: p. 313-321.

163. Schiotz, J. and A.E. Carlsson, *The influence of surface stress on dislocation emission from sharp and blunt cracks in fcc metals*. Philosophical Magazine A (Physics of Condensed Matter: Structure, Defects and Mechanical Properties), 2000. **80**(1): p. 69-82.
164. Siegel, D.J., L.G. Hector, and J.B. Adams, *Adhesion, atomic structure, and bonding at the Al(111)/-Al<sub>2</sub>O<sub>3</sub>(0001) interface: A first principles study*. Physical Review B (Condensed Matter and Materials Physics), 2002. **65**(8): p. 085415-1.
165. Tagarielli, V.L. and N.A. Fleck, *The Shear Response of a Thin Aluminum Layer*. Journal of Applied Mechanics, 2011. **78**(1): p. 014505 (3 pp.).
166. Goldsby, J.C., *High temperature mechanical behavior of polycrystalline alumina from mixed nanometer and micrometer powders*. Ceramics International, 2001. **27**(6): p. 701-3.
167. Sen, D., A.P. Garcia, and M.J. Buehler, *Mechanics of Nano-Honeycomb Silica Structures: Size-Dependent Brittle-to-Ductile Transition*. Journal of Nanomechanics and Micromechanics, 2011. **1**(4): p. 112-118.
168. Qiang, L., et al., *Nanoscale fracture of tetrahedral amorphous carbon by molecular dynamics: flaw size insensitivity*. Physical Review B (Condensed Matter and Materials Physics), 2008. **77**(1): p. 014109-1.
169. Ding, J.N., Y.G. Meng, and S.Z. Wen, *Specimen size effect on mechanical properties of polysilicon microcantilever beams measured by deflection using a nanoindenter*. Materials Science & Engineering B (Solid-State Materials for Advanced Technology), 2001. **B83**(1-3): p. 42-7.
170. Tuckerman, M.E., et al., *Modified nonequilibrium molecular dynamics for fluid flows with energy conservation*. The Journal of Chemical Physics, 1997. **106**(13): p. 5615-5621.
171. Theofanis, P.L., et al., *Nonadiabatic Study of Dynamic Electronic Effects during Brittle Fracture of Silicon*. Physical Review Letters, 2012. **108**(4): p. 045501 (5 pp.).
172. Kraehling, D., et al. *Effect of strain rate and triaxiality on the stress-strain response of super vacuum die cast AM60B magnesium alloy*. in *Materials Science and Technology Conference and Exhibition 2013, MS and T 2013, October 27, 2013 - October 31, 2013*. 2013. Montreal, QC, Canada: Association for Iron and Steel Technology, AISTECH.
173. Koenig, J.A., *Shakedown of elastic-plastic structures*. Fundamental studies in engineering. Vol. 7. 1987: Elsevier.
174. Sen, F.G., et al., *Oxidation-assisted ductility of aluminium nanowires*. Nat Commun, 2014. **5**.
175. Rozhanskii, V.N., et al., *Dislocation and crowdion plasticity of corundum at room temperature*. Physica Status Solidi, 1970. **41**(2): p. 579-90.
176. Huang, L., et al., *Investigation into the microstructure evolution caused by nanoscratch-induced room temperature deformation in M-plane sapphire*. Acta Materialia, 2011. **59**(13): p. 5181-5193.
177. Liu, H., et al., *Structural refinement of the high-pressure phase of aluminum trihydroxide: In-situ high-pressure angle dispersive synchrotron X-ray diffraction and theoretical studies*. Journal of Physical Chemistry B, 2005. **109**(18): p. 8857-8860.
178. Goto, T., et al., *Elastic constants of corundum up to 1825 K*. Journal of Geophysical Research, 1989. **94**(B6): p. 7588-602.
179. Thaulow, C., D. Sen, and M.J. Buehler, *Atomistic study of the effect of crack tip ledges on the nucleation of dislocations in silicon single crystals at elevated temperature*. Materials Science & Engineering: A (Structural Materials: Properties, Microstructure and Processing), 2011. **528**(13-14): p. 4357-64.
180. Baker, K.L. and D.H. Warner, *An atomistic investigation into the nature of near threshold fatigue crack growth in aluminum alloys*. Preprint submitted to Engineering Fracture Mechanics, 2013.
181. Voter, A.F., *Parallel replica method for dynamics of infrequent events*. Physical Review B (Condensed Matter), 1998. **57**(22): p. 13985-8.

182. Le Bris, C., et al., *A mathematical formalization of the parallel replica dynamics*, in *Monte Carlo Methods and Applications*. 2012. p. 119.
183. Joshi, K.L., S. Raman, and A.C.T. van Duin, *Connectivity-Based Parallel Replica Dynamics for Chemically Reactive Systems: From Femtoseconds to Microseconds*. *The Journal of Physical Chemistry Letters*, 2013. **4**(21): p. 3792-3797.
184. Cozmuta, I. *Molecular mechanisms of gas surface interactions in hypersonic flow*. in *39th AIAA Thermophysics Conference, June 25, 2007 - June 28, 2007*. 2007. Miami, FL, United states: American Institute of Aeronautics and Astronautics Inc.
185. Valentini, P., T.E. Schwartzentruber, and I. Cozmuta, *ReaxFF Grand Canonical Monte Carlo simulation of adsorption and dissociation of oxygen on platinum (111)*. *Surface Science*, 2011. **605**(23-24): p. 1941-50.
186. Senftle, T.P., et al., *Development of a ReaxFF potential for Pd/O and application to palladium oxide formation*. *Journal of Chemical Physics*, 2013. **139**(4): p. 044109 (15 pp.).
187. Lachet, V., et al., *Grand canonical Monte Carlo simulations of adsorption of mixtures of xylene molecules in faujasite zeolites*. *Faraday Discussions*, 1997. **106**(0): p. 307-323.
188. *NIST-JANAF Thermochemical Tables*. 2000 [cited 2013 11/1]; Available from: <http://kinetics.nist.gov/janaf/>.
189. Bao, Y. and T. Wierzbicki, *On fracture locus in the equivalent strain and stress triaxiality space*. *International Journal of Mechanical Sciences*, 2004. **46**(1): p. 81-98.
190. Hull, D. and D.J. Bacon, *Introduction to Dislocations*. 5 ed. 2011: Butterworth-Heinemann.
191. Kitamura, T., K. Yashiro, and R. Ohtani, *Atomic simulation on deformation and fracture of nano-single crystal of nickel in tension*. *JSME International Journal, Series A (Solid Mechanics and Material Engineering)*, 1997. **40**(4): p. 430-5.
192. Beverskog, B. and I. Puigdomenech, *Revised Pourbaix diagrams for nickel at 25-300C*. *Corrosion Science*, 1997. **39**(5): p. 969-80.
193. Phatak, A.A., et al., *Density functional theory comparison of water dissociation steps on Cu, Au, Ni, Pd, and Pt*. *Journal of Physical Chemistry C*, 2009. **113**(17): p. 7269-7276.
194. Hong, Y. and J.L. Whitten, *The adsorption of water and hydroxyl on Ni(111)*. *Surface Science*, 1989. **223**(1-2): p. 131-50.
195. Sun, Y., Q. Peng, and G. Lu, *Quantum mechanical modeling of hydrogen assisted cracking in aluminum*. *Physical Review B*, 2013. **88**(10): p. 104109.
196. Miller, R., et al., *Quasicontinuum simulation of fracture at the atomic scale*. *Modelling and Simulation in Materials Science and Engineering*, 1998. **6**(5): p. 607-38.
197. Winning, M., et al., *Mobility of low-angle grain boundaries in pure metals*. *Philosophical Magazine*, 2010. **90**(22): p. 3107-3128.
198. Horstemeyer, M.F., M.I. Baskes, and S.J. Plimpton, *Length scale and time scale effects on the plastic flow of fcc metals*. *Acta Materialia*, 2001. **49**(20): p. 4363-4374.
199. Potirniche, G.P., et al., *A molecular dynamics study of void growth and coalescence in single crystal nickel*. *International Journal of Plasticity*, 2006. **22**(2): p. 257-278.
200. Mehrer, H., *Diffusion in Solids - Fundamentals, Methods, Materials, Diffusion-Controlled Processes*. Springer Series in Solid-State Sciences. Vol. 155. 2007: Springer.

## Appendix A

### Annealing and oxidation of binary $\text{Mo}_3\text{Ni}$ -cluster

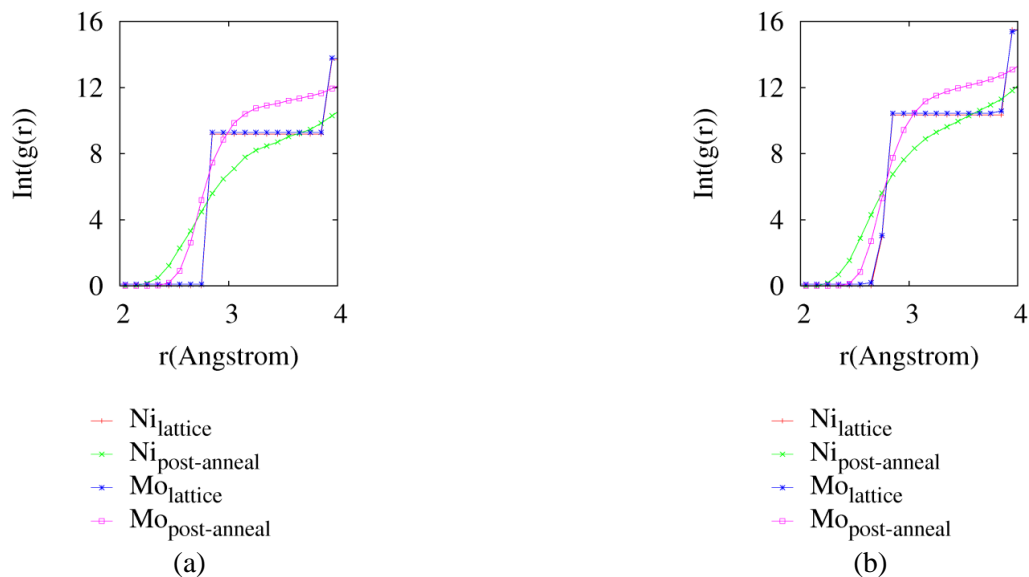


Figure A-1. IRDF for Mo and Ni atoms in the initial (lattice) and annealed states (a – 256-atom cluster, b – 1372-atom cluster).

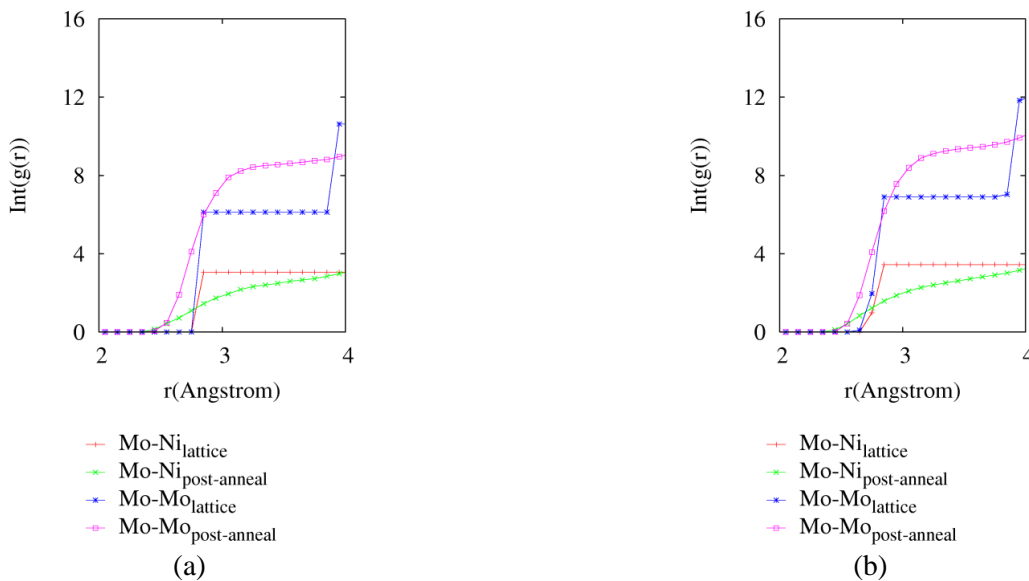


Figure A-2. IRDF for Mo atoms with respect to Mo and Ni atoms separately in the initial (lattice) and annealed states (a – 256-atom cluster, b – 1372-atom cluster).

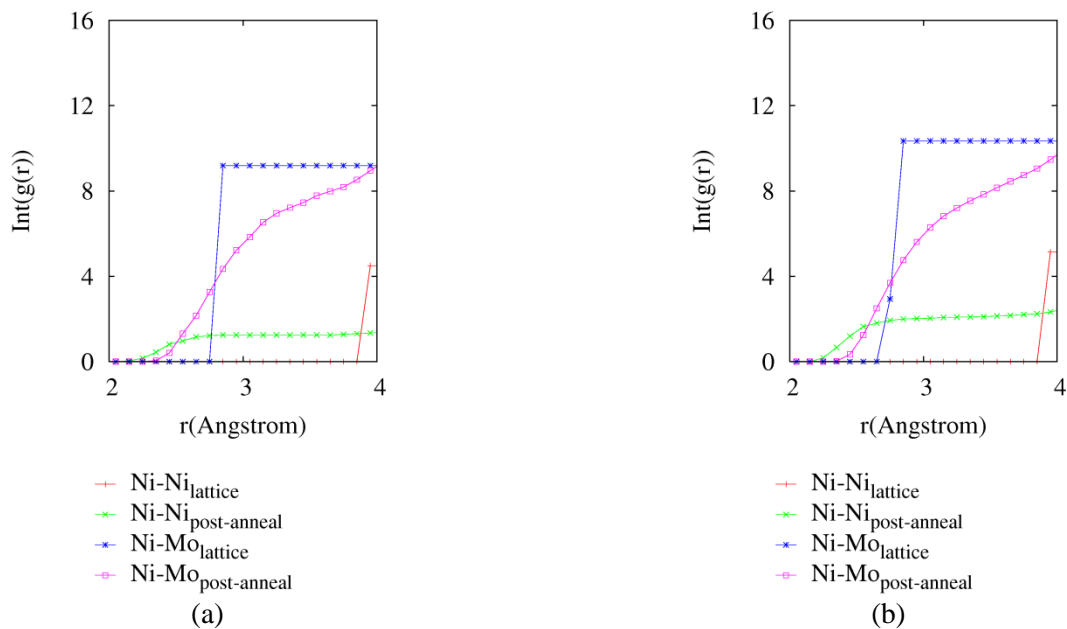


Figure A-3. IRDF for Ni atoms with respect to Mo and Ni atoms separately in the initial (lattice) and annealed states (a – 256-atom cluster, b – 1372-atom cluster).

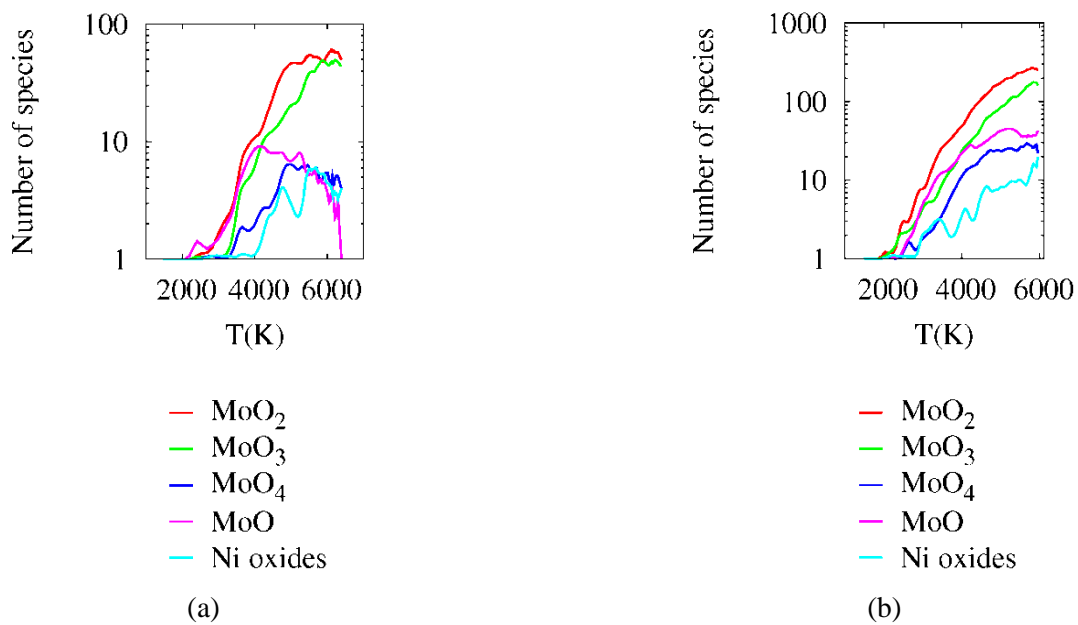


Figure A-4. Bezier interpolated numbers of  $\text{MoO}_x$  and  $\text{NiO}_x$  species vs. temperature during the cluster oxidation (a – 256-atom cluster, b – 1372-atom cluster).

## Appendix B

### Molecular dynamics simulation of Al grain mixing in Fe/Ni matrices and its influence on oxidation

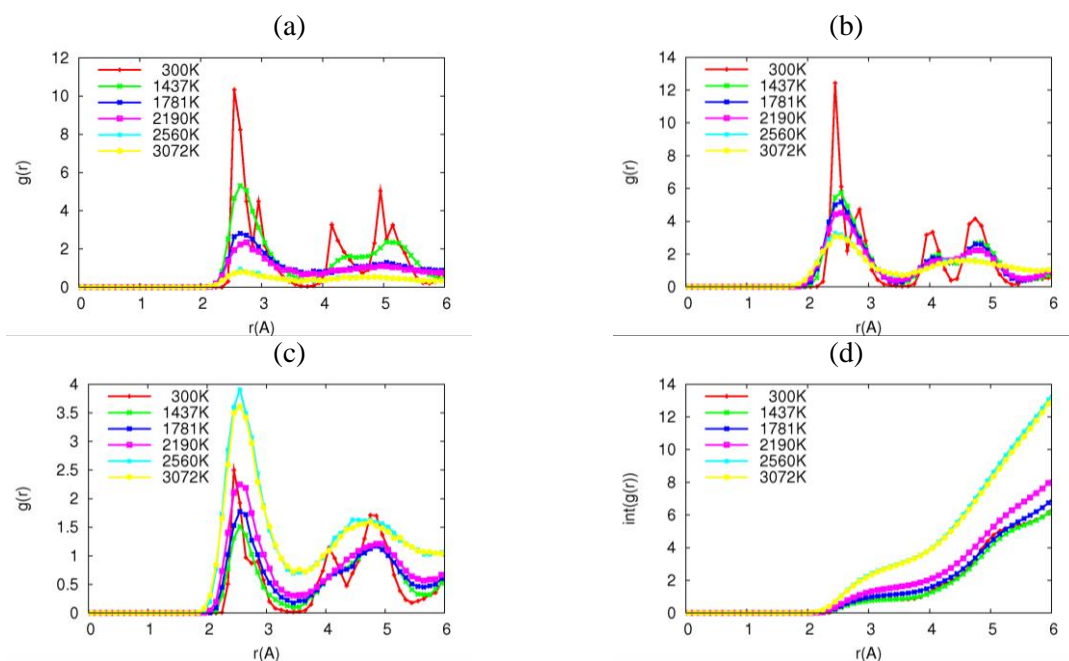


Figure B-1. RDF of Al-Al (a), Fe-Fe (b), Fe-Al (c) and IRDF of Fe-Al (d) for 1 Al grain in Fe matrix structure during heating.

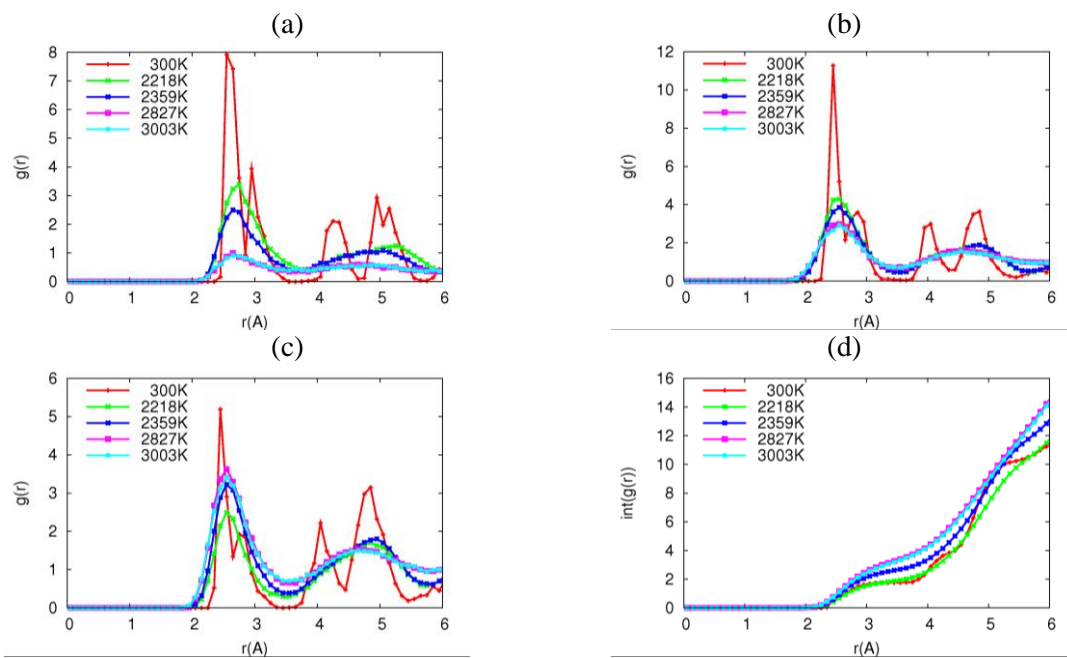


Figure B-2. RDF of Al-Al (a), Fe-Fe (b), Fe-Al (c) and IRDF of Fe-Al (d) for 8 Al grains in Fe matrix structure during heating.

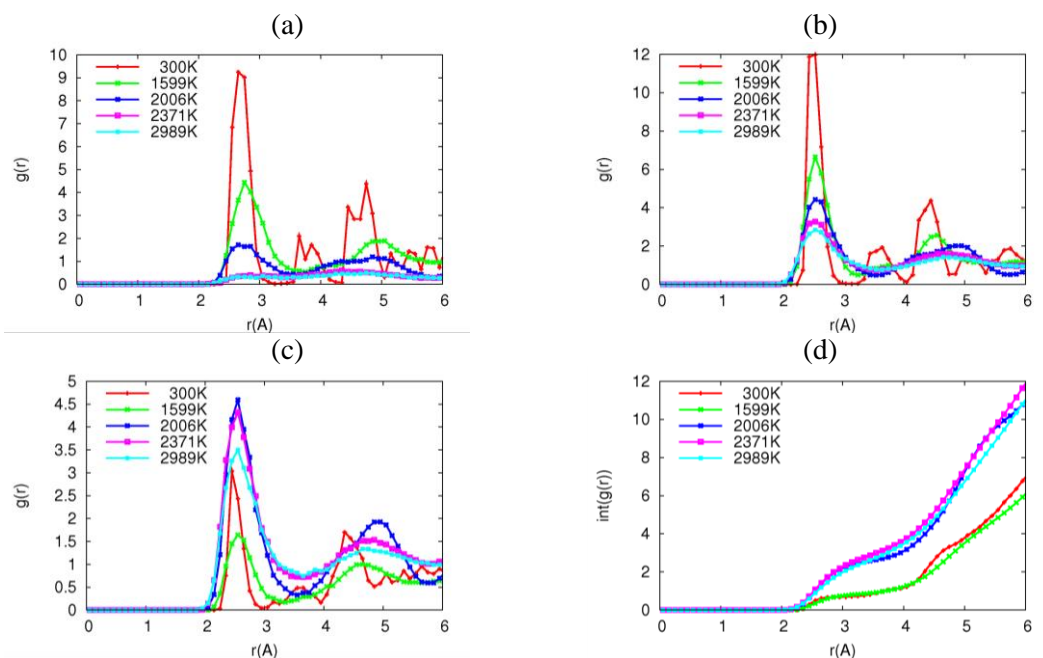


Figure B-3. RDF of Al-Al (a), Ni-Ni (b), Ni-Al (c) and IRDF of Ni-Al (d) for 1 Al grain in Ni matrix structure during heating.

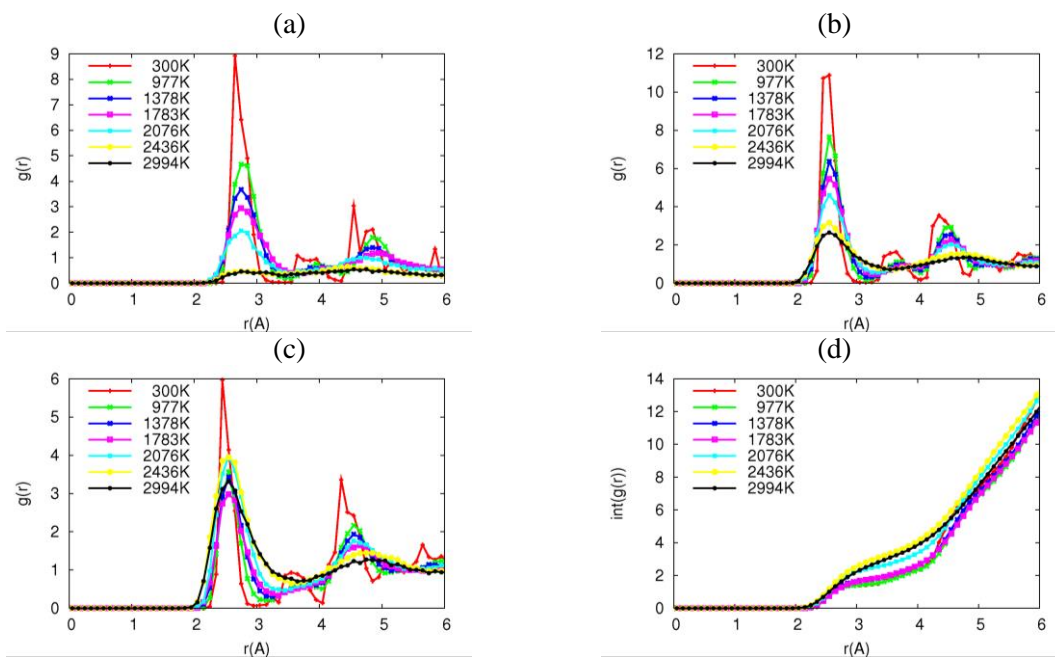


Figure B-4. RDF of Al-Al (a), Ni-Ni (b), Ni-Al (c) and IRDF of Ni-Al (d) for 8 Al grains in Ni matrix structure during heating.

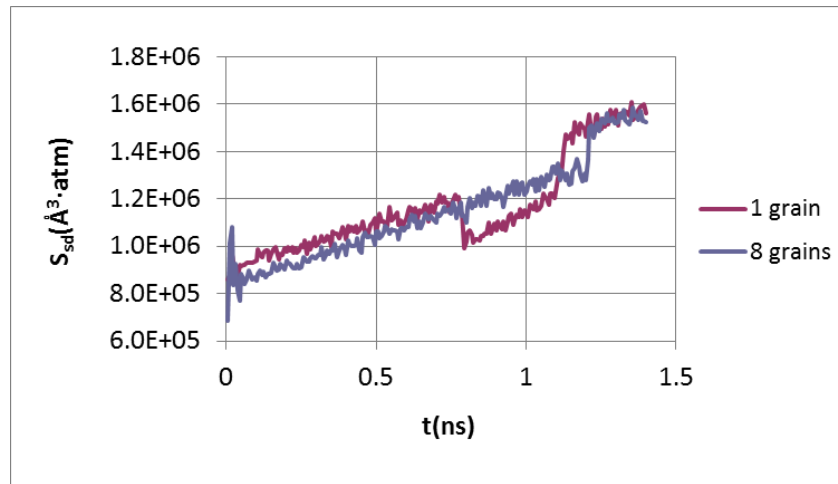


Figure B-5. Standard deviation of atomic hydrostatic stress vs. time for 1/8 Al grain Fe matrix structures during heating.

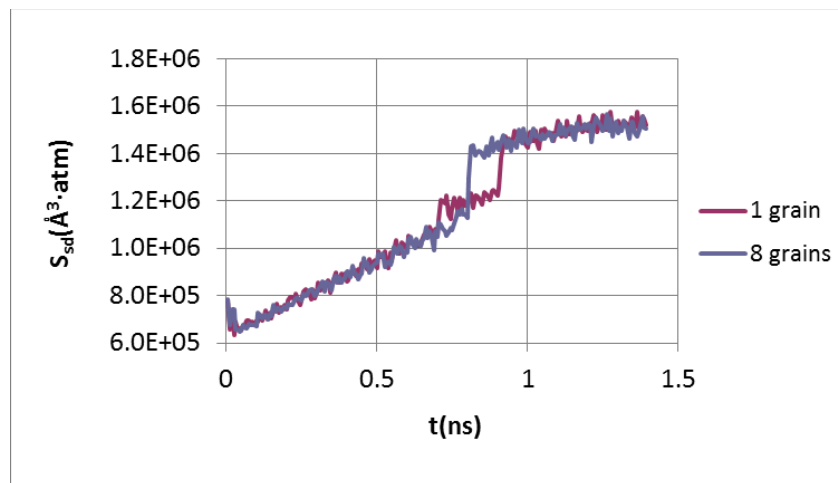


Figure B-6. Standard deviation of atomic hydrostatic stress vs. time for 1/8 Al grain Ni matrix structures during heating.

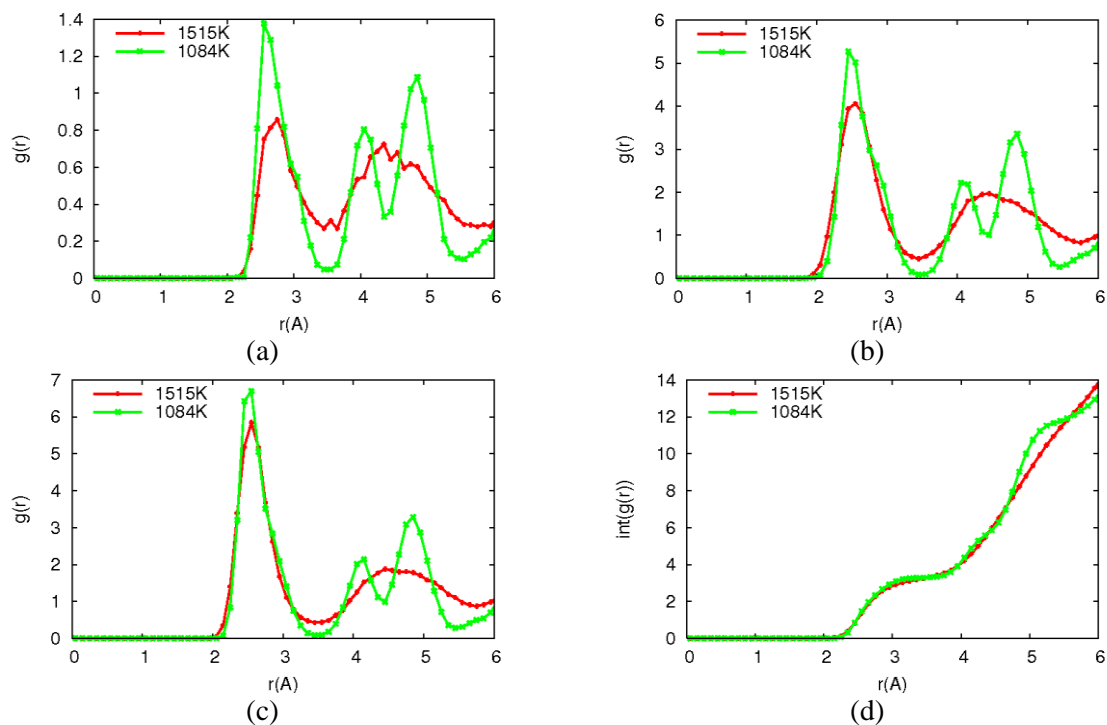


Figure B-7. RDF of Al-Al (a), Fe-Fe (b), Fe-Al (c) and IRDF of Fe-Al (d) for molten 1 Al grain in Fe matrix structure during cooling.

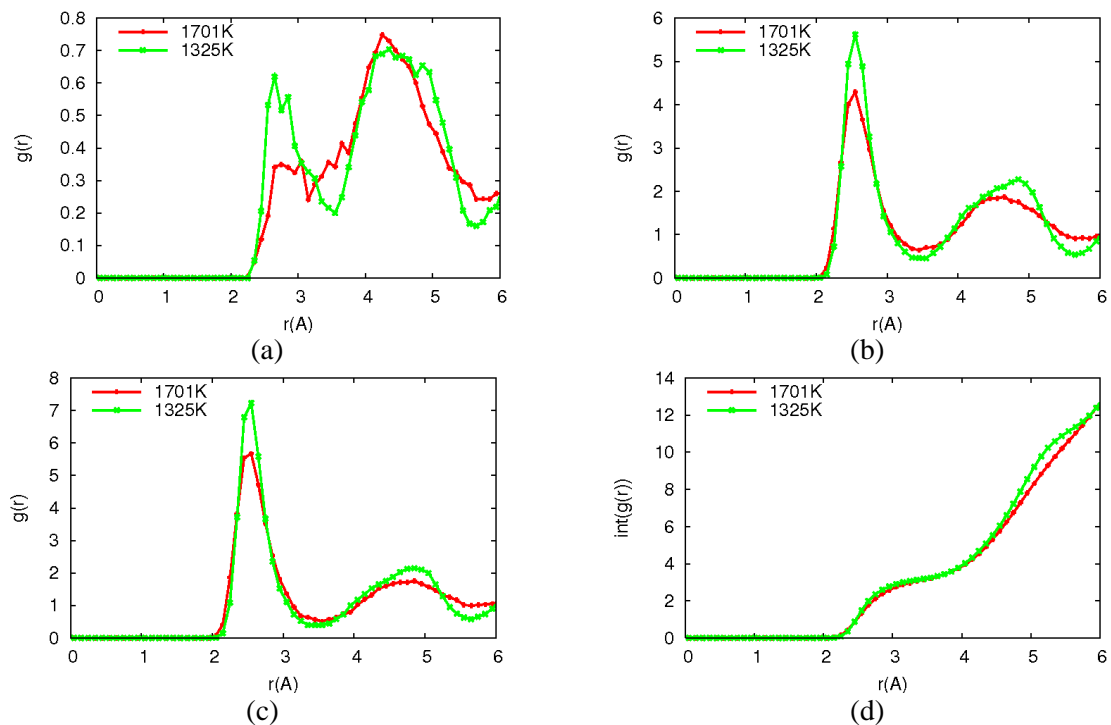


Figure B-8. RDF of Al-Al (a), Ni-Ni (b), Ni-Al (c) and IRDF of Ni-Al (d) for molten 1 Al grain in Ni matrix structure during cooling.

## Appendix C

### Dissertation related papers and conference presentations

#### Papers:

1. Verners, O., van Duin, A. C. T., *Molecular dynamics study of  $\alpha$ -Al<sub>2</sub>O<sub>3</sub> fatigue behavior*, manuscript in preparation.
2. Verners, O., van Duin, A. C. T., *Comparative molecular dynamics study of fcc-Al hydrogen embrittlement*, manuscript in preparation.
3. Verners, O., van Duin, A. C. T., *Comparative molecular dynamics study of fcc-Ni nanoplate stress corrosion in water*, manuscript in preparation.
4. van Duin, A. C. T., Verners, O., Shin, Y. K., *Reactive force fields: concepts of reaxff and applications to high-energy materials*, International Journal of Energetic Materials and Chemical Propulsion **12**, 95 (2013).
5. Liang, T., Shin, Y. K., Cheng, Y. T., Yilmaz, D. E., Vishnu, K. G., Verners, O., Zou, C., Phillpot, S. R., Sinnott, S. B., van Duin, A. C. T., *Reactive potentials for advanced atomistic simulations*, Annu. Rev. Mater. Res. **43**, 109 (2013).
6. Verners, O., Shin, Y. K., and van Duin, A. C. T., *Molecular dynamics simulation of Al grain mixing in Fe/Ni matrices and its influence on oxidation*, J. Appl. Phys. **114**, 023501 (2013).
7. Assowe, O., Politano, O., Vignal, V., Arnoux, P., Diawara, B., Verners, O., and van Duin, A. C. T., *Reactive molecular dynamics simulation of the initial oxidation stages of Ni (111) in pure water: Effect of an applied electric field*, Journal of Physical Chemistry A **116**, 11796 (2012).
8. Vasenkov, A., Newsome, D., Verners, O., Russo, M. F., Zaharieva, R., van Duin, A. C. T., *Reactive molecular dynamics study of Mo-based alloys under high-pressure, high-temperature conditions*, J. Appl. Phys. **112**, 013511 (2012).

#### Conference presentations:

1. Lordi, V., Ong, M., Verners, O., van Duin, A. C. T., Draeger, E., Pask, J., *Electrolyte Structure near Electrode Interfaces in Lithium-Ion Batteries*. APS March Meeting 2014, March 3–7, 2014, Denver, Colorado.
2. Verners, O., van Duin, A. C. T., *Molecular dynamics simulation of Al oxide stress corrosion cracking*. MS&T 2013 Conference, October 27-31, 2013, Montreal, Quebec, Canada.
3. Verners, O., van Duin, A. C. T., Shin, Y. K. *MD simulation of Al grain mixing/diffusion in Fe/Ni matrices*. ACS Fall 2012 Meeting, August 19-23, 2012, Philadelphia, Pennsylvania.

## VITA

### Osvalds Verners

#### Professional/Research experience

01/2011-06/2014	graduate research assistant with Dr. Adri van Duin, Department of Mechanical and Nuclear Engineering, The Pennsylvania State University;
06/2013-08/2013	Computational Chemistry and Materials Science Summer Institute intern at Lawrence Livermore National Laboratory (Li ion battery simulations);
08/2010-12/2010	teaching assistant at the Department of Mechanical and Nuclear Engineering, Pennsylvania State University;
02/2009-07/2010	researcher at the Research Centre for Civil Engineering at Riga Technical University;
07/2005-06/2006	designing engineer at company Peruza Ltd., specialized in production of automated food production equipment;
02/2005-05/2005	trainee at the engineering office of company Peruza Ltd., specialized in production of automated food production equipment;

#### Professional studies

08/2010-present	<i>Mechanical Engineering</i> doctorate study program at The Pennsylvania State University;
10/2006-09/2008	<i>Computer Aided Conception in Mechanical Engineering</i> Master of Engineering study program at Aachen University of Technology;
09/2003-01/2006	<i>Mechanics and Mechanical Engineering</i> engineer's degree (equivalent to bachelor's degree) study program, major <i>Production Automation and Processing Technology</i> , at Riga Technical University;
09/2001-06/2003	<i>Industrial Design / Computer Graphics</i> college (professional) study program at Riga Technical University;